UNITED NATIONS EDUCATIONAL, SCIENTIFIC AND CULTURAL ORGANIZATION
INTERNATIONAL ATOMIC ENERGY AGENCY
INTERNATIONAL CENTRE FOR THEORETICAL PHYSICS
I.C.T.P., P.O. BOX 586, 34100 TRIESTE, ITALY, CABLE: CENTRATOM TRIESTE

H4.SMR/1013-2

SCHOOL ON THE USE OF SYNCHROTRON RADIATION
IN SCIENCE AND TECHNOLOGY:
"John Fuggle Memorial"

3 November - 5 December 1997

Miramare - Trieste, Italy

Insertion Devices: Undulators and Wigglers

Richard P. Walker
Sincrotrone Trieste, Italy

ST/M-97/2

Insertion Devices: Undulators and Wigglers

Richard P. Walker

June 1997

---

* Invited lectures at the CERN Accelerator School on Synchrotron Radiation and Free-Electron Lasers Grenoble, April 1996

INSERTION DEVICES: UNDULATORS AND WIGGLERS

Richard P. Walker
Sincrotrone Trieste, Italy

Abstract
The main features of the design and performance of insertion devices are discussed, including the radiation characteristics, magnetic design aspects, and performance optimisation for both standard devices and those producing circularly polarized radiation. The special requirements of undulators used for free-electron lasers are also considered.

1. INTRODUCTION

Undulators and wigglers are magnetic devices producing a spatially periodic field variation that cause a charged particle beam, usually electrons or positrons, to emit electromagnetic radiation with special properties. They are also commonly called "insertion devices", particularly in the context of storage rings, since they can be installed and operated more or less independently of the operation of the ring itself. A large number of insertion devices are in operation in synchrotron radiation facilities world-wide providing radiation with enhanced features compared to that from the bending magnets: higher photon energies, higher flux and brightness, and different polarization characteristics. Periodic magnets of this type are also at the heart of devices which generate coherent radiation, called free-electron lasers (FELs).

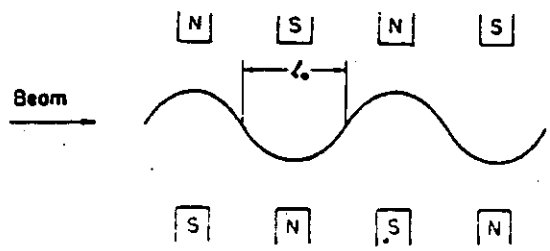

Schematic arrangement of undulator magnets.

Fig. 1 Origins of the undulator: from the first page of Motz's article [2]

Although insertion devices have only been regularly employed as sources of synchrotron radiation in storage rings for less than two decades, their history goes back much further. The first discussion of the use of artificial periodic structures for the generation of microwaves using energetic charged particles was made 50 years ago [1]. A little later, Motz independently proposed that a periodic magnetic structure, which he termed an "undulator" (Fig. 1), could be used to generate quasi-monochromatic electromagnetic radiation from microwaves up to hard X-rays using electron beams with energies in the 1 MeV to 1 GeV range [2]. The initial interest in these ideas was as a source of intense coherent microwave radiation using a tightly bunched electron beam, and experiments were later carried out [3] in which radiation with a wavelength around 1.9 mm was produced using a 3-5 MeV beam; visible light was also observed when using a 100 MeV beam. Similar experiments were also carried out in the Soviet Union [4]. Little further progress was made at that time however because of the difficulties of producing electron beams with the required characteristics to produce coherent radiation as well as the lack of higher energy beams for producing shorter wavelength radiation. In related work to that of Motz, Phillips in 1957 devised a device called a ubitron which uses an undulator and a low energy electron beam to achieve amplification of microwave radiation [5]. The relativistic analogue of this proposed by Madey in 1971 [6] became known as a "free-electron laser" and was first demonstrated in 1976.

The possibilities for using undulators in high energy synchrotrons and storage rings as a source of intense, quasi-monochromatic VUV, XUV and X-ray radiation was discussed by several authors in the late 60's and early 70's [7-10]. The first experimental investigations of the properties of undulator radiation at higher energies were carried out in the Soviet Union, using various synchrotrons. The first studies in 1971 used an extracted 3.6 GeV beam from the Arus synchrotron at Erevan to generate X-rays [11]. Subsequently in 1977-79 undulators were installed in the Pakhra (Lebedev Institute, Moscow) [12] and Sirius (Tomsk Polytechnical Institute) [13] synchrotrons. At the same time a large amount of theoretical work was carried out. The first complete and accessible analysis of the spectral/angular distribution in both planar and helical devices was given in Ref. [14]. In the West, the first detailed study of the radiation properties of the helical undulator was made by Kincaid [15]. The first undulators to be installed in storage rings were at the VEPP-3 ring at INP, Novosibirsk in 1979 [16] (for FEL experiments) closely followed by SSRL, Stanford in 1980 [17] (for generation of synchrotron radiation).

The use of periodic magnets in a regime in which interference effects can be neglected is also of interest. In this case the resulting spectrum at high photon energies is smooth, similar to that of a bending magnet, however the radiation intensity can be much higher as a result of the increased number of emitting poles, and higher magnetic field which generates radiation with a higher critical energy. The development of these devices, generally called "wigglers", went on in parallel to that of undulators, see for example Refs. [18,19]. The idea was an extension of the concept in which a single high field pole generates a harder spectrum than the usual bending magnets. The first device of this kind, called a "wavelength shifter", was built for the Tantalus storage ring in 1971 [20]. The first "multipole wiggler" devices were electromagnetic. For example, a 1.8 T, 5-pole device was installed at SSRL in 1979 [21], followed by a similar device on ADONE [22]. Since then permanent magnet devices have been developed with many more poles, for example the 55-pole device installed at SSRL in 1983 [23]. Superconducting technology has also been applied in order to reach higher field strengths. For example, a 3.5 T device was installed on VEPP3 in 1979 [24], and a 5 T wiggler on the SRS in 1982 [25]. Superconducting wigglers are currently operating in several synchrotron radiation facilities: SRS (England), DCI and ESRF (France), UVSOR and Photon Factory (Japan) and NSLS Xray Ring (USA).

Another reason for installing insertion devices in electron rings is to deliberately change the electron beam properties such as damping times, energy spread, and emittance. A periodic device with a gradient field was first described by Robinson in 1958 [26] and later used to convert the C.E.A. from a synchrotron to a storage ring [27]. The use of standard wiggler magnets to change beam sizes and polarization times was discussed in Ref. [28]. The effect of insertion devices on beam properties was discussed in detail in another CERN Accelerator School Proceedings [29] and so will not be repeated here.

In this report we consider the main features of the design and performance of insertion devices, including the radiation characteristics, magnetic design aspects, and performance optimisation. Both standard devices and those producing circularly polarized radiation are treated and the special requirements of undulators used for free-electron lasers are also examined. For further details the reader can refer to the many Conference and Workshop Proceedings [18,30-35], text books [36-42], Proceedings of Schools [43-45] and review articles [46-56].

2. BASIC FEATURES OF THE RADIATION FROM STANDARD INSERTION DEVICES

2.1 Electron motion

In order to understand the properties of the radiation emitted in insertion devices we must begin by firstly calculating the electron motion. We consider a standard device (Fig. 2) as one with median plane symmetry which produces a sinusoidal vertical field component along the magnet axis: $B_y = B_o \sin(kz)$, where $k = 2\pi/\lambda_o$ and λ_o is the insertion device period length.

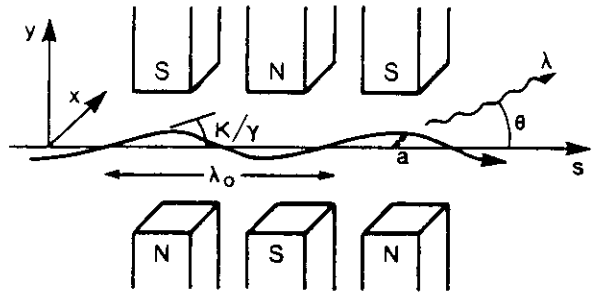

Fig. 2 Schematic of planar undulator and coordinate system

In this analysis we can ignore any transverse (x) variation in the field. The simplified equation of motion is then as follows:

$$\ddot{x} = \frac{e}{\gamma m}(-\dot{z} B_y) \qquad \ddot{z} = \frac{e}{\gamma m}(\dot{x} B_y) \tag{1}$$

The first equation can be integrated directly to give:

$$\dot{x} = \frac{eB_o}{\gamma m}\frac{\cos(kz)}{k}$$

and hence

$$\beta_x = \dot{x}/c = \frac{K}{\gamma}\cos(kz) \tag{2}$$

where the dimensionless undulator or deflection parameter is defined as follows:

$$\boxed{K = \frac{eB_o\lambda_o}{2\pi mc} = 93.4\ B_o[T]\ \lambda_o[m]}$$

The horizontal motion of the electron causes the electron velocity along the z axis to vary also, since the electron energy, and hence total speed remain unaltered:

$$\beta_x^2 + \beta_z^2 = \beta^2 \quad (= \text{constant})$$

Inserting Eq. (2) into the above we obtain:

$$\beta_z \equiv \beta\left(1 - \frac{K^2}{4\gamma^2} - \frac{K^2}{4\gamma^2}\cos 2kz\right)$$

The average velocity along the z-axis is thus:

$$\overline{\beta} \equiv \beta\left(1 - \frac{K^2}{4\gamma^2}\right) \equiv 1 - \frac{1}{2\gamma^2} - \frac{K^2}{4\gamma^2}$$

We will only consider cases in which $K/\gamma << 1$ and so we can write to a good approximation that $z = \overline{\beta} ct$ and $kz = \Omega t$ where $\Omega = 2\pi\overline{\beta}c/\lambda_o$. We have then:

$$\dot{x} = \frac{K}{\gamma} c\cos(\Omega t) \qquad \dot{z} = \overline{\beta}\, c - \frac{K^2}{4\gamma^2} c\cos(2\Omega t)$$

which can be integrated directly to give:

$$x = \frac{K}{\gamma}\frac{c}{\Omega}\sin(\Omega t) \qquad z = \bar{\beta}\,c\,t - \frac{K^2}{4\gamma^2}\frac{c}{2\Omega}\sin(2\Omega t)$$

In most cases the actual motion of the particle is quite small: for example, a realistic device with a 50 mm period and K = 2 in a 2 GeV ring has a maximum deflection angle (x') of 0.5 mrad and oscillation amplitude of 4 μm. The z-motion is even smaller with an amplitude of only 2.6 Å. Although the modulation in the z-motion is relatively small, it is significant in terms of the emitted wavelength (the fundamental has a wavelength of 49 Å in this example) and so has an important effect on the radiation characteristics, as will be seen later.

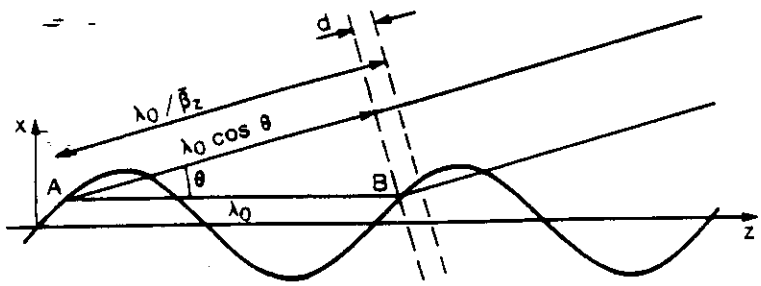

Fig. 3 Interference in an undulator

2.2 Interference

The radiation properties from an insertion device can most simply be understood in terms of an interference of wavefronts emitted *by the same electron* at different points in the magnet (see Fig. 3). In the time it takes the electron to move through one period length from point A to an equivalent point B ($\lambda_o/\bar{\beta}c$) the wavefront from A has advanced by a distance $\lambda_o/\bar{\beta}$ and hence is ahead of the radiation emitted at point B by a distance d where:

$$d = \frac{\lambda_o}{\bar{\beta}} - \lambda_o \cos\theta$$

and where θ is the angle of emission with respect to the electron beam axis. When this distance is equal to an integral number, n, of radiation wavelengths there is constructive interference of the radiation from successive poles:

$$\frac{\lambda_o}{\bar{\beta}} - \lambda_o \cos\theta = n\lambda \tag{3}$$

Inserting the expression for the average electron velocity:

$$\frac{1}{\bar{\beta}} \cong 1 + \frac{1}{2\gamma^2} + \frac{K^2}{4\gamma^2}$$

results in the following interference condition:

$$\boxed{\lambda = \frac{\lambda_o}{2\gamma^2}\frac{1}{n}\left(1 + \frac{K^2}{2} + \gamma^2\theta^2\right)} \tag{4}$$

where $n = 1, 2, 3$ ..etc. is the harmonic number. From this we can obtain the following expressions for the radiation wavelength and photon energy in practical units:

$$\lambda[\text{Å}] = 1305.6\ \frac{\lambda_o}{E^2_{[GeV]}}\frac{1}{n}\left(1+\frac{K^2}{2}+\gamma^2\theta^2\right) \quad \text{and} \quad \varepsilon[\text{eV}] = 9.498\, n\ \frac{E^2_{[GeV]}}{\lambda_o\left(1+K^2/2+\gamma^2\theta^2\right)}$$

The interference condition tells us immediately several important facts about the radiation from insertion devices:

- The fundamental wavelength of the radiation is very much shorter than the period length of the device, because of the large γ^2 term (for electrons, $\gamma = 1957\ E$ [GeV])
- The wavelength of the harmonics can be varied either by changing the electron beam energy (γ) or the insertion device field strength, and hence K value.
- The wavelength varies with observation angle. Overall therefore the spectrum covers a wide range of wavelength. However, if the range of observation angles is restricted using a "pinhole" aperture, the spectrum will show a series of lines at harmonic frequencies.

The interference model can supply further information about the spread in wavelength and angles as follows. If the insertion device consists of N periods in a length L the condition for constructive interference over the entire length becomes:

$$\frac{L}{\overline{\beta}} - L\cos\theta = nN\lambda \tag{5}$$

Now we ask at what value of wavelength (λ') the interference becomes destructive. This is obtained when there is one complete extra wavelength of wavefront separation, i.e. 2π phase advance, over the length of the device:

$$\frac{L}{\overline{\beta}} - L\cos\theta = nN\lambda' + \lambda' \tag{6}$$

Subtracting Eqs. (5) and (6) yields the range of wavelengths at fixed angle θ:

$$\frac{\Delta\lambda}{\lambda} = \frac{1}{nN}$$

Similarly, changing angle θ at fixed wavelength results in destructive interference when:

$$\frac{L}{\overline{\beta}} - L\cos\theta' = nN\lambda + \lambda \tag{7}$$

Subtracting Eqs. (7) and (5) gives $\Delta(\theta^2) = 2\lambda/L$. In the special case of radiation with the on-axis wavelength (i.e. $\theta = 0$) the width therefore becomes:

$$\Delta\theta = \sqrt{\frac{2\lambda}{L}} = \frac{1}{\gamma}\sqrt{\frac{1+K^2/2}{iN}}$$

The cone of radiation at this wavelength can therefore be significantly smaller in opening angle compared to that of conventional synchrotron radiation (~ $1/\gamma$), a first indication of the high brightness of such sources.

2.2 Electron rest frame

Another model that gives a simple understanding of the properties of undulator radiation is to consider the electron motion in the frame that moves with the electron's average velocity along the axis, $\bar{\beta} c$. The electron sees the undulator approaching with relativistic factor $\bar{\gamma}$ where:

$$\bar{\gamma} = \frac{1}{\left(1-\bar{\beta}^2\right)^{1/2}} \cong \frac{\gamma}{\left(1+K^2/2\right)^{1/2}}$$

The undulator period appears Lorentz contracted with period length $\lambda_o/\bar{\gamma}$. In the moving frame the electron is therefore caused to oscillate with this wavelength, emitting a dipole radiation pattern. The transformation to the lab. frame involves a relativistic Doppler shift:

$$\lambda = \lambda' \bar{\gamma}(1-\bar{\beta}\cos\theta) = \frac{\lambda'}{2\bar{\gamma}}(1+\bar{\gamma}^2\theta^2)$$

Inserting the expression above for $\bar{\gamma}$ gives the same expression for the wavelength, Eq. (4).

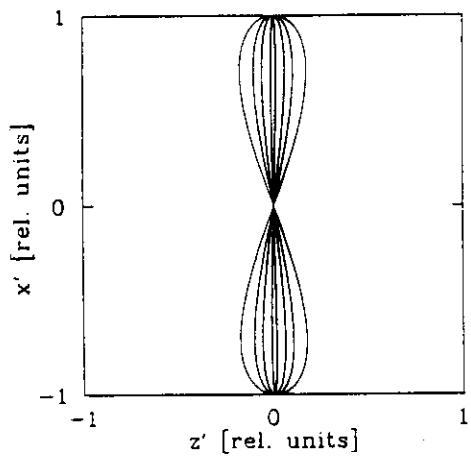

Fig. 4 Figure-of-eight motion in the frame of reference moving with the electron's average velocity, normalized to the same x' amplitude, for K = 0.1 (inner), 0.5, 1.0, 10.0 (outer)

In the moving frame the z oscillation amplitude is multiplied by a factor $\bar{\gamma}$ and so the ratio between the oscillation amplitudes in the two planes is given as follows:

$$\frac{\text{z' amplitude}}{\text{x' amplitude}} = \frac{\bar{\gamma}\left(\frac{K^2}{8\gamma^2}\frac{\lambda_o}{2\pi}\right)}{\left(\frac{K}{\gamma}\frac{\lambda_o}{2\pi}\right)} = \frac{K}{8(1+K^2/2)^{1/2}}$$

Thus, when K is small the oscillation is almost purely simple harmonic motion in the x-direction and as a result the radiation consists of a single harmonic. As K increases however the electron performs a "figure-of-eight" motion in the x'-z' plane (see Fig. 4) implying an increased emission at higher harmonic frequencies. Calculating the power emitted in the dipole mode [57] and comparing it to the total power emitted one obtains the ratio:

$$\frac{\text{power in the fundamental}}{\text{total power}} = \frac{1}{(1+K^2/2)^{1/2}}$$

which shows that the relative power in the fundamental decreases rapidly with increasing K value.

2.3 Electric field

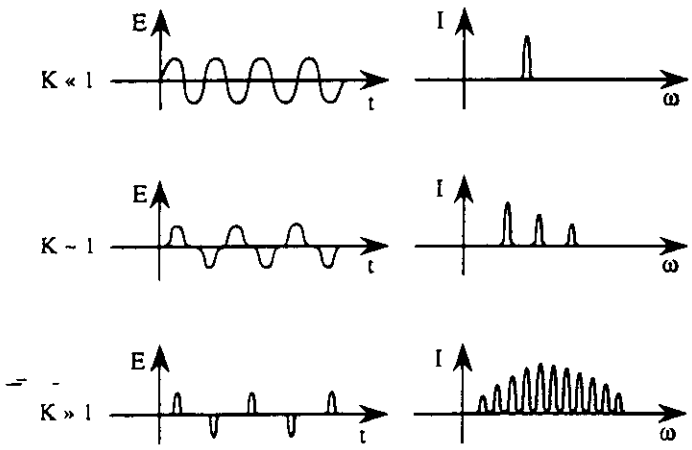

Fig. 5 Schematic diagram showing the electric field and corresponding radiation spectrum in devices with various K values

Another way of deducing some of the characteristics of the radiation is to consider in a qualitative way the electric field emitted by the electron. We imagine the electron moving on an oscillating trajectory with a maximum angular excursion of K/γ while emitting radiation into a cone with the typical opening angle of synchrotron radiation, ~ $1/\gamma$. It is reasonable to suppose therefore that for $K \leq 1$ an observer "sees" a continuous sinusoidal emission from the device. Correspondingly the radiation spectrum, which is the Fourier Transform of the electric field, consists of a single harmonic (see Fig. 5). At large K on the other hand the observer only detects radiation near the peaks in the trajectory, corresponding to the position of the magnet poles. In this case the electric field is strongly peaked and so the radiation spectrum contains a large number of harmonics.

We can also deduce from this picture the spectral width of the harmonics, as follows. The observed signal can be considered a continuous periodic signal multiplied by a "top-hat" function i.e. a function that is equal to unity within the range $\pm 2/T_o$, i.e. $\pm N/2\upsilon_1$ where υ_1 is fundamental frequency, and zero outside. According to the convolution theorem the Fourier Transform is the transform of the continuous signal convoluted with the transform for the top-hat function. The former consists of a series of lines at the harmonic frequencies, while the latter is a sinc function $(\sin(N\pi\upsilon/\upsilon_1)/\pi\upsilon_1)$ with a width in frequency that is inversely proportional to the length of the impulse: $\Delta\upsilon = 1/T_o = \upsilon_1/N$. After convolution each line has this same width, and so the relative width becomes $\Delta\upsilon/\upsilon = 1/nN$, in agreement with the result of section 2.1.

2.4 The high K limit

It is evident from the above that the number of harmonics in the spectrum increases as a function of the K value. The number can be estimated by comparing the equation for the wavelength of the harmonics, Eq. (4), with that of the critical wavelength for conventional synchrotron radiation corresponding to the peak field amplitude [58]:

$$\lambda_c = \frac{4\pi mc}{3\gamma^2 e B_o}$$

The harmonic number corresponding to a given wavelength is then as follows:

$$n = \frac{(3/4)K(1+K^2/2)}{(\lambda/\lambda_c)}$$

Table 1
Harmonic numbers giving a wavelength equal to the critical wavelength ($\lambda = \lambda_c$) as a function of K.

K	n
1	1
2	5
3	12
5	51
10	383
20	3015

We can get an idea of the number of harmonics in the spectrum by calculating the harmonic number corresponding to the critical wavelength, $\lambda = \lambda_c$. Table 1 shows that the number increases very rapidly with the K value. Since the harmonics are equally spaced in frequency $(\omega_1, 2\omega_1, 3\omega_1, 4\omega_1 \ldots)$ at high harmonic numbers they are relatively closer together $(\Delta\omega/\omega = 1/n)$ making it easier for the interference structure to become smoothed-out, resulting in a spectrum similar to that of a bending magnet. Interference effects will always remain however around the fundamental and low order harmonics. Thus, a device with relatively large K value ($K \geq 5$) can exhibit both strong interference effects near the fundamental as well as a quasi-smooth spectrum at high harmonic numbers. The degree of smoothing that occurs will be discussed in more detail in Section 3.7.

A note on nomenclature:

In the context of synchrotron radiation sources devices with low K values are traditionally called "undulators" while those with high K values are generally called "multipole wigglers" or simply "wigglers". It should be clear from the descriptions above however that there is no fundamental distinction between them. Unfortunately there is no universal agreement over nomenclature, which is further confused by the fact that magnets employed in free-electron lasers are often (particularly in the USA) called "wigglers", rather than the more historically accurate term "undulators".

3. RADIATION FROM INSERTION DEVICES: DETAILED ANALYSIS

3.1 Spectral/angular distribution

The energy radiated by a single electron during one passage through an undulator, per unit solid angle ($d\Omega$), per unit frequency interval ($d\omega$) is given by the Fourier Transform of the electric field seen by the observer [59]:

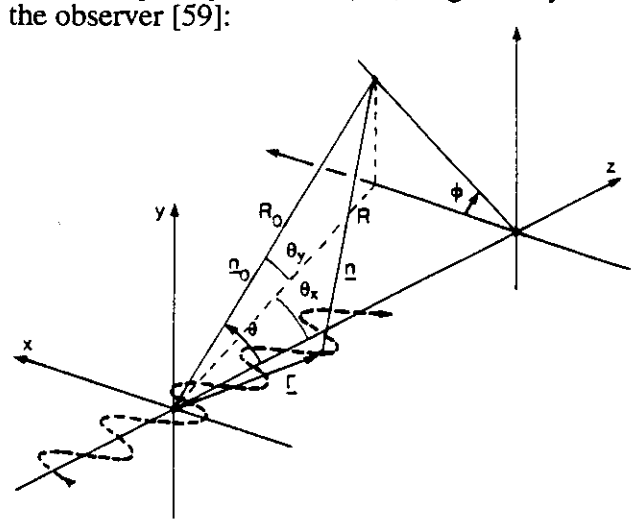

Fig. 6 Geometry for the analysis of undulator radiation

$$\frac{d^2I}{d\omega\, d\Omega} = \frac{c}{4\pi^2}\left|\int_{-\infty}^{\infty} R\,E(t)\,e^{i\omega t}\,dt\right|^2 \tag{8}$$

The electric field seen by the observer at time t is related to the electron acceleration at the earlier emission time, conventionally referred to as the "retarded time", $t_{ret.}$, as follows:

$$E(t) = \frac{e}{\sqrt{4\pi\varepsilon_o c}}\left[\frac{\hat{n}\wedge\{(\hat{n}-\beta)\wedge\dot{\beta}\}}{(1-\hat{n}\cdot\beta)^3 R}\right]_{t_{ret.}} \tag{9}$$

where $\hat{n} = (\sin\theta\cos\phi,\ \sin\theta\sin\phi,\ \cos\theta)$ is the unit vector from the point of emission to the observer (see Fig. 6). The observer and emission times are related by: $t = t_{ret.} + R/c$ where R is the distance between the emission and observer points, and hence:

$$\frac{d^2\bar{I}}{d\omega\, d\Omega} = \frac{e^2 c}{(4\pi\varepsilon_o)4\pi^2}\left|\int_{-\infty}^{\infty}\left[\frac{\hat{n}\wedge\{(\hat{n}-\beta)\wedge\dot{\beta}\}}{(1-\hat{n}\cdot\beta)^3}\right]_{t_{ret.}} e^{i\omega t}\,dt\right|^2 \tag{10}$$

In cases in which the observer is not very far from the source, the observation angle $\hat{n}$ must be considered to be a variable in the equation above, leading to additional "near-field" effects [60]. For most cases however it is possible to consider only the "far-field" case with $\hat{n}$ constant. In this case we can write $R = R_o - \hat{n}_o \cdot r$ and hence, ignoring a constant phase term:

$$t = t_{ret.} - \hat{n}_o \cdot r/c$$

from which it also follows that

$$\frac{dt}{dt_{ret.}} = 1 - \hat{n}_o \cdot \beta \tag{11}$$

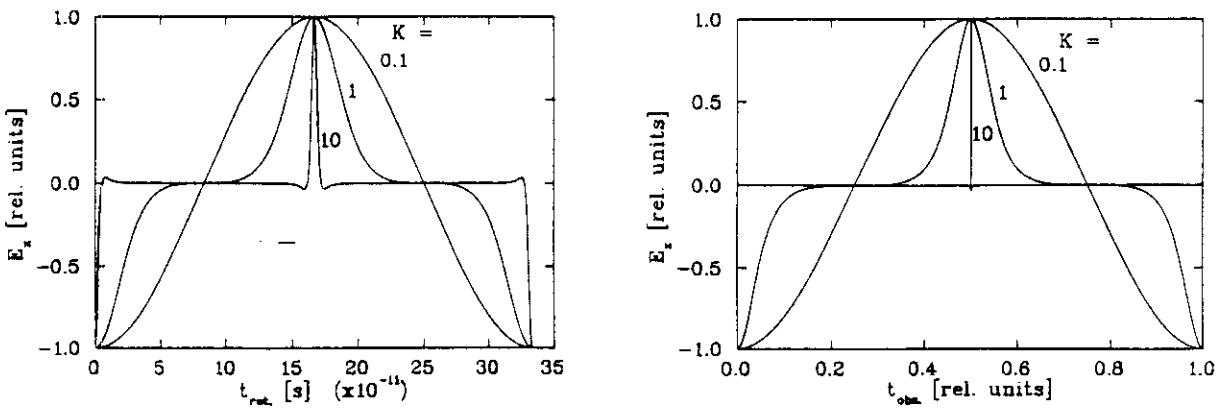

Fig. 7 Electric field calculated using Eq. (9) for one period in an undulator (λ_o = 0.1 m, E = 2 GeV) expressed in terms of the emission or retarded time (left) and observer time (right), normalized to the same time period

At this point we make a brief aside to examine the effect of the difference between the emission and observer time on the electric field distribution. Figure 7 (left) shows the calculated electric field for insertion devices with various K values. As already anticipated in section 2.3, the field is essentially sinusoidal for small K values and becomes sharply peaked for large K values. This is even more evident when expressed in terms of the observer time, as shown in Fig. 7 (right). Here the time axis has been normalized to a unit time period because of the large

difference between the three cases. At small K the pattern remains sinusoidal, but at large K it becomes extremely sharply peaked. The reason for this behaviour is the varying "time compression" factor [43], Eq. (11), relating the emission and observer times, which for small angles between the direction of motion and the angle of observation can be expressed as:

$$\frac{dt_{ret.}}{dt} = \frac{2\gamma^2}{\left(1+\gamma^2\theta^2\right)}$$

Thus, for small K and for large K in the region of the poles when the angle θ is close to zero, the time scales are compressed by the large factor $2\gamma^2$. For most of the trajectory however in the case of large K the factor is much smaller since the electrons are not travelling in the direction of observation. On an absolute scale therefore the electric field emission close to the peaks remains the same as in Fig. 7 (left). The difference in Fig. 7 (right) is due to the much longer time *between* the peaks (in terms of the observer time) for large K than for small K, which is reflected in the longer wavelength of the radiation.

Returning to the calculation of the spectral and angular distributions, the result expressed in terms of the emitter time is then as follows:

$$\frac{d^2I}{d\omega\, d\Omega} = \frac{e^2}{(4\pi\varepsilon_o)4\pi^2 c}\left|\int_{-\infty}^{\infty} \frac{\hat{n}\wedge\{(\hat{n}-\beta)\wedge\beta\}}{(1-\hat{n}\cdot\beta)^2}\, e^{i\omega(t-\hat{n}\cdot r/c)}\, dt\right|^2 \qquad (12)$$

where from now on it is also to be understood that $\hat{n} = \hat{n}_o$. This equation, or the more general Eq. (10), can be used directly for numerical calculation: having specified the magnetic field of the device, the electron motion $(r,\beta,\dot{\beta})$ can be computed and then the integration above can be performed.

A further simplification can generally be made, by integrating the above expression by parts, after which one obtains [59]:

$$\frac{d^2I}{d\omega\, d\Omega} = \frac{e^2\,\omega^2}{(4\pi\varepsilon_o)4\pi^2 c}\left|\int_{-\infty}^{\infty} \{\hat{n}\wedge(\hat{n}\wedge\beta)\}\, e^{i\omega(t-\hat{n}\cdot r/c)}\, dt\right|^2 \qquad (13)$$

In the case of a periodic magnet the integral for each period is the same, apart from a phase factor and hence we can write:

$$\frac{d^2I}{d\omega\, d\Omega} = \frac{e^2\,\omega^2}{(4\pi\varepsilon_o)4\pi^2 c}\left|\int_{-\lambda_o/2\bar{\beta}c}^{\lambda_o/2\bar{\beta}c} \{\hat{n}\wedge(\hat{n}\wedge\beta)\}\, e^{i\omega(t-\hat{n}\cdot r/c)}\, dt\right|^2 \left|(1+e^{i\delta}+e^{i2\delta}+e^{i3\delta}+\ldots.e^{i(N-1)\delta})\right|^2$$

where the phase increase between one period and the next is given by:

$$\delta = \omega\left(T - \frac{\lambda_o\cos\theta}{c}\right) = \omega\left(\frac{\lambda_o}{\bar{\beta}\,c} - \frac{\lambda_o\cos\theta}{c}\right)$$

which can be expressed in terms of the fundamental frequency, using Eq. (4), as follows:

$$\delta = \frac{2\pi\omega}{\omega_1(\theta)}$$

The geometric series of phase factors can be simplified as follows:

$$\left|(1+e^{i\delta}+\ ....e^{i(N-1)\delta})\right|^2 = \frac{\sin^2 N\delta/2}{\sin^2 \delta/2} = \frac{\sin^2 N\pi\omega/\omega_1}{\sin^2 \pi\omega/\omega_1} \tag{14}$$

This function, sometimes called the "grating function" in analogy with diffraction from a grating or crystal, represents the interference between successive periods [61,62], and selects a narrow range of frequencies and angles near the harmonics, i.e. $\omega = n\omega_1(\theta)$, as shown in Fig. 8 (left). The lineshape for each harmonic is the same which we can express as follows, normalized to unit amplitude:

$$L(N\Delta\omega/\omega_1(\theta)) = \frac{\sin^2(N\pi\Delta\omega/\omega_1(\theta))}{N^2\sin^2(\pi\Delta\omega/\omega_1(\theta))} \tag{15}$$

where $\Delta\omega = \omega - n\omega_1(\theta)$. For reasonably large values of N ($\geq$ 10) the shape becomes independent of N and can be expressed in terms of a single variable $N\Delta\omega/\omega_1(\theta)$, as shown in Fig. 8 (right).

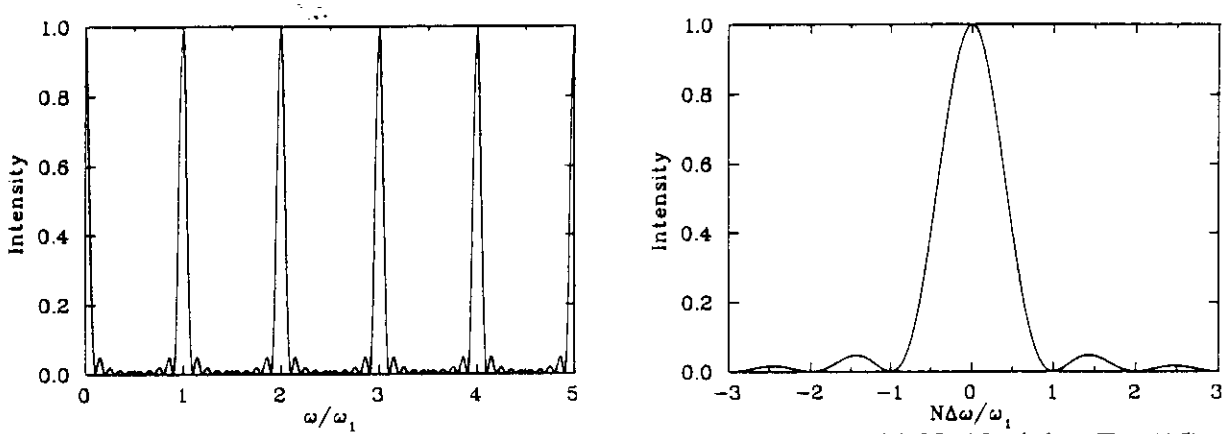

Fig. 8 Undulator radiation interference functions: left - Eq. (14) with N=10, right - Eq. (15)

The remaining part of the integral is a more smoothly varying function and so need only be evaluated at the harmonic frequencies, and thus becomes a function only of observation angle, $\hat{n}$, and harmonic number. As in the case of Eq. (12) the integration can of course be carried out numerically, in which case any form of magnetic field distribution can be used. One can also proceed analytically in the case of a pure sinusoidal motion [14, 63] (see Appendix). The result can be expressed in the following form:

$$-\frac{d^2I}{d\omega\, d\Omega} = \frac{e^2\gamma^2N^2}{(4\pi\varepsilon_o)c}\, L(N\Delta\omega/\omega_1(\theta))\; F_n(K,\theta,\phi) \tag{16}$$

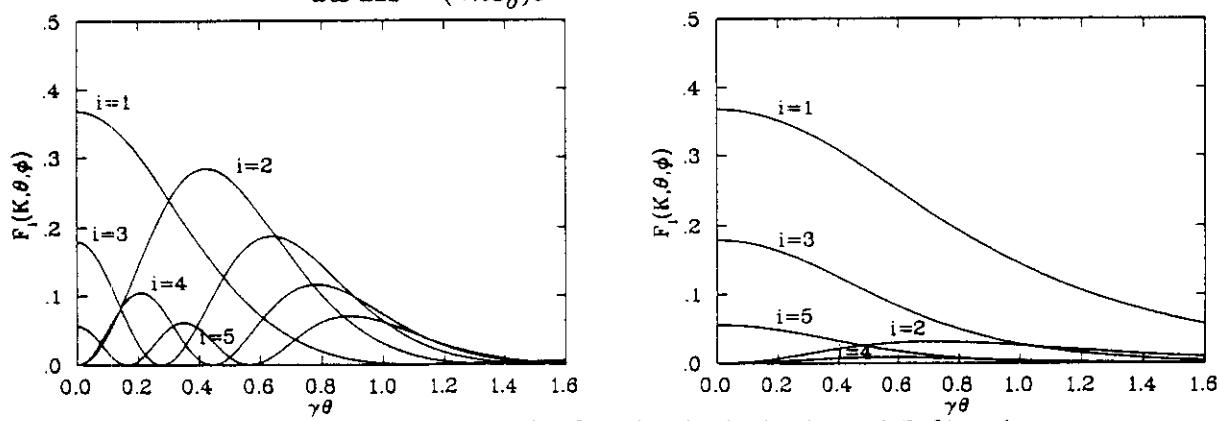

Fig. 9 Angular flux density function in the horizontal (left) and vertical (right) planes for the case K = 1

The function $F_n(K,\theta,\phi)$ is smoothly varying in the vertical plane, but is an oscillatory function with n peaks in the horizontal plane, as shown in Fig. 9. The complex structure in the horizontal plane arises from the interference of the emission from the two poles within each period [64].

On-axis the expression simplifies to the following:

$$\frac{d^2I}{d\omega\, d\Omega} = \frac{N^2 e^2 \gamma^2}{(4\pi\varepsilon_o)c} L(N\Delta\omega/\omega_1(\theta))\, F_n(K)$$

where:

$$F_n(K) = \frac{n^2K^2}{(1+K^2/2)^2}\left[J_{\frac{n+1}{2}}(Z) - J_{\frac{n-1}{2}}(Z)\right]^2 \quad \text{and} \quad Z = \frac{nK^2}{4(1+K^2/2)}$$

It is interesting to note that if we neglect the longitudinal oscillation, i.e. $Z = 0$, the result would be only a single harmonic on-axis, $n = 1$. We can say therefore that the higher harmonics on-axis arise as a direct result of the z-motion, whose amplitude increases as K increases. Figure 10 shows the on-axis angular flux density function $F_n(K)$, which again indicates that the higher harmonics become more important as K increases.

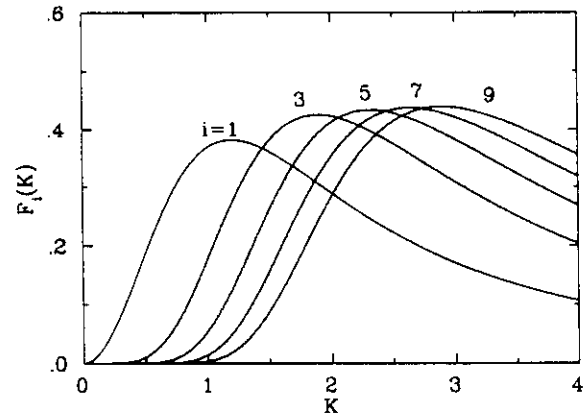

Fig. 10 On-axis angular flux density function

The expression above gives the energy radiated (Joules) by the passage of a single electron through the undulator. Multiplying by the number of electrons passing per second, I_b/e, where I_b is the average beam current (Amps), gives the radiated power (Watts). It is more usual however to express the intensity in terms of the photon flux, the number of photons per second, $\dot{n}$: dividing by the photon energy $\hbar\omega$ gives the photon flux per unit bandwidth, or alternatively dividing by $\hbar$ gives the photon flux per unit relative bandwidth. Finally we obtain in practical units of photons/s/mrad^2/0.1% bandwidth:

$$\left.\frac{d^2\dot{n}}{d\omega/\omega\; d\Omega}\right|_{\theta=0} = 1.744\ 10^{14}\ N^2\ E^2_{[GeV]}\ F_n(K)\ I_b$$

3.2 Total flux

It is also of interest to know how much total flux is available at a given wavelength. We can obtain an approximate expression by assuming that the intensity variation off-axis is determined only by the lineshape function, Eq. (15), which is a function of both frequency and angle:

$$L\left(N\frac{\Delta\omega}{\omega_1(\theta)}\right)=L\left(N\frac{\Delta\omega}{\omega_1(0)}+\frac{L\theta^2}{2\lambda}\right) \tag{17}$$

where the "detuning parameter" $\Delta\omega/\omega_1(0)=(\omega-n\omega_1(0))/\omega_1(0)$ is the difference between the frequency and the on-axis value. Integrating over angle we obtain:

$$\int_0^{\infty}\int_0^{2\pi} L(N\Delta\omega/\omega_1(0))\ \theta\,\mathrm{d}\theta\,\mathrm{d}\phi=\frac{2\pi\lambda}{L}f(N\Delta\omega/\omega_1(0))$$

We obtain therefore in practical units of photons/s/0.1% bandwidth:

$$\frac{-\,d\dot{n}}{d\omega/\omega}=1.431\ 10^{14}\ N\ Q_n(K)f(N\Delta\omega/\omega_1(0))\ I_b \tag{18}$$

where $Q_n(K)=(1+K^2/2)F_n(K)/n$. The flux function $Q_n(K)$ and the detuning function $f(N\Delta\omega/\omega_1(0))$ are shown in Fig. 11. It can be seen that for zero detuning (i.e. $\omega=\omega_n(0)$) the flux is very close to half of the usually quoted result. Nearly twice as much flux can be obtained however by a small detuning to lower frequency by approximately $\Delta\omega/\omega_1(0)\cong -1/N$.

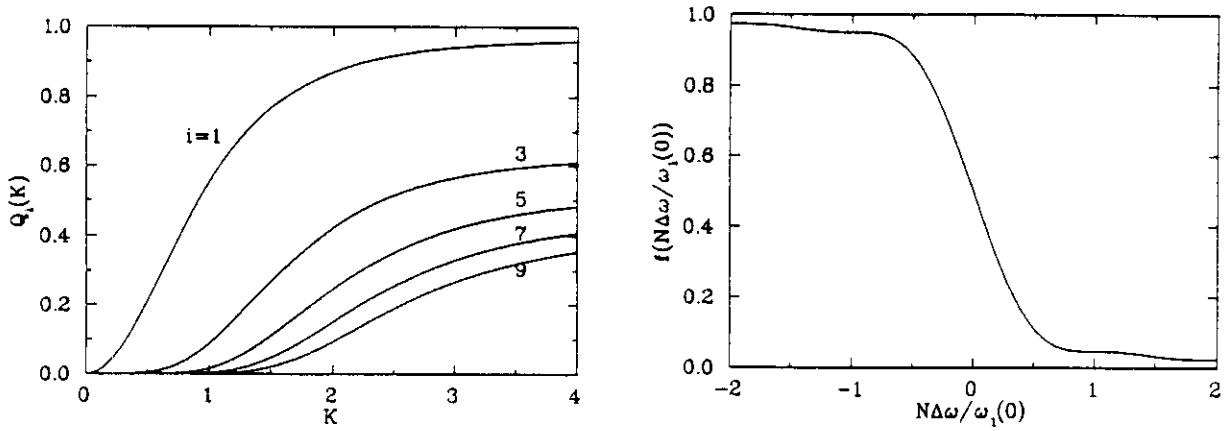

Fig. 11 Undulator flux function (left) and flux as a function of detuning (right)

It is interesting to compare these results with that of a simple bending magnet source. The peak bending magnet angular flux density is given approximately by $1.95\ 10^{13}\ E^2_{[GeV]}\ I_b$, in the same units as above. The ratio between the undulator and the peak bending magnet angular flux density is therefore $8.9\ N^2\ F_n(K)$. For example, the angular flux density of an undulator with 50 periods and $K=1$ exceeds that of a bending magnet by nearly 4 orders of magnitude. The peak bending magnet flux, integrated over all vertical angles, is given approximately by $2.23\ 10^{13}\ E_{[GeV]}\ I_b$ per mrad horizontal. The ratio in this case is therefore $6.4\,N\,F_n(K)(1+K^2/2)/n\,E_{[GeV]}$. The same undulator as above in a 2 GeV ring gives approximately an order of magnitude higher flux on its first harmonic than the maximum flux per mrad from a bending magnet source. We can begin to appreciate therefore not only the higher flux, but particularly the much higher brightness of the undulator source compared to a bending magnet.

3.3 Brightness and the effect of electron beam emittance

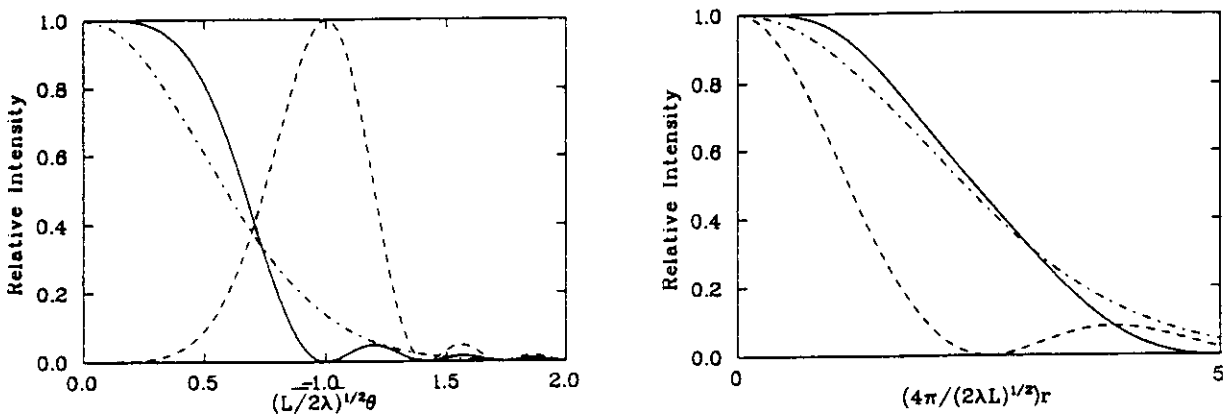

Fig. 12 Intensity as a function of angle (left) and position (right).
Solid lines - zero detuning, dashed lines - detuning of $\Delta\omega/\omega_1(0) \cong -1/N$,
dot-dashed lines - Gaussian approximations for zero detuning (see text)

We start by considering the effect of the electron beam divergence on the angular flux density. In general a numerical approach is required in order to carry out the 2-dimensional convolution of the complex angular distribution of the radiation with the Gaussian electron beam. We can however derive an approximate result by considering that the radiation also has a Gaussian distribution. Figure 12 (left) shows the approximate form of the angular distribution of the radiation as determined by the lineshape function, for zero detuning and for a detuning of $\Delta\omega/\omega_1(0) \cong -1/N$. It is clear that a Gaussian approximation is only valid at zero-detuning, and even then is not very accurate. The dashed line shows a Gaussian approximation for the zero-detuning case with standard deviation, $\sigma'_R = \sqrt{\lambda/2L}$. The significance of this value is that it gives the correct ratio between integrated flux and peak angular flux density:

$$\frac{d\dot{n}/(d\omega/\omega)}{d^2\dot{n}/(d\omega/\omega)d\Omega\big|_{\theta=0}} = 2\pi\sigma'^2_R = \pi\frac{\lambda}{L}$$

Using the Gaussian approximation above the effective divergences of the source become simply:

$$\Sigma'_x = \sqrt{\sigma'^2_x + \sigma'^2_R} \qquad \Sigma'_y = \sqrt{\sigma'^2_y + \sigma'^2_R}$$

where σ'_x, σ'_y are the rms angular divergences of the electron beam. The total flux remains constant and so we can write the expression for the modified on-axis angular flux density including electron beam divergence as follows:

$$\frac{d^2\dot{n}}{d\omega/\omega\, d\Omega}\bigg|_{\theta=0} = \frac{d\dot{n}/(d\omega/\omega)}{2\pi\,\Sigma'_x\,\Sigma'_y}$$

The radiation brightness includes not only the angular divergence of the source but also the emitting source size. The standard unit of measurement is thus photons/s/mm^2/mrad^2/0.1% bandwidth. The most simple view of how the size of the source comes about, is to consider projecting the angular cone of the radiation to the centre of the undulator. We might expect therefore a spatial distribution at the centre of size $\sigma_R \sim \sigma'_R L/2$, and hence with the above expression for σ'_R, we obtain $\sigma_R \sim \sqrt{2\lambda L}/4$. The correct approach however is to integrate the wave amplitudes, in the same way as one calculates diffraction from an aperture. The spatial distribution is thus given by:

$$I(r) = \left| \frac{1}{\lambda} \int_0^{\infty} \int_0^{2\pi} A(\theta,\phi) e^{-i2\pi(\hat{n}\cdot r)/\lambda_o} \, \theta \, d\theta \, d\phi \right|^2$$

Carrying out this calculation with the angular distribution given by Eq. (15) results in the functions shown in Fig. 12 (right). The zero-detuning case can be approximated well by a Gaussian with standard deviation $\sigma_R = \sqrt{2\lambda L}/2\pi$, i.e. very similar to the simple result above. The effective source sizes are then given by the convolution with the electron beam dimensions, σ_x, σ_y, i.e.:

$$\Sigma_x = \sqrt{\sigma_x^2 + \sigma_R^2} \qquad \Sigma_y = \sqrt{\sigma_y^2 + \sigma_R^2}$$

Combining the information about source size with the angular flux density allows us to estimate the brightness, as follows:

$$B = \frac{dn/(d\omega/\omega)}{4\pi^2 \, \Sigma_x \Sigma_y \Sigma'_x \Sigma'_y}$$

The limiting cases of the above equation are:

i/ $\sigma_R > \sigma_{x,y}$ and $\sigma'_R > \sigma'_{x,y}$. At long wavelength and with small electron beam dimensions and divergences the natural radiation dimensions dominate; this is often referred to as the "diffraction limit".

ii/ $\sigma_R < \sigma_{x,y}$ and $\sigma'_R < \sigma'_{x,y}$. At the other extreme case the brightness is dominated by the electron beam emittance, and we can write in the usual case (insertion device at a symmetry point with zero dispersion) $B = Flux/4\pi^2\varepsilon_x\varepsilon_y$, where $\varepsilon_x = \sigma_x \sigma'_x$, $\varepsilon_y = \sigma_y \sigma'_y$ are the electron beam emittances in the two planes.

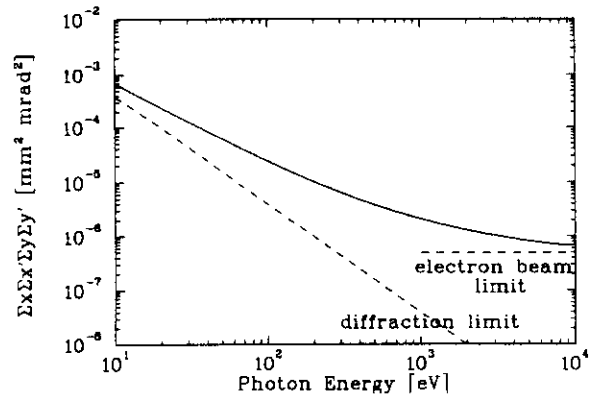

Fig. 13 Product of photon beam emittances in the case of ELETTRA

Both extremes are indicated in Fig. 13 which shows the variation of the denominator in the above expression, $\Sigma_x \Sigma_y \Sigma'_x \Sigma'_y$, as a function of photon energy using the parameters of ELETTRA as representative of "third-generation" synchrotron radiation facilities, compared to the result for a zero emittance electron beam. At low photon energies therefore the radiation is close to being diffraction limited, while at high energies the electron beam emittance is clearly the limiting factor.

It must be remembered that for various reasons the expression for the brightness is only an approximation. It has already been shown that away from the condition of zero-detuning, the angular distribution function becomes strongly non-Gaussian, as shown in Fig. 12(left). Under these conditions it is difficult to arrive at a sensible definition of the effective standard deviation which gives the correct convolution with the electron beam divergence. The calculation of the source size also should take into account the effect of detuning. A further problem is that, as

already noted, no account is taken of the off-axis angular distribution function $F_n(K,\theta,\phi)$ which can have a significant effect on the overall angular distribution particularly when n is large and N is small. Finally, another potentially important effect is not included, namely the electron beam energy spread. A better approximation can therefore be made by making a numerical calculation of the on-axis angular flux density (see section 3.6), including the true angular distribution function and the effects of emittance and energy spread, and then applying an approximate calculation of the source size, i.e. defining the brightness as:

$$B = \frac{d^2\dot{n}/(d\omega/\omega)d\Omega}{2\pi\,\Sigma_x\,\Sigma_y}$$

To go beyond these approximate treatments requires a more fundamental definition of the brightness in terms of the electric field distribution [65] which however is outside the scope of the present discussion.

3.4 Coherence

The degree of coherence of the radiation beam is an increasingly important parameter for various synchrotron radiation experiments. Basically, there are two measures of coherence - temporal (or longitudinal) coherence and spatial (or transverse) coherence. Temporal coherence determines the extent to which two parts of a beam, one delayed with respect to the other, can mutually interfere. Spatial coherence on the other hand determines the extent to which two spatially separated (but not delayed) parts can interfere. Temporal coherence is determined by the degree of monochromaticity of the radiation, and is described by the longitudinal coherence length over which waves of different wavelength remain in phase:

$$l_s = \frac{\lambda^2}{2\,\Delta\lambda}$$

In most cases this is determined by the monochromator bandwidth, which is usually considerably smaller than the linewidth of the undulator radiation.

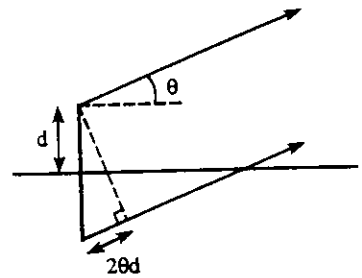

Fig. 14 Definition of spatial coherence in terms of phase-space area

Spatial coherence is determined by the phase-space area of the source. Simple geometry is sufficient to show that only waves which are emitted from an area with half-size d and half angle θ where $2d\theta \leq \lambda/4$ are in phase, and hence coherent (Fig. 14). It follows therefore from the definitions above that the amount of spatially coherent flux is directly proportional to the brightness. The minimum obtainable product of size and divergence is defined by the Uncertainty Principle and is represented by the fundamental (Gaussian) mode of a laser resonator, for which $\sigma_R\,\sigma'_R = \lambda/4\pi$. Such a beam has therefore complete spatial coherence. According to the definitions above, undulator radiation, in the absence of electron beam emittance, has a product of approximately $\sigma_R\,\sigma'_R = \lambda/2\pi$. The radiation is nevertheless completely spatial coherent, since it is a single radiation pattern from a single electron. Partial coherence results only when a summation is taken over many electrons in an electron beam. We can therefore write that the coherent flux is given approximately as follows:

$$F_{coh.} = B\left(\frac{\lambda}{2\pi}\right)^2$$

and hence also that the fraction of coherent flux is:

$$\frac{F_{coh.}}{F_{tot.}} = \frac{(\lambda/2\pi)^2}{4\pi^2 \Sigma_x \Sigma_y \Sigma'_x \Sigma'_y}$$

A more detailed treatment of brightness and coherence aspects can be found in Refs. [45, 65].

3.5 Power and power density

The instantaneous power radiated per unit solid angle in the direction $\hat{n}$ by a single electron in arbitrary motion in a magnetic field (i.e. with no acceleration) is given as follows [66]:

$$\frac{dP}{d\Omega} = \frac{e^2}{(4\pi\varepsilon_o)4\pi c}\left[\frac{\dot{\beta}^2}{(1-\hat{n}\cdot\beta)^3} - \frac{(\hat{n}\cdot\dot{\beta})^2}{\gamma^2(1-\hat{n}\cdot\beta)^5}\right]$$

After integrating over the length of the insertion device to get the energy radiated per unit solid angle, and multiplying by I_b/e to get the power radiated by a beam of electrons in the insertion device, the result can be expressed in the following form in practical units [67]:

$$\frac{dP}{d\Omega}[\mathrm{W/mrad^2}] = 13.44\ 10^{-3}\ E^4_{[GeV]}\, I_b \int\left[\frac{\upsilon_x'^2 + \upsilon_y'^2}{D^3} - \frac{(\upsilon_x^2)' + (\upsilon_y^2)'}{D^5}\right]dz \qquad (19)$$

where $\upsilon_x(z) = \gamma(\beta_x - \theta_x)$, $\upsilon_y(z) = \gamma(\beta_y - \theta_y)$, $D = 1 + \upsilon_x^2 + \upsilon_y^2$ and where the prime indicates the derivative with respect to z.

In the case of a plane sinusoidal device $\upsilon_x = K\sin\alpha - \gamma\theta_x$ and $\upsilon_y = -\gamma\theta_y$, where $\alpha = 2\pi z/\lambda_o$. After some simplification the result becomes:

$$\frac{dP}{d\Omega}[\mathrm{W/mrad^2}] = 13.44\ 10^{-3}\ E^4_{[GeV]}\, I_b \frac{2\pi}{\lambda_o} N K^2 \int_{-\pi}^{\pi} \cos^2\alpha \left[\frac{1}{D^3} - \frac{4(\gamma\theta_x - K\sin\alpha)^2}{D^5}\right]d\alpha$$

where $D = 1 + (\gamma\theta_y)^2 \pm (K\sin\alpha - \gamma\theta_x)^2$. This can be expressed in the following form:

$$\frac{dP}{d\Omega}[\mathrm{W/mrad^2}] = 10.84\ E^4_{[GeV]}\, B_o\, N\, I_b\, G(K)\, f_K(\theta_x, \theta_y)$$

where $G(K) = \dfrac{K(K^6 + \frac{24}{7}K^4 + 4K^2 + \frac{16}{7})}{(1+K^2)^{7/2}}$ and

$f_K(\theta_x, \theta_y) = \dfrac{16K}{7\pi G(K)} \displaystyle\int_{-\pi}^{\pi} \sin^2\alpha \left[\frac{1}{D^3} - \frac{4(\gamma\theta_x - K\cos\alpha)^2}{D^5}\right]d\alpha$, as obtained by Kim [68].

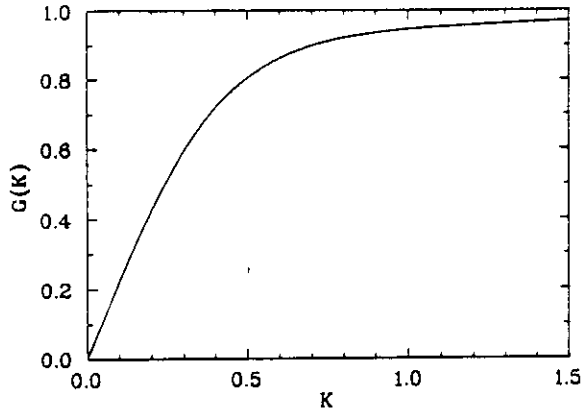

Fig. 15 The function $G(K)$

The function $G(K)$ is illustrated in Fig. 15 and is close to unity for $K > 1$. The function $f_K(\theta_x, \theta_y)$ has a peak value of unity on-axis and is shown in Fig. 16 in the horizontal and vertical planes for various K values. It can be seen that in the vertical plane the angular distribution is insensitive to the value of K and in the limit $K \to \infty$ is equal to that of a bending magnet. For large K in the horizontal plane the distribution becomes semi-circular, since the power density is proportional to the field at the corresponding tangent point: at an angle $\theta_x = (K/\gamma)\cos(kz)$ the field at the tangent point is $B = B_o \sin(kz)$ and hence $(B/B_o)^2 + (\gamma\theta_x/K)^2 = 1$.

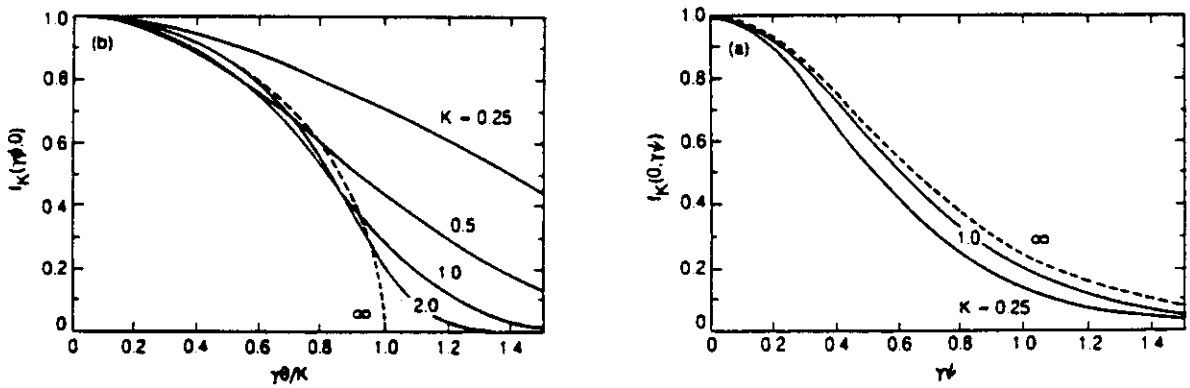

Fig. 16 Power density as a function of angle in the horizontal (left) and vertical (right) planes

The instantaneous rate of total power emitted by a single electron is given by the Liénard result (1898) [59]:

$$P = \frac{2}{3}\frac{e^2 c}{4\pi\varepsilon_o \rho^2}\beta^2\gamma^4$$

where ρ is the radius of curvature of the trajectory. Integrating over the insertion device length and converting to practical units we obtain:

$$P_{tot}[\mathrm{W}] = 1265.\ E^2_{[GeV]} \int B^2\, ds\, I_b \qquad (20)$$

in which B is the magnitude of the magnetic field, irrespective of its direction. For an insertion device of length L with sinusoidal field amplitude B_o we have then:

$$P_{tot}[\mathrm{W}] = 633.\ E^2_{[GeV]}\, B_o^2\, L\, I_b$$

Table 2
Total power $P_{tot.}$ (kW) and peak power density $d^2P/d\Omega$ (kW/mrad^2) for typical undulator and multipole wiggler parameters in storage rings of various energies; insertion device length = 3 m, beam current = 200 mA.

	$\lambda_o = 0.05$ m, $B_o = 0.5$ T		$\lambda_o = 0.15$ m, $B_o = 1.6$ T	
E(GeV)	$P_{tot.}$	$d^2P/d\Omega$	$P_{tot.}$	$d^2P/d\Omega$
0.8	0.06	0.03	0.62	0.03
2.0	0.38	1.0	3.9	1.1
6.0	3.4	84.3	35.0	89.9

Table 2 gives the power and power density emitted by a "typical" undulator and wiggler in rings of three different energies. It can be seen that the numbers increase rapidly with energy, particularly for the power density ($\sim E^4$). Multipole wigglers can emit significantly more total power than undulators (for the same length), however the peak power densities are similar because of the approximate inverse scaling of field strength with period length. Handling the very high power and power densities requires special designs for beamline components. Care must also be taken to prevent damage to the electron beam vacuum chamber in the event of beam mis-steering. Automatic interlock systems are therefore required to detect any unwanted electron beam movement and to dump the beam within a sufficiently short time interval.

3.6 Practical computation of radiation spectra

Various computer programs have been written that can calculate the spectral and angular distribution of undulator radiation using a number of different approaches:

i/ Direct numerical integration of Eqs. (10), (12) or (13) e.g. [69-71]
ii/ Calculation of the electric field in the time domain using Eq. (9) followed by Fourier Transformation to obtain the radiation spectrum e.g. [72,73]
iii/ Use of the analytic approximations for a pure sinusoidal field involving series of Bessel functions (see Appendix) e.g. [74, 75]
iv/ Other techniques e.g. [76-78]

Methods i/ and ii/ are applicable to the case of a real magnetic field and also for the near-field case, whereas method iii/ assumes an ideal sinusoidal magnetic field in the far-field case. The effect of electron beam emittance can be included either by numerical convolution or by Monte-Carlo methods. Each type of code has its particular advantages and disadvantages. Method iii/ for example is useful for a rapid calculation of the main effects of angular acceptance and electron beam effects, whereas i/ and ii/ are usually more time consuming but provide more detailed information on the effects of magnetic field errors etc. Methods i/ and iii/ can calculate also the angular distributions at a given frequency, which is not possible with method ii/. Some special techniques have been developed for the cases where the K value is large [76,77]. Here we will not discuss further the various numerical approaches, but rather present some results using one code [75] that illustrate the main features of the effects of angular acceptance and electron beam emittance and energy spread.

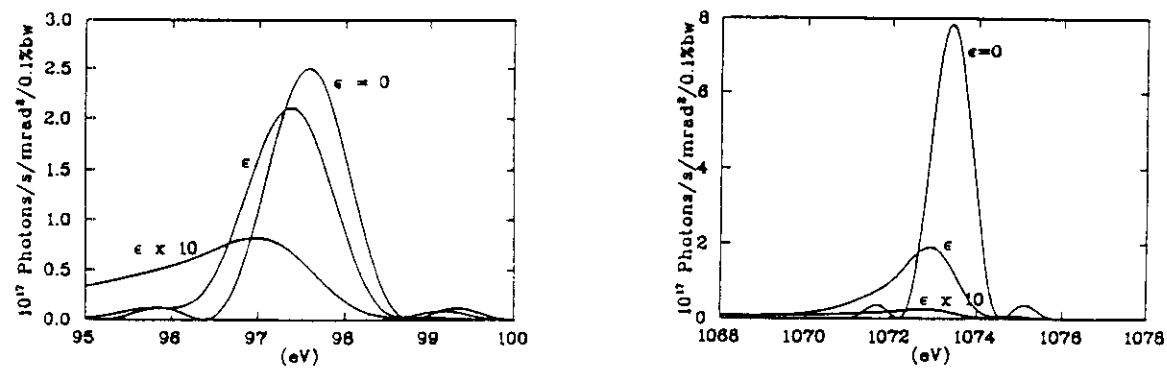

Fig. 17 Effect of electron beam emittance on the 1st (left) and 11th (right) harmonics for an undulator in ELETTRA; E = 2 GeV, λ_o = 56 mm, N = 81, K = 3.45

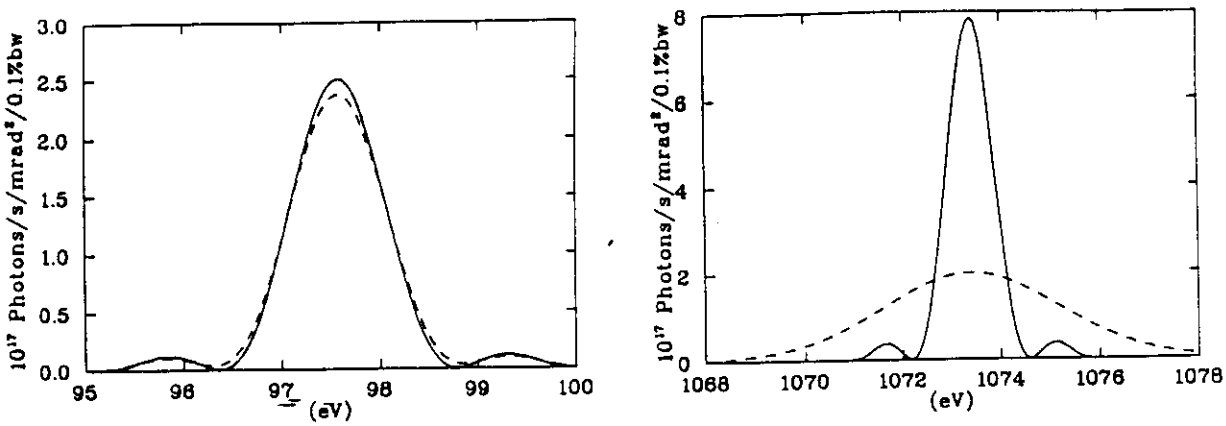

Fig. 18 Effect of electron beam energy spread on the 1st (left) and 11th (right) harmonics for an undulator in ELETTRA; parameters as Fig. 17

Figure 17 shows an example of the effect of electron beam emittance on the on-axis spectrum for an undulator installed on ELETTRA. It can be seen that with the nominal emittances there is a relatively small effect on the first harmonic (17% reduction), but this is much larger on the 11th harmonic (factor of 4 reduction). The effect of a ten-fold increase in emittance is also shown, which is sufficient to reduce the first harmonic by a factor of 3. Figure 18 illustrates the effect of electron beam energy spread, with zero emittance. The nominal energy spread gives rise to a negligible reduction in peak intensity on the first harmonic, but quite significant reduction (factor of 4) on the 11th harmonic. It should be noted that the effect of emittance is not symmetric, broadening the lineshape mainly on the long wavelength side, in accordance with Eq. (4), whereas the effect of energy spread is symmetric.

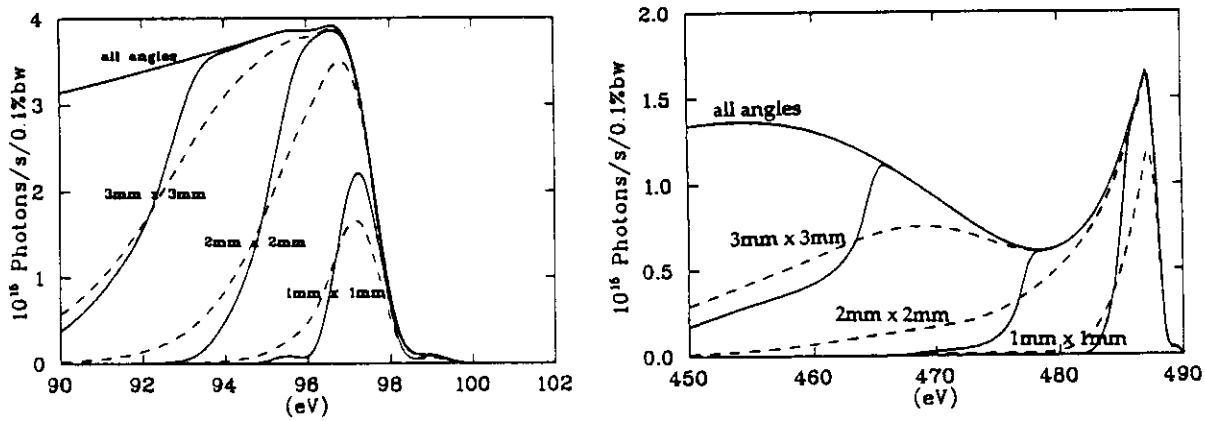

Fig. 19 Effect of "pinhole" size on the 1st (left) and 5th (right) harmonics for an undulator in ELETTRA; parameters as Fig. 17, distance from source 10 m

Finally, Fig. 19 (left) shows the effect of the size of the acceptance, both with and without electron beam emittance and energy spread included. As the pinhole size increases the peak flux increases up to a maximum value, whereas the line continues to widen. The calculated first harmonic on-axis photon energy is 97.6 eV and it can be seen that the flux at this energy is roughly one half of the maximum value which occurs with a detuning $\Delta\varepsilon/\varepsilon$ of approximately $1/N$, which in this case corresponds to about 1.2 eV, in agreement with the observations made in section 3.2. The same calculation is shown also for the 5th harmonic. In this case a smaller pinhole is needed to collect the same fraction of flux due to the smaller angular divergence of the source. With a large acceptance an extra peak appears in the spectrum due to the intensity maxima that occur off-axis in the horizontal plane, as shown in Fig. 9.

3.7 Wiggler regime

In this section we return in more detail to the question of when the interference effects which characterize an undulator spectrum become sufficiently "smoothed out" that the result is what may be termed the "wiggler" mode of operation. Generally this requires that there are a sufficient number of harmonics in the spectrum ($K \geq 5$) and that the frequency is not too close to the fundamental ($n \geq 10$). The possible effects that can help to smooth out the spectrum are as follows:

- wavelength acceptance: the relative spacing of the harmonics is $\Delta\omega/\omega = 1/n$ and so if the wavelength acceptance exceeds this value then the harmonics become smoothed out.
- angular acceptance: if the angular acceptance is sufficiently large the $n+1$'th harmonic off-axis can reach the wavelength of the n'th harmonic on-axis. It is easy to show that this occurs when $\gamma^2\theta^2 \geq (1+K^2/2)/n$.
- electron beam divergence: the same effect as the above occurs if the electron beam divergence becomes too large.
- electron beam energy spread: since the change in frequency is related to the electron energy by $\Delta\omega/\omega = 2\Delta E/E$, it follows that the spectrum is smoothed if $\Delta E/E \geq 1/2n$.
- magnetic field errors: random errors in the magnetic field distribution lead to an imperfect constructive interference, particularly for higher harmonics, which can also contribute to the transition between undulator and wiggler characteristics.

In most cases the bandpass of the monochromator is too small to have a significant effect, and the most dominant is the angular acceptance, followed by electron beam divergence and energy spread and magnetic field errors. It should be noted that the effects of angular acceptance and beam divergence are both much bigger in a higher energy ring whereas the other effects are energy independent.

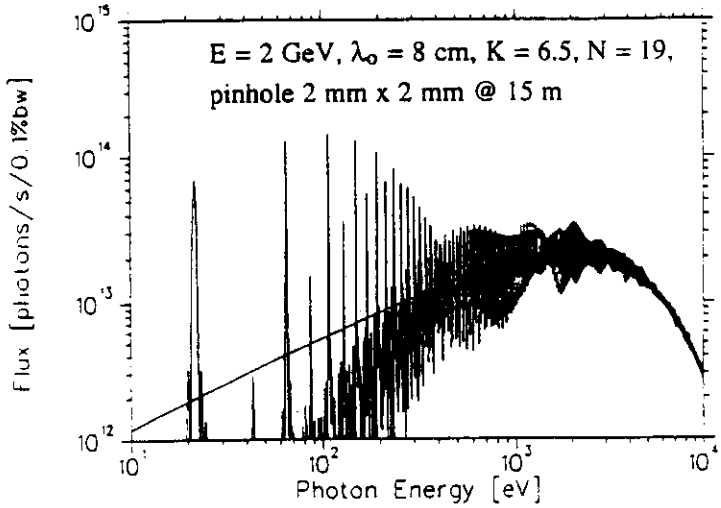

Fig. 20 Calculated spectrum for a high K device in ELETTRA

The resulting spectrum of a high K-device is therefore quite complex and can be described in terms of three regions:

- the fundamental and first few harmonics where there are strong interference effects
- the high photon energy region where the spectrum is essentially smooth
- an intermediate zone where the spectrum is modulated.

As an example Fig. 20 shows a calculated spectrum for a device with a relatively large K value but with a small angular acceptance. At sufficiently high photon energies the spectrum becomes smooth and the intensity equals $2N$ times that of a bending magnet - shown by the solid line in the figure.

In the absence of interference effects the radiation spectrum can be calculated as for a bending magnet but with a critical energy that varies with the angle of emission in the horizontal plane:

$$\varepsilon_c/\varepsilon_{co} = \sqrt{1-(\gamma\theta_x/K)^2}$$

The brightness can be approximated by the following expression [79]:

$$B = \frac{d\dot{n}/d\theta_x}{(2\pi)^{3/2}\left[\left(\sigma_x^2 + a^2 + \sigma_x'^2 L^2/12\right)\left(\sigma_y^2 + \sigma_y'^2 L^2/12\right)\left(\sigma_y'^2 + \sigma_R'^2\right)\right]^{1/2}}$$

where $d\dot{n}/d\theta_x$ is the total flux per unit horizontal angle, integrated over the vertical angle, and σ_R' is the vertical opening of the radiation, as for a bending magnet source; a is the amplitude of the sinusoidal motion ($=K\lambda_o/2\pi\gamma$). The above expression assumes that the magnet length is not too great ($L < 4\beta_x$, $L < 4\beta_y$), as well as a relatively small amplitude of motion ($a < \sigma_x$) and electron beam divergence ($\sigma_y' < \sigma_R'/2$), otherwise a summation must be made over every pole. The brightness of a wiggler is usually several orders of magnitude less than that of an undulator (see 5.2). To obtain significant flux the radiation is usually collected over a wide range of angles, which results in an increased effective source size which also needs to be considered in the beamline optics design. Further details of the geometrical properties of the radiation from multipole wiggler sources is given in Refs. [80,81].

4. INSERTION DEVICE TECHNOLOGY: INTRODUCTION

4.1 Electromagnets

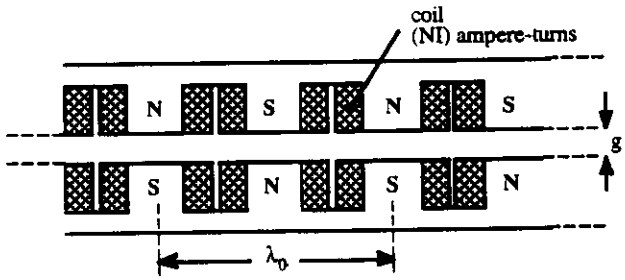

Fig. 21 Schematic of an electromagnetic undulator

To a first approximation an electromagnetic insertion device can be thought of as a series of dipole magnets. We can therefore estimate the field strength by applying Ampère's Law to a circuit as for a simple dipole magnet (see for example Ref. [82]):

$$\mu_o(NI) = B_o g/2$$

where (NI) is the number of Ampère-turns per coil. Using the definition of K this can be re-written as follows:

$$\frac{(NI)}{K} = \frac{4260}{(\lambda_o/g)} \qquad (21)$$

It can be seen therefore that in order to maintain a particular value of K, the number of Ampère-turns must increase rapidly as the ratio of period to gap decreases. There is a problem however to reach small period lengths even if the gap can be reduced correspondingly, since the space available for the coils decreases and hence the current density rapidly becomes too big for conventional (i.e. non superconducting) coils.

The above discussion assumed that the field is constant in the vertical direction, however this is not in general a good approximation since a sinusoidal field variation along the axis implies a variation of the field in the vertical direction in order to satisfy Maxwell's Equations. Using a 2D approximation i.e. no variation in the x-direction, the field can be written as follows:

$$B_y = \sum_{n=1}^{\infty} B_n \cosh(nky)\ \cos(nkz)$$

$$B_z = \sum_{n=1}^{\infty} B_n \sinh(nky)\ \sin(nkz)$$

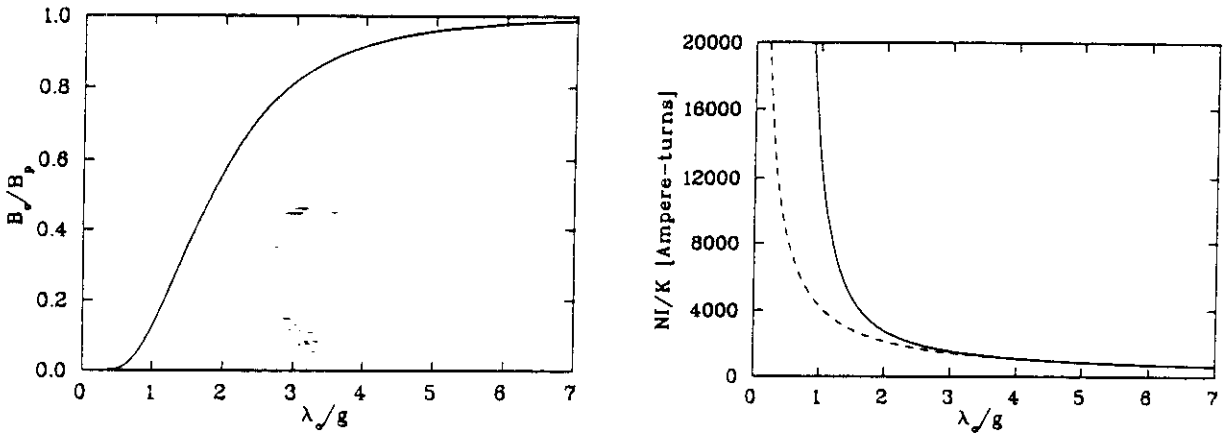

Fig. 22 Ratio of field on axis to the field at the pole-tip (left) and number of Ampère-turns required (right) as a function of period/gap ratio in an electromagnet

Assuming a geometry with pole lengths equal to one-quarter of a period length, and that the B_z field component at the height of the poles ($y = g/2$) is either zero at the poles or $\pm\ 8\mu_o(NI)/\lambda_o$ at the coils (from Ampère's Law) allows the coefficients B_n to be determined [83]. Comparisons with numerical calculations show that two terms in the series are sufficient to give accurate results and hence one obtains [84]:

$$B_y = \frac{32\mu_o(NI)}{\sqrt{2}\,\pi\lambda_o}\left[\frac{\cosh(ky)}{\sinh(kg/2)} - \frac{\cosh(3ky)}{3\sinh(3kg/2)}\right] \tag{22}$$

From this can be derived the following expression for the ratio between the field on-axis (B_o) and at the pole (B_p), shown in Fig. 22 (left):

$$\frac{B_o}{B_p} = \frac{1}{\cosh(kg/2)}\left[\frac{1-(\sinh(kg/2)/3\sinh(3kg/2))}{1-(\tanh(kg/2)/3\tanh(3kg/2))}\right]$$

The number of Ampère-turns required for a given K value can be expressed as follows:

$$\frac{NI}{K} = 1.18\ 10^3\ \sinh(kg/2)\left[1-\frac{\sinh(kg/2)}{3\sinh(3kg/2)}\right]^{-1}$$

which is shown in Fig. 22 (right) compared to the result for a simple dipole, Eq. (21).

In conclusion, it can be seen that for period-to-gap ratios greater than about 4 the magnet poles can be considered independent. At smaller values the field on-axis reduces and the excitation required increases significantly compared to the simple dipole model. As a rule-of-thumb a ratio $\lambda_o/g \geq 2$ is needed to obtain significant magnetic field on-axis, with not too high an excitation.

4.2 Permanent magnets

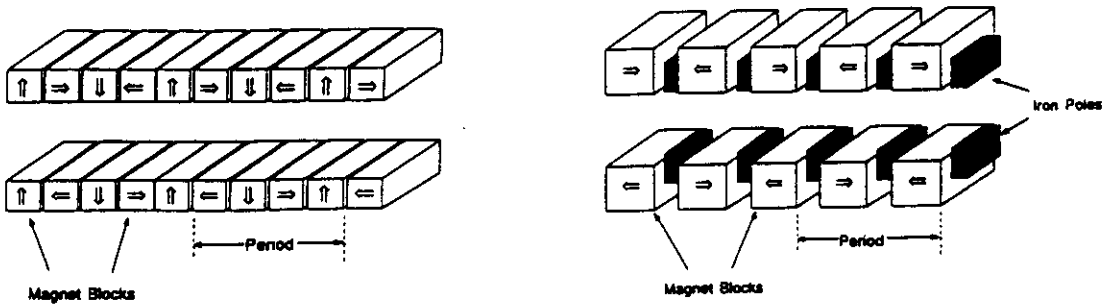

Fig. 23 Schematic diagrams of the "pure-permanent magnet" (left) and "hybrid" (right) types of insertion device

The use of permanent magnets for undulator and wiggler construction dates back to the very first undulator described by Motz in 1953 [3]. Permanent magnets were also employed in the ubitron developed by Phillips in the late 50's and early 60's [5]. Subsequently pioneering work on the development of permanent magnet undulators and their implementation in storage rings was carried out in the late 1970's and early 80's at INP, Novosibirsk (USSR) [16,85,86] and LBL, Berkeley (USA) [17,87,88]. The two schemes most commonly used are the "pure permanent magnet" and the "hybrid" schemes shown in Fig. 23.

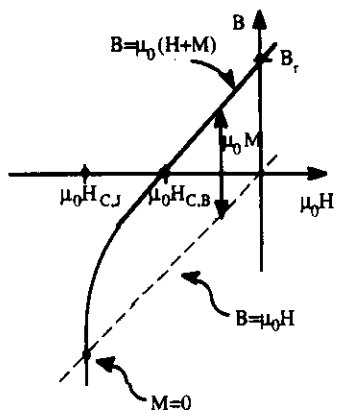

Fig. 24 De-magnetization curve of a permanent magnet

The two types of permanent magnet material in common use are samarium cobalt ($SmCo_5$ or Sm_2Co_{17}) and the more recently developed neodymium-iron-boron (NdFeB). The latter is the usual choice since it has a higher remanent field strength (1.1-1.3 T, compared to 0.9-1.0 T for SmCo) as well as a lower cost. The main disadvantages are that it has less radiation resistance and also a larger variation with temperature (0.11%$^oC^{-1}$ compared to 0.04% $^oC^{-1}$ for SmCo). Figure 24 shows a typical de-magnetization curve for such hard permanent magnet materials. Manufacturer's tables usually quote the following 3 quantities: the remanent field (B_r) where H=0, the coercive force ($\mu_0 H_{c,B}$) where the induction becomes zero and the intrinsic coercive force ($\mu_0 H_{c,J}$) where the magnetization becomes zero. A large value of $\mu_0 H_{c,J}$ is an advantage to avoid demagnetization of the pieces during assembly. If it necessary to take demagnetization effects into account, manufacturers can supply permanent magnet blocks that have been thermally and/or magnetically stabilized - heated to a higher temperature, or subjected to a higher reverse magnetic field than the blocks will experience during assembly or operation.

The slope of the curve in the linear region ($\mu=B/\mu_0 H$) is typically 1.05-1.06. The fact that this is close to unity has important consequences [87,89]. Unit permeability implies constant magnetization and so the equivalent charges $\rho = \nabla \bullet M$ and equivalent currents $J = \nabla \times M$ are zero except at the permanent magnet block surfaces. The material therefore behaves like vacuum

surrounded by charge or current sheets, hence the expression "charge (or current) sheet equivalent material" or CSEM. This fact means that the field from different pieces can be superimposed linearly. It also leads to a simple calculation of the fields in the case of simple geometries, in the absence of ferromagnetic material. It is interesting to note that the equivalent current is very large, 8 kA per cm of the block dimension for a 1 T remanent field, which explains why permanent magnets are so efficient in generating magnet field. Another advantage is the fact that, unlike electromagnets, the field remains the same if all of the dimensions are scaled. For the most part the small effects due to the non-unit permeability can be neglected. At the level of detail however, this is no longer true; some of the small effects that can arise due to non-linear superposition in pure permanent magnet systems are discussed in Ref. [90].

The field achievable in a 2D approximation from a pure permanent magnet geometry can be calculated analytically [87] and is given as follows:

$$B_o = 2B_r \frac{\sin(\pi/M)}{(\pi/M)}(1-e^{-2\pi h/\lambda_o})e^{-\pi g/\lambda_o} \tag{23}$$

where M is the number of blocks per period in each array, usually 4 as shown in Fig. 23, and h is the block height.

In the hybrid case the field cannot be calculated analytically. Instead the following type of empirical relationship is often used to estimate the achievable field amplitude, based on a series of 2D field calculations with optimized pole and magnet dimensions:

$$B_o = a\exp\left(-b\frac{g}{\lambda_o}+c\left(\frac{g}{\lambda_o}\right)^2\right) \tag{24}$$

In the above, the values appropriate to $SmCo_5$ material with $B_r = 0.9$ T have been found to be: $a = 3.33$, $b = 5.47$, $c = 1.8$ [88] whereas for NdFeB with $B_r = 1.1$ T the values are $a = 3.44$, $b = 5.08$, $c = 1.54$ [91]. The validity of the above expression is usually quoted as $.07 < g/\lambda_o < 0.7$, giving a peak field of 2.3 T ($SmCo_5$) or 2.4 T (NdFeB) for $g/\lambda_o = 0.07$. Sometimes the above expression is multiplied by a factor 0.95 to account for 3D effects, non-optimized dimensions etc.

4.3 Performance comparison

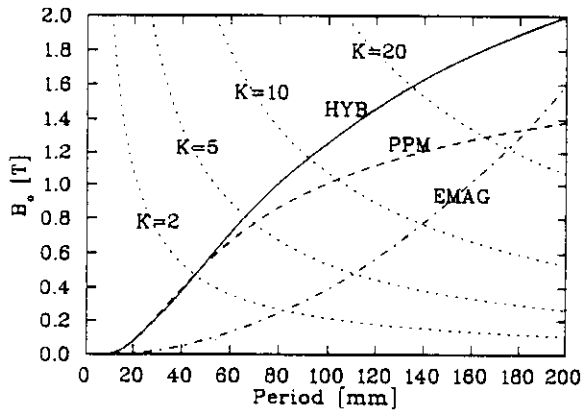

Fig. 25 Comparison of performance of electromagnetic (EMAG), pure permanent magnet (PPM) and hybrid (HYB) insertion devices
EMAG - Eq. (22) with rectangular coils of area $\lambda_o/8 \times \lambda_o/4$ with J=10 A/mm^2
PPM - Eq. (23) with $M = 4$, $h = \lambda_o/2$, $B_r = 1.2$T.
HYB - Eq. (24) with $a = 3.27$, $b = 5.08$, $c = 1.54$

Figure 25 compares the performance of electromagnet, pure permanent magnet (PPM) and hybrid designs, using the above formulae in the case of a 20 mm gap. The maximum field strength achievable is limited in the case of the electromagnet and hybrid designs by steel saturation, not included in the formulae, and in the case of the PPM by the remanent field of the material. It is clear that the electromagnet is only competitive in the case of long period lengths, or if a reduced field strength is acceptable. For fields in excess of about 0.6 T the hybrid design exceeds the PPM performance. However, in the undulator regime, $K \leq 5$, the performance of the PPM and hybrid types are very similar.

5. INSERTION DEVICE PERFORMANCE LIMITS AND PARAMETER OPTIMIZATION

5.1 Undulator performance limits

Following the previous general discussions of the properties of the radiation emission (Section 3) and the magnetic performance of various insertion device types (Section 4) we will now put these two together to examine what determines the practical performance limits and how the main parameters are chosen in a number of practical cases, based on the more usual choice of permanent magnet rather than electromagnet technology. To do this it will be sufficient to use simple formulae for the radiation flux, Eq. (18), and magnet performance, Eqs. (23) and (24), since they are generally sufficiently accurate to enable the main parameters to be determined on the basis of the required photon energy tuning range. In practise, the next stage would be to revise the parameters after carrying out a detailed magnet design.

We note first of all that optimization of the brightness and flux at a given photon energy are equivalent since the ratio between brightness and flux involves factors depending only on photon energy, electron beam emittance and undulator length which are fixed quantities. Given the magnet period and gap, we can therefore calculate the field amplitude using either Eq. (23) or (24), and hence K and the flux per unit length of undulator as follows:

$$\text{Flux[photons / s / 0.1\%bandwidth / m / A]} = 1.43\ 10^{14}\ \frac{F_n(K)(1+K^2/2)}{\lambda_o n}$$

The photon energy can also be expressed in terms of known quantities as follows:

$$\frac{\varepsilon}{E^2}[\text{eV/GeV}^2] = \frac{9.498\ n}{\lambda_o(1+K^2/2)}$$

We can therefore plot one quantity against another i.e. photon flux as a function of normalized photon energy, for different magnet periods and gaps. Figure 26 (left) shows the resulting curves of both fixed gap (variable period) and fixed period (variable gap), assuming in this case a pure permanent magnet geometry, Eq. (23) with Br = 1.2 T and $h = \lambda_o/2$. Figure 25 shows that in the present range there is little difference between the performance of the two permanent magnet configurations. From the dashed curves in Fig. 26 (left) (fixed gap) it is clear that at any photon energy the smallest gap always gives the highest flux, especially at the highest photon energies where flux is critically dependent on magnet gap. The solid curves (fixed period) show the tuning curves achievable in a practical case with fixed period length. It can be seen that longer periods give a wider tunability, because of the larger K value, whereas the short periods which are required to reach the highest photon energies result in much reduced tunability.

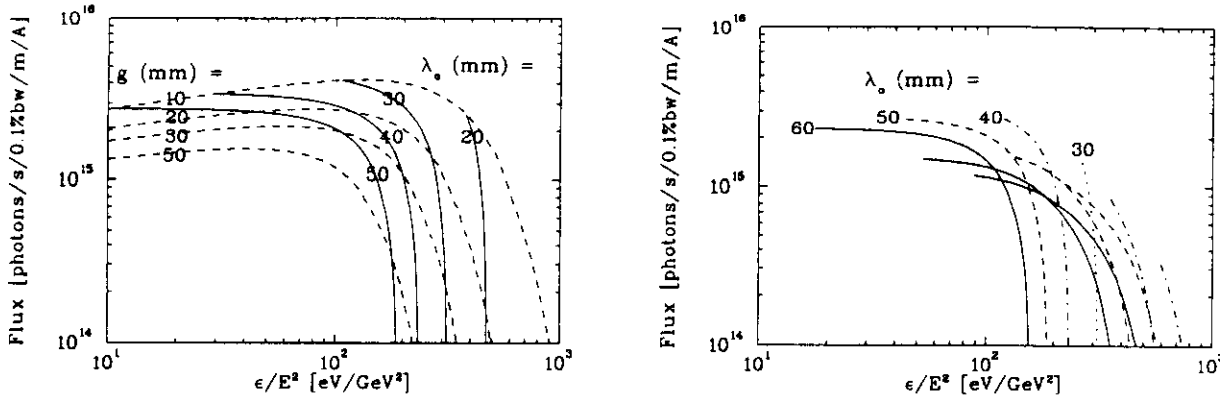

Fig. 26 Undulator flux as a function of normalized photon energy;
left - first harmonic as a function of gap and period
right - first, third and fifth harmonics as a function of period, gap = 20 mm

The results above refer only to the fundamental ($n = 1$) of the radiation. Higher harmonics can however be used in order to extend the tuning range. This is illustrated in Fig. 26 (right), where the tuning curves for the 1st, 3rd and 5th harmonics are shown for various period lengths, with a minimum gap of 20 mm. Longer periods and hence larger K values result in an overlap of the harmonics, allowing a wide tuning range to be covered. As the period and hence K value reduces so also does the overlap of the harmonics, eventually leaving a gap between them. For a "reasonable" overlap between the 1st and 3rd harmonics a K value ≥ 2.2 is required, which also guarantees overlap of the successive harmonics. If one is willing to give up some tunability in favour of reaching higher photon energies, a K value ≥ 1.3 is a reasonable choice, since it allows tuning through the 3rd, 5th and successive harmonics. Figure 26 illustrates the fact that there is an optimum range of photon energies that can be covered with a machine of a given energy, and with a given minimum gap. At low photon energies the limitation is the large K value and hence the high radiation power density, whereas at high photon energies the limitation is the rapidly reducing flux. Table 3 indicates what might be considered the optimum range of photon energies for 3 "standard" machine energies, 0.8 GeV (e.g. SuperACO), 2 GeV (e.g. ELETTRA) and 6 GeV (e.g. ESRF). It can be seen that although there is significant overlap between the ranges, the different machines are nevertheless optimized for different spectral regions, namely the VUV, Soft X-ray and X-ray ranges respectively.

Table 3
"Optimum" photon energy ranges as a function of
storage ring energy, based on a minimum undulator gap of 20 mm

Ring Energy (GeV)	Photon energy range
0.8	6 eV - 450 eV
2.0	40 eV - 2.8 keV
6.0	360 eV - 25 keV

It should be emphasized that the "optimum" photon energy ranges shown in the Table are only indicative. For example, as we have already seen, the performance is strongly determined by the minimum gap that can be allowed. Special insertion devices can also be built with even smaller gaps to extend the performance at higher energy. The lower photon energy limit is also rather arbitrary, and depends in practise on the acceptable power loading. Overall however it remains true that undulator performance is one of the most important factors determining the choice of energy for a synchrotron radiation facility, and that this is essentially limited (at the high photon energy limit) by the minimum gap that can be allowed for successful machine operation.

5.2 Undulator parameter optimization

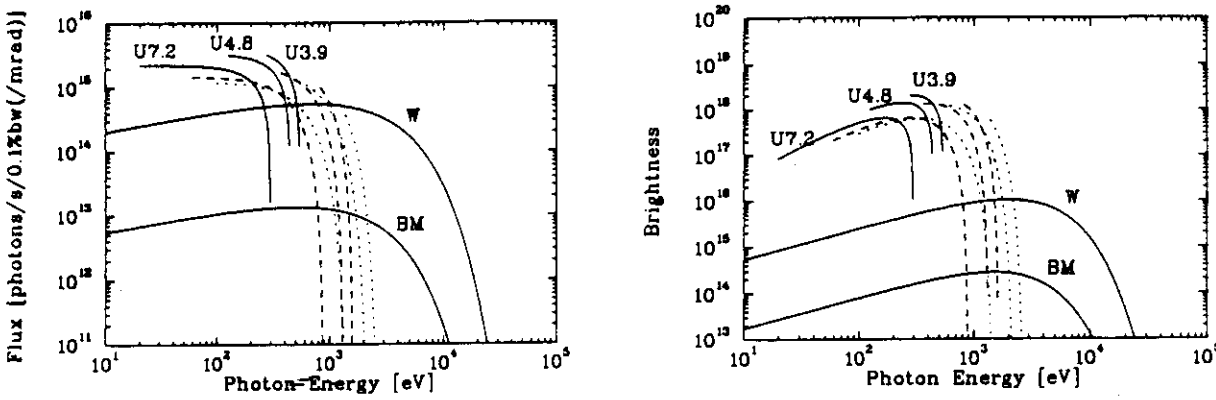

Fig. 27 Flux (left) and brightness (right) for various sources in a 1.5 GeV ring: U - 1st (solid), 3rd (dashed) and 5th (dotted) harmonics; W - multipole wiggler; BM - bending magnet. (E=1.5 GeV, I_b = 0.4 A, ε_x=10^{-8} m rad, ε_y = 10^{-9} m rad, β_x = 5 m, β_y = 2 m, ID length = 3 m, BM field = 1.2 T)

Table 4

Parameters of various undulators shown in Fig. 27; peak power density units W/mrad^2

λ_o(mm)	g (mm)	B_o(T)	K	$P_{tot.}(W)$	$d^2P/d\Omega$
39	20	0.38	1.40	247	615
26	10	0.57	1.40	554	1381
18.5	5	0.81	1.40	1120	2787
48	20	0.51	2.29	443	686
72	20	0.78	5.26	1029	702
100	≥ 20	0.47	4.40	379	309
150	≥ 20	0.25	3.50	107	109
200	≥ 20	0.11	2.56	21	29

As a practical example we will consider the design of undulators for a 1.5 GeV ring based on a minimum gap of 20 mm; the principles involved however remain valid for any other choice of parameters. Figure 27 shows the flux and brightness achievable from a range of different undulators, together with that from a multipole wiggler and a bending magnet for comparison. In the latter cases the flux is integrated vertically, and per mrad of horizontal angle. Although the multipole wiggler can provide a reasonably high flux, clearly the brightness is several orders of magnitude inferior to that of an undulator. The parameters of the devices are given in Table 4 which includes also the total power and peak power density of the radiation.

As stated in the Section above, at the low photon energy end of the spectrum the radiation power density can become a limiting factor. Figure 28 (a) shows a selection of different devices all with a fundamental of 20 eV. As the period length increases the power and power density decrease rapidly, as shown in Table 4, whereas the flux decreases more slowly. The choice therefore is a compromise between power, flux and tuning range.

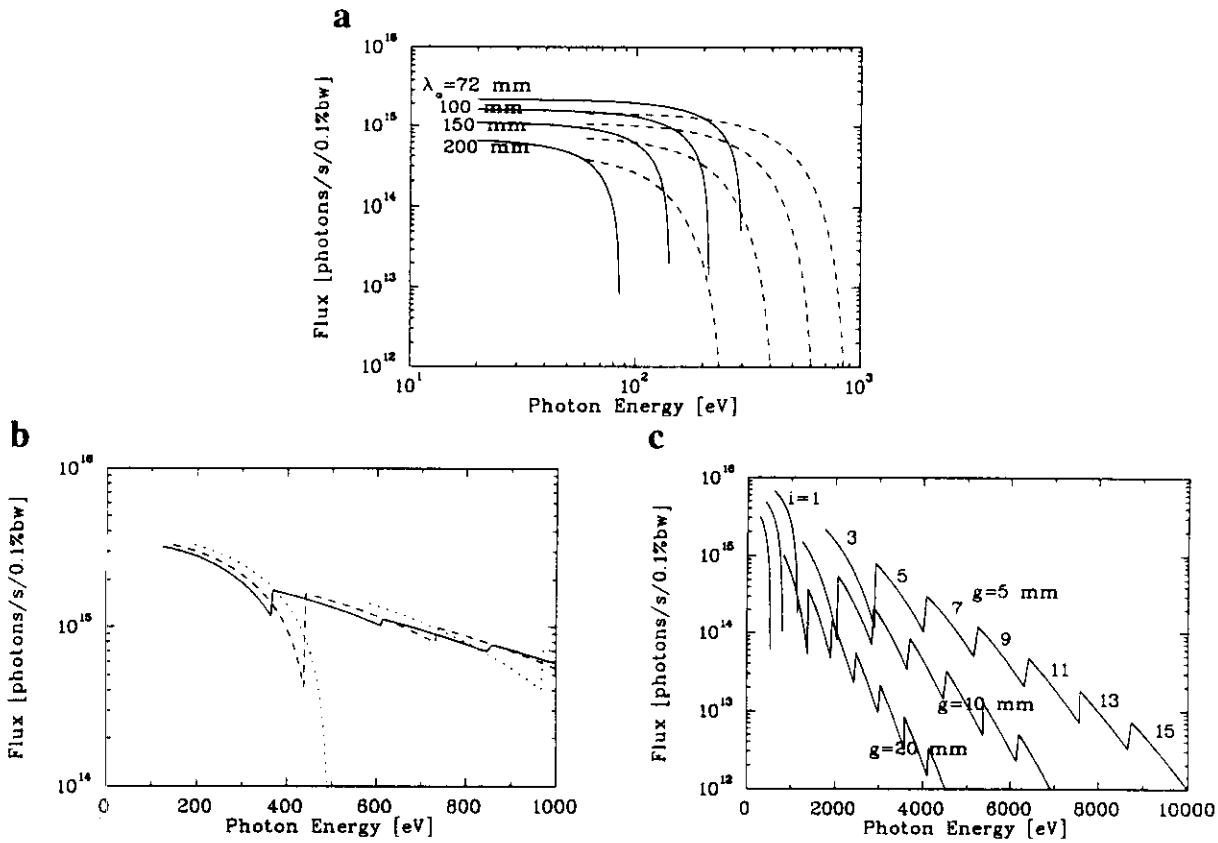

Fig. 28 Undulator performance in low, medium and high energy spectral regions. (a) λ_o = 72 - 200 mm; (b) λ_o = 43 mm (dotted), 46 mm (dashed) and 48 mm (solid); (c) undulators optimized for gaps of 5 mm (λ_o = 18.5 mm), 10 mm (λ_o = 26.2 mm) and 20 mm (λ_o = 39.2 mm). Ring parameters as Fig. 27.

In the medium and high energy parts of the spectrum the choice of undulator parameters is often dictated by the required tuning range rather than simply the energy of the fundamental. For example, Fig. 28 (b) shows the performance for 3 undulators with similar period lengths in the range 43-48 mm. The device which gives the peak flux at 200 eV for example has a period of 43 mm, however in this case the K value is too small (1.8) to allow a continuous coverage between the fundamental and 3rd harmonic at 600 eV. A slightly larger period length of 46 mm (K=2.1) or 48 mm (K=2.3) results in only a small reduction in flux at 200 eV but provides a much wider tuning range.

At the high energy extreme the performance reduces rapidly, even if higher harmonics are used, as shown in Fig. 28 (c). A lower gap is clearly advantageous in this case, and the figure shows the result for a 5 mm and 10 mm gap. In each case the period has been adjusted to maintain a K value of 1.4 which allows tunability from the 3rd harmonic upwards. Table 4 gives the parameters for these devices.

6. INSERTION DEVICE TECHNOLOGY: DETAILED MAGNETIC DESIGN

6.1 Detailed magnetic design: periodic part

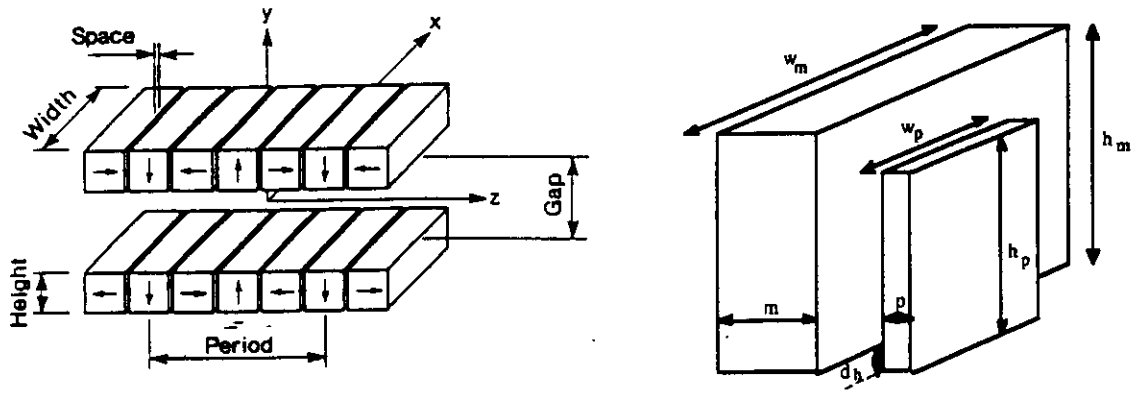

Fig. 29 Parameters to be optimized for pure-permanent magnet (left) and hybrid (right) structures

Having first established the main parameters of the device on the basis of the required characteristics of the radiation (Section 5) the next step in the design process is generally to carry out the detailed design, which usually starts with the periodic part of the structure. In the case of the pure permanent magnet case 3D analytic formulae exist for the field due to a parallelepiped block in the approximation of unit permeability, which is generally a sufficiently good approximation. Adding the field from a sufficient number of blocks then allows the field in the centre of the device to be calculated. Many laboratories have codes which will perform these calculations, e.g. Ref. [92].

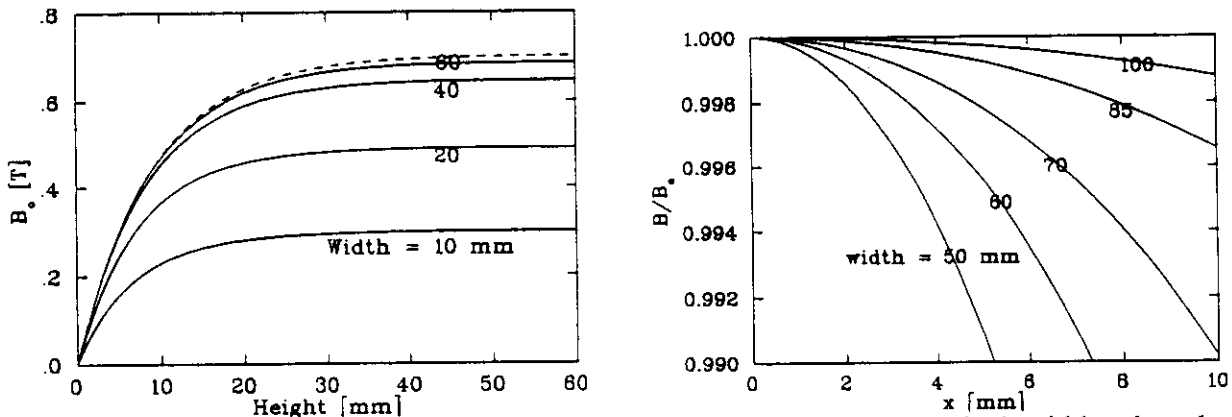

Fig. 30 Left - variation of field amplitude with block height for various block widths; dotted line - infinite width. Right - relative field variation with transverse position for various block widths (block height = 28 mm). Period = 56 mm, gap = 20 mm, space = 0, Br = 1.2 T

Using such a program it is then a relatively simple matter to optimize the remaining parameters, namely the magnet height and width, see Fig. 29. The space between the blocks is usually sufficiently small to have a negligible effect. Fig. 30 (left) shows the variation of field amplitude with block height for various block widths in one particular case. To reach sufficiently close to the maximum achievable value a height of 26 mm i.e. $h = \lambda_o/2$ was chosen. A width of 85 mm was chosen, not because of the field strength - for which a width of about 40 mm would be sufficient - but in order to give a satisfactory field homogeneity. The transverse field variation is shown in Fig. 30 (right).

In the case of the hybrid design the situation is more complicated since there are more parameters to optimize, as shown in Fig. 29, and more criteria to satisfy: achieving the required field and field homogeneity with a minimum volume of permanent magnet material, whilst avoiding excessive saturation in the iron and regions of reverse field in the permanent magnet

material. Some account has to be taken of three dimensional effects. A possible solution is therefore to use a 3D code; several commercial ones are available such as AMPERES, FLUX3D, MAFIA, MAXWELL and OPERA-3D. Such codes are however generally quite expensive and require a period of training before reliable results can be obtained. An alternative is to use a combination of a 2D code, which includes the effect of saturation in the iron, and 3D approximations valid for infinite μ [93,94].

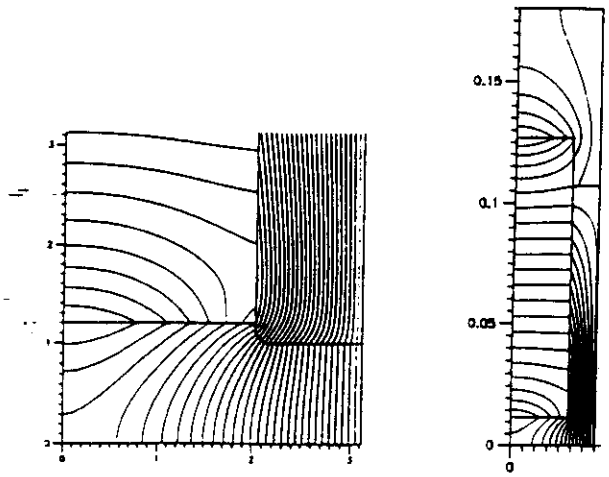

Fig. 31 Magnetic flux lines in a hybrid device; right - complete model of 1/8th period, left - detail of the pole-tip region

By making use of symmetry only 1/8th of a complete period needs to be modelled; Figure 31 shows part of the field distribution in one case, together with the detailed region near the pole surface. A choice that has to be made is to use standard magnet steel, with a saturation magnetization of about 2.1 T, or iron-cobalt steel which has a significantly higher saturation of about 2.4 T. The latter is more costly but can lead to a smaller pole width and a reduction in the volume of permanent magnet material and hence can be cost effective. In the hybrid design it is important that the permanent magnet is larger than the pole in order to reduce flux leakage [95].

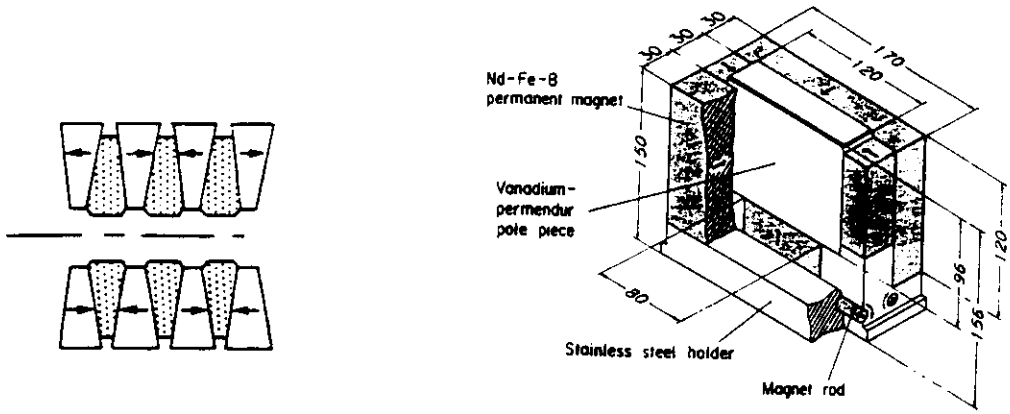

Fig. 32 Alternative hybrid designs; left - with wedged poles, right - with side magnets

Alternative geometries to the basic one discussed above that can lead to an enhanced field strength, but with an increase in complexity and cost, are the wedged-pole geometry [96], and the inclusion of side-magnets [97], as shown in Fig. 32.

A factor that has to be taken into account particularly in the hybrid design is the fact that the field can vary significantly from a pure sinusoid, containing a large 3rd harmonic component. The effect is to change the fundamental photon energy, and also the radiation opening angle.

6.2 Detailed magnetic design: ends

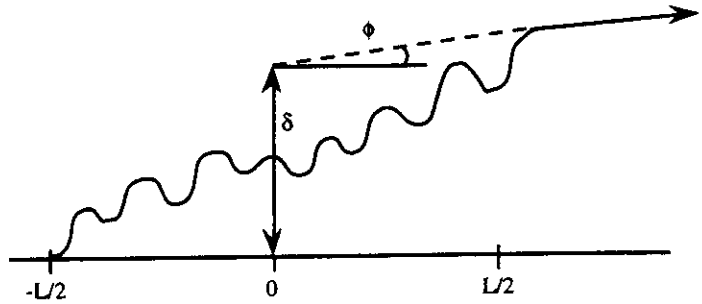

Fig. 33 Projection of electron beam exit conditions to the centre of the insertion device

In order that the insertion device does not affect the storage ring closed orbit requires that there is no net change in transverse position or angle of the beam. In the horizontal plane for example the final angle and position at the end of the device ($z = L/2$) are given as follows:

$$x'(L/2) = \frac{e}{\gamma mc} \int_{-\infty}^{L/2} B_y(z)\, dz = \phi$$

$$x(L/2) = \frac{e}{\gamma mc} \int_{-\infty}^{L/2} dz \int_{-\infty}^{z} B_y(z')\, dz'$$

which are often referred to as the first and second field integrals respectively. It is convenient to refer to the position of the beam projected back to the centre of the device (δ) , rather than at the end, as shown in Fig. 33. After integrating the second expression by parts and re-arranging one obtains the following result:

$$\delta = x(L/2) - x'(L/2)\frac{L}{2} = -\frac{e}{\gamma mc} \int_{-\infty}^{L/2} B_y(z)\, z\, dz$$

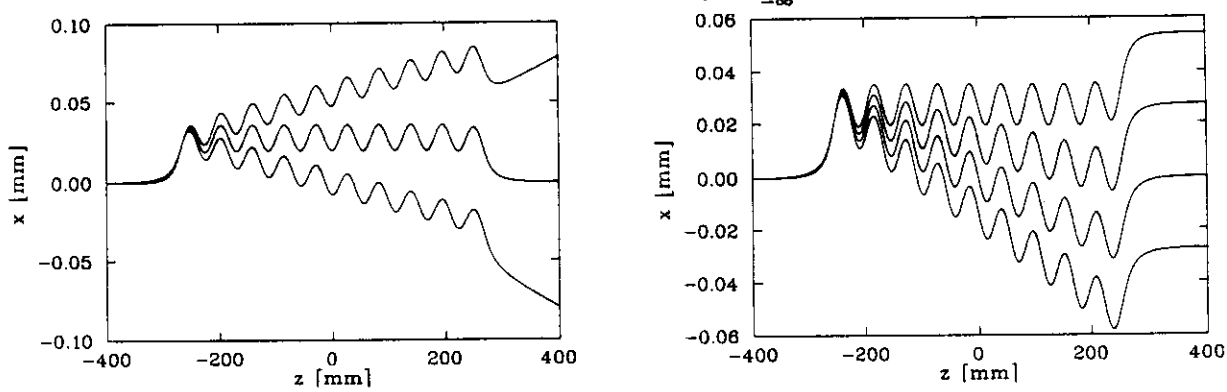

Fig. 34 Electron trajectories in insertion devices with symmetric (left) or anti-symmetric (right) field distributions

We can now examine the requirement for no net change in angle (ϕ) or position (δ) of the beam. In the usual case the magnet design is symmetric with respect to the centre of the device. According to the above equation we have then by symmetry $\delta = 0$. The correct angular condition $\phi = 0$ is obtained by appropriate adjustment of the end-poles as illustrated in Fig. 34 (left). An alternative configuration is anti-symmetric with respect to the centre. In this case by symmetry $\phi = 0$, and the condition $\delta = 0$ is obtained by correct adjustment of the end-poles, as illustrated in Fig. 34 (right). In the case that the magnet consists of a series of equal strength central poles with a special end-pole at either end, then the required condition can be met in the

case of the symmetric configuration by arranging that the end-poles have one half of the field integral of the centre poles. In the anti-symmetric case however no such simple result exists; the relative strength required for the end-poles depends on the number of poles in the magnet (M) as follows: $(M-\frac{1}{2})/(M-1)$.

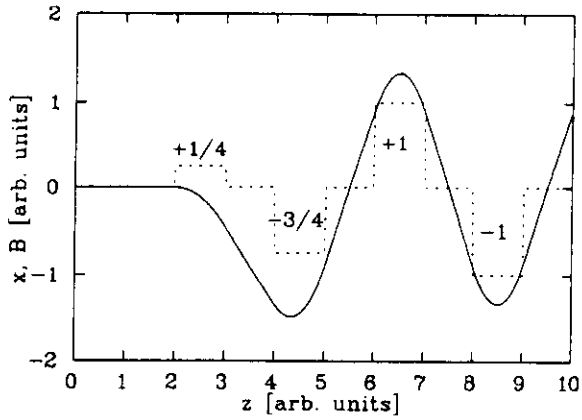

Fig. 35 Sequence of magnet poles (dotted line) resulting in no offset between the electron trajectory (solid line) and the magnet axis.

It can be seen from Fig. 34 that even when the magnet is perfectly compensated in angle and position the axis about which the electron beam oscillates is offset from the straight through direction either in position (symmetric case) or angle (anti-symmetric case). Such an offset is not generally a problem, but can be in certain applications. To overcome this requires a more sophisticated entrance and exit configuration involving more than one end-pole. Considering an arrangement of equally spaced poles, the simplest arrangement employs two reduced-strength end-poles with a sequence of 1/4, -3/4, 1 ... as shown in fig 35. It is clear that the same configuration can be applied to either the symmetric or anti-symmetric cases. For sequences involving three end-poles a variety of solutions are possible, which can be expressed as follows: x, -(2x + 1/4), (x + 3/4), -1.

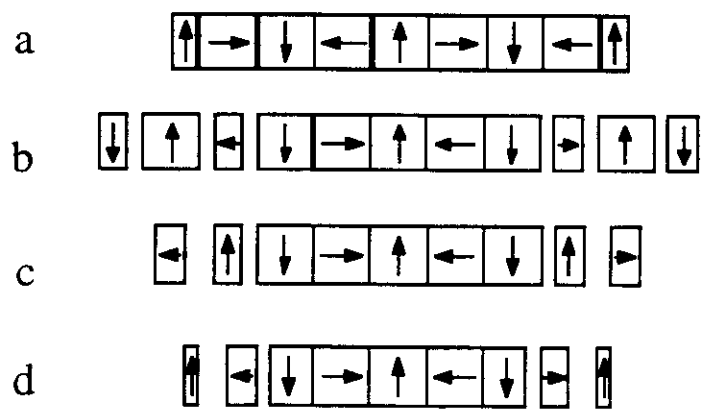

Fig. 36 Various end-sequences for the pure-permanent magnet structure

Implementation of the various end-pole sequences described above is straightforward in the case of the pure permanent magnet configuration because of the applicability of linear superposition. As a consequence of this, the field integral due to a single block depends linearly on the block length. A great advantage is the fact that apart from small effects due to non-unit permeability and magnetization errors the device remains compensated at all gaps. In the symmetric case overall compensation can be achieved simply by terminating with a half-block, as shown in the Fig. 36 (a). Some other schemes are shown (b-e) that give no offset of the oscillation axis using either half-sized blocks (b, c) or 1/4 and 3/4 sized blocks (d) [98].

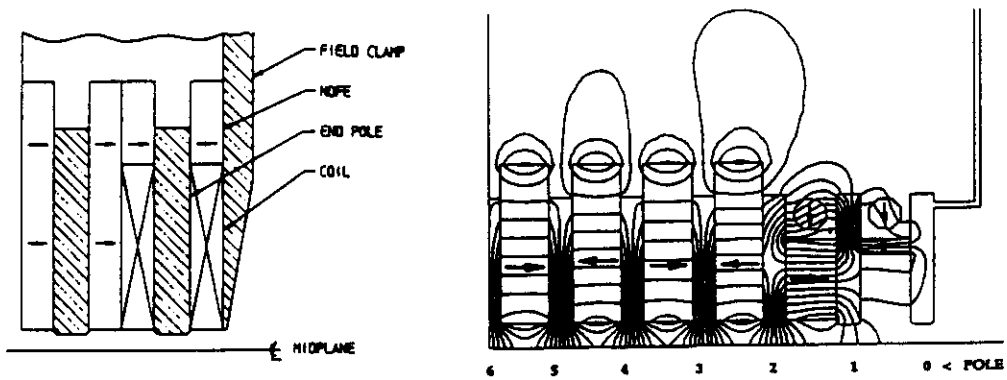

Fig. 37 Termination schemes for hybrid insertion devices using coils (left) and rotating magnets (right)

In the case of the hybrid construction no simple geometrical arrangement exists for the termination. Even after adjusting permanent magnet or pole dimensions to achieve compensation there still generally exists a significant variation of the field integrals with gap that needs to be overcome with an active system such as a coil [99] or rotating permanent magnet block [100], as shown in Fig. 37. Recently, there has been some success in developing a geometry that reduces the variation of field integral with gap, with the hope of eliminating completely the correction system. In one case empirical adjustments were made to the strength of the end magnets and the height of the next to last pole [101]. In another case 3D computer runs were made to optimize the end geometry [102]. Interestingly, in both cases the resulting solution produces close to no offset between the magnet and the oscillation axes.

6.3 Magnetic field errors

Magnetic field errors arise due to variations in the dimensions and shape of the magnets and poles, variations in gap etc., as well as variations in magnetization strength and angle from block to block and inhomogeneity. The effects of such errors are two-fold: unwanted effects on the electron beam and deterioration of the quality of the emitted radiation. In the former case, the effects are due to the non-zero first and second field integrals along the beam axis, which produces a change in the closed orbit, as well as the transverse variation of these quantities. The transverse variation of the first field integral errors can be expressed in terms of multipole components which cause changes in focusing properties, i.e. changes in tune values and betatron functions (quadrupole errors), variations in coupling (skew-quadrupole errors) as well as non-linear beam dynamics effects (sextupole, octupole errors etc.). Effects on the radiation spectrum on the other hand depend on the details of the field distribution and hence electron trajectory. Effects arise due to both the deflection of the electron beam away from the nominal axis, as well as errors in the phase of the radiation. The latter cause a loss of constructive interference causing reduced angular flux density and brightness, particularly on the higher harmonics.

Initial work on the effects of field errors on the emitted radiation [103] attempted to characterize the effect in terms of the variation in field amplitude from pole to pole, which was assumed to be a random quantity. It was shown later however that the intensity is not well correlated with this quantity [104], but is well correlated to the radiation phase error [105]. The phase can be calculated simply from the magnetic field distribution as follows:

$$\phi = \frac{2\pi}{\lambda}\left(\frac{z}{2\gamma^2} + \int \frac{x'^2}{2} dz\right)$$

where the angle x' is given by Eq. (2). In practise the phase is calculated at each magnet pole and the linear variation subtracted, to remove the π increase in phase between each pole and also to take account of any small changes in the radiation wavelength from the nominal value [64,

106]. The rms value of the phase variation (σ_ϕ) is then calculated. Simulations show that the relative intensity of the n'th harmonic (R_n) agrees well with the simple formula [64]:

$$R_n = \exp(-n^2\sigma_\phi^2)$$

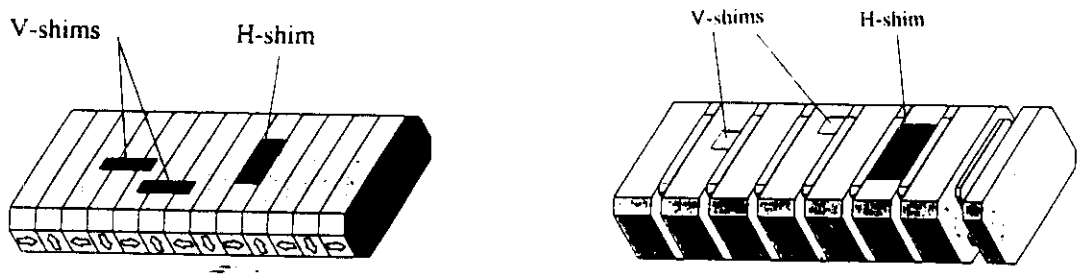

Fig. 38 Method of magnetic shimming to improve the magnetic field quality

In order to combat field errors therefore requires a sufficiently precise mechanical construction as well as some method for overcoming the effect of magnetization errors. For the latter various techniques have been adopted. The first consists of measuring the individual permanent magnet blocks and then arranging them in the structure in such a way as to optimize the field quality. Sorting procedures of this kind are most widely applied to the pure permanent magnet case where linear superposition can be used. Various ways of characterizing the blocks have been tried based on measurement of either total magnetization strength, field integrals or field maps. The most common sorting procedure is based on the "simulated annealing" algorithm [107] although "genetic algorithms" have also been used [108]. Once the magnet has been constructed and measured, the remaining errors can be overcome by swapping blocks, or more commonly by "shimming" i.e. placing thin ferromagnetic sheets on the magnet surfaces (see Fig. 38). Shimming was first applied to hybrid devices to correct pole-to-pole field strength error [109] and subsequently as a means of correcting multipole errors [110,111] and then also radiation phase errors [112-116]. As a result of these developments, as well as better magnetic measurement techniques [117], recent insertion devices have been free from the multipole errors observed in some earlier devices and have also far exceeded expectations in terms of the radiation performance. When the present "third generation" of synchrotron radiation sources were planned it was thought that field errors would preclude use of harmonics higher than about the 5'th. Now, with the correction techniques described above, the undulator spectrum can be almost perfect up to much higher harmonic numbers so that the limiting factor is no longer the undulator quality but that of the electron beam itself (emittance and energy spread).

7. INSERTION DEVICES FOR CIRCULARLY POLARIZED RADIATION

7.1 Introduction

There is an increasing interest in using circularly polarized radiation over a broad photon energy range for a wide range of experiments such as Circular Dichroism (CD) - which measures the difference in absorption between right- and left-handed polarized light, Magnetic Circular Dichroism (MCD) - the difference in absorption depending on the relative alignment of the magnetic field and the polarization directions in magnetic materials, and Circular Intensity Differential Scattering (CIDS) - the difference in scattering of right- and left-handed polarized radiation. Conventional insertion devices produce only linearly polarized radiation and so special types have been developed to generate circularly, or in general elliptically, polarized radiation. In this section we first introduce the concept and a basic description of the polarization, before considering the polarization properties of insertion devices.

The polarization of a radiation beam is determined by the phase relationship between the components of the Electric field [118]. For example given the horizontal component

$E_x = E_{xo}\cos(\omega t)$ and the vertical component $E_y = E_{yo}\cos(\omega t + \phi)$, it can be seen that there are in general three independent parameters, E_{xo}, E_{yo}, and ϕ. When $\phi = 0$ the radiation is linearly polarized, in a direction defined by the amplitudes E_{xo} and E_{yo}; when $\phi = 90^o$ and $E_x = E_y$ we have circularly polarized radiation. Such a description is not however of much practical use since none of these parameters are directly measurable, and in general we have to consider a superposition of different waves, not just a single monochromatic wave. A more useful description in terms of directly measurable quantities was introduced by G.G. Stokes in 1852, involving the following parameters:

$$S_0 = I_x + I_y = I_{45^o} + I_{-45^o} = I_R + I_L$$
$$S_1 = I_x - I_y$$
$$S_2 = I_{45^o} - I_{-45^o}$$
$$S_3 = I_R - I_L$$

S_1 is the difference in intensity transmitted by a linearly polarized filter oriented in the horizontal (x) and vertical (y) directions, S_2 is the difference in intensity for the components polarized at $\pm 45^o$ with respect to the x-y axes and S_3 is the difference in intensity of right- and left-handed circularly polarized components. The total intensity is S_0. Since only three independent parameters are needed it follows that there is some relationship between the above, and this is:

$$S_0^2 = S_1^2 + S_2^2 + S_3^2$$

The above description is true for a single monochromatic wave. In general there is a summation of waves from different source points in the insertion device as well as due to the range of wavelengths, the angular acceptance and the effect of electron beam emittance and energy spread. The effect of the summation is that the radiation can be divided into a polarized and an un-polarized part. For the polarized part the same decomposition into the three polarization states can be made, and so it follows that:

$$S_0 = \sqrt{S_1^2 + S_2^2 + S_3^2} + S_4$$

where S_4 is the intensity of the unpolarized radiation. Dividing through by the total intensity we obtain:

$$1 = \sqrt{P_1^2 + P_2^2 + P_3^2} + P_4$$

where $P_1 = S_1/S_0$ etc. The overall degree, or fraction, of polarization is therefore $\sqrt{P_1^2 + P_2^2 + P_3^2}$ and the fraction of unpolarized radiation is P_4. The quantities P_1, P_2 and P_3 are known as the polarization rates for the particular component.

The intensity of the radiation at a given frequency that is polarized in a given direction $\underline{u}$ is calculated by modifying Eq. (8) as follows:

$$\frac{d^2I}{d\omega\, d\Omega} = \frac{c}{4\pi^2}\left|\int_{-\infty}^{\infty} R\,(\underline{E}\cdot\underline{u})\, e^{i\omega t}\, dt\right|^2 = |\underline{A}\cdot\underline{u}|^2 \qquad (25)$$

The directions corresponding to the various polarization states are given below:

Polarization component	Direction vector, $\underline{u}$	Radiation amplitude
linear, x-direction	(1,0,0)	A_x
linear, y-direction	(-1,0,0)	A_y
linear, 45° to x-y	$(1,1,0)/\sqrt{2}$	$(A_x + A_y)\sqrt{2}$
linear, -45° to x-y	$(1,-1,0)/\sqrt{2}$	$(A_x - A_y)\sqrt{2}$
right circular	$(1,i,0)/\sqrt{2}$	$(A_x + iA_y)\sqrt{2}$
left circular	$(1,-i,0)/\sqrt{2}$	$(A_x - iA_y)\sqrt{2}$

In the above we also show the amplitude of the radiation polarized in the given direction in terms of the horizontal and vertical components, which are in general complex quantities. The intensities can then be expressed as follows:

$$I_x = |A_x^2| \qquad I_y = |A_y^2|$$

$$I_{45^o} = \left[|A_x^2| + |A_y^2| + A_x A_y^* + A_x^* A_y\right]/2 \qquad I_{-45^o} = \left[|A_x^2| + |A_y^2| - A_x A_y^* - A_x^* A_y\right]/2$$

$$I_R = \left[|A_x^2| + |A_y^2| - i(A_x A_y^* - A_x^* A_y)\right]/2 \qquad I_L = \left[|A_x^2| + |A_y^2| + i(A_x A_y^* - A_x^* A_y\right]/2$$

Finally, we can express the Stokes parameters in terms of the radiation amplitudes as follows:

$$\begin{aligned} S_0 &= A_x A_x^* + A_y A_y^* \\ S_1 &= A_x A_x^* - A_y A_y^* \\ S_2 &= A_x^* A_y + A_x A_y^* \\ S_3 &= i(A_x^* A_y - A_x A_y^*) \end{aligned} \tag{26}$$

7.2 Bending magnet and conventional insertion devices

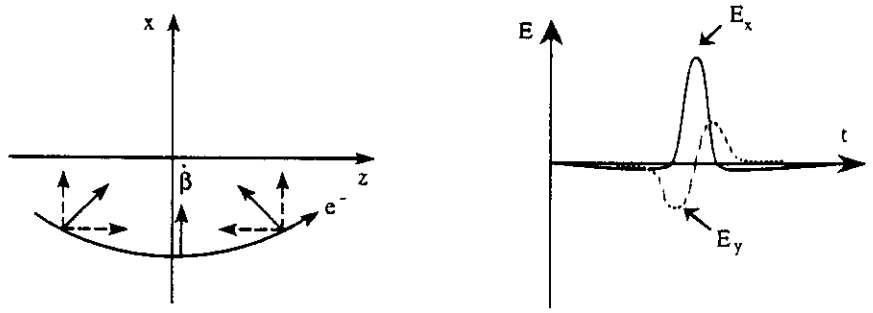

Fig. 39 Schematic diagram of radiation emission in a bending magnet: direction of electron acceleration (left), and electric field components as a function of time (right)

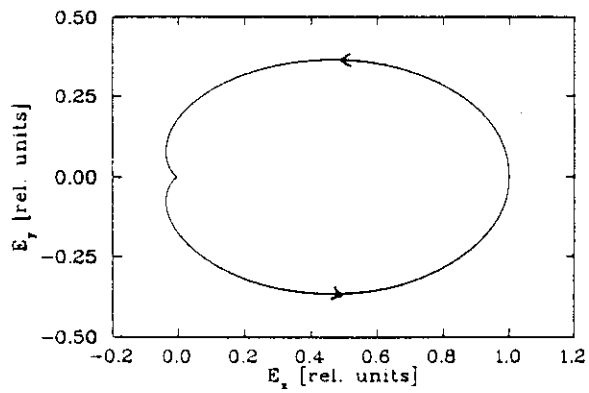

Fig. 40 Calculated electric field components, normalized to $(E_x)_{max.}$, for a bending magnet source with B= 1 T at a vertical angle $\gamma\theta_y$ = 1; arrows indicate the direction of rotation

In order to understand the polarization properties of bending magnet and insertion device sources we will examine the electric field of the radiation, which according to Eq. (9) is proportional to the electron acceleration. To a first approximation we have the following relationships:

$$E_x \sim \dot{\beta}_x - \theta_x \dot{\beta}_z$$
$$E_y \sim \dot{\beta}_y - \theta_y \dot{\beta}_z \tag{27}$$

where θ_x, θ_y are the angles of emission with respect to the x, y axes (Fig. 6). In a bending magnet which bends in the horizontal plane $\beta_y = 0$ and hence the vertical electric field component only exists for emission out of the orbit plane $\theta_y \neq 0$. It follows directly from the direction of acceleration that $E_x (\sim \beta_x)$ is symmetric with respect to the tangent point whereas E_y $(\sim \theta_y \beta_z)$ is anti-symmetric, as shown schematically in Fig. 39. Figure 40 shows the pattern traced out by the electric field for the particular case $\theta_y = 1/\gamma$. The circular motion of the electric field vector indicates the presence of circularly polarized radiation. In fact as the angle θ_y increases the fraction of circular polarization rate increases while the linear polarization decreases, as shown in Fig. 41. For angles below the orbit plane ($\theta_y < 0$) the vertical electric field component changes sign and hence the direction of circular polarization reverses.

In terms of the radiation amplitudes, the symmetry of the electric field components implies that A_x is real whereas A_y is imaginary, which implies directly from Eqs. (26) that $S_2 = 0$. The Stokes parameters can therefore be written in this case as follows:

$$S_1 = I_x - I_y$$
$$S_2 = 0$$
$$S_3 = \pm 2\sqrt{I_x I_y}$$

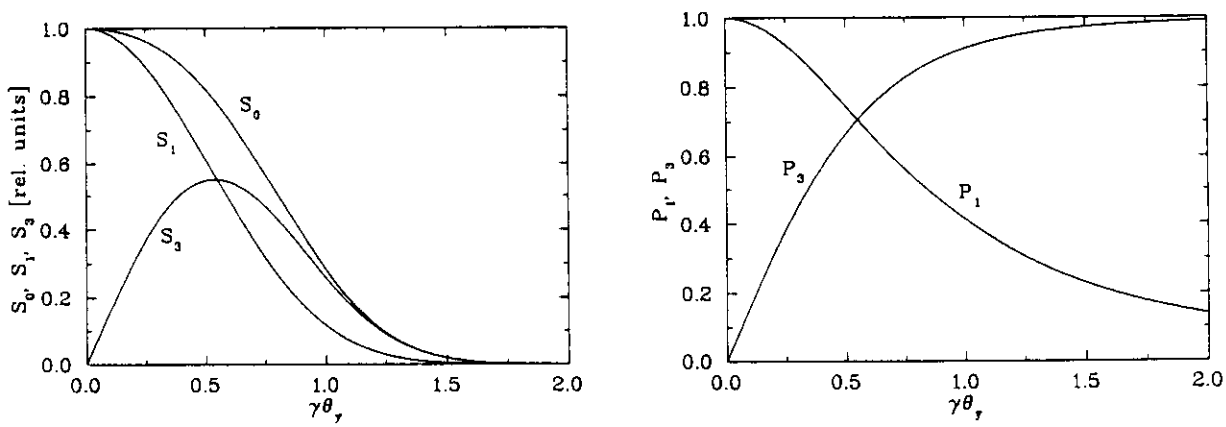

Fig. 41 Stokes parameters (left) and relative polarization rates (right) as a function of vertical angle for bending magnet radiation, at a wavelength corresponding to the critical wavelength ($\lambda = \lambda_c$)

We now consider what happens in the case of a conventional insertion device. Figure 42 shows one period of such a device and it can be seen that at the second pole β_x and hence E_x changes sign, whereas β_z and hence E_y remain the same, as indicated schematically. Figure 43 also shows the calculated electric field variation for a particular case and it can be seen that the direction of rotation reverses, indicating a cancellation of the circularly polarized component. In other words, S_3 has the opposite sign for the second pole compared to the first; summing the intensities of the two poles then results in $S_3 = 0$. All radiation that is not linearly polarized is therefore unpolarized (Fig. 44).

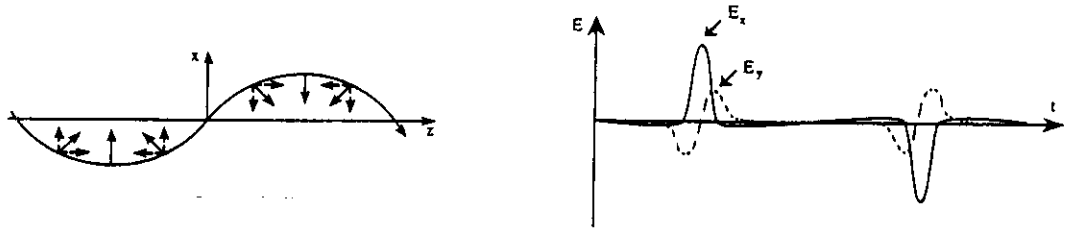

Fig. 42 Schematic diagram of radiation emission in an insertion device: direction of electron acceleration (left), and electric field components as a function of time (right)

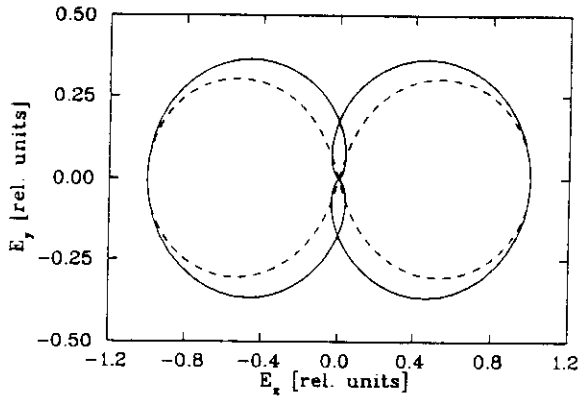

Fig. 43 As Fig. 40 for an insertion device; dashed line $K = 1$, solid line $K = 10$, $\lambda_o = 0.1$ m

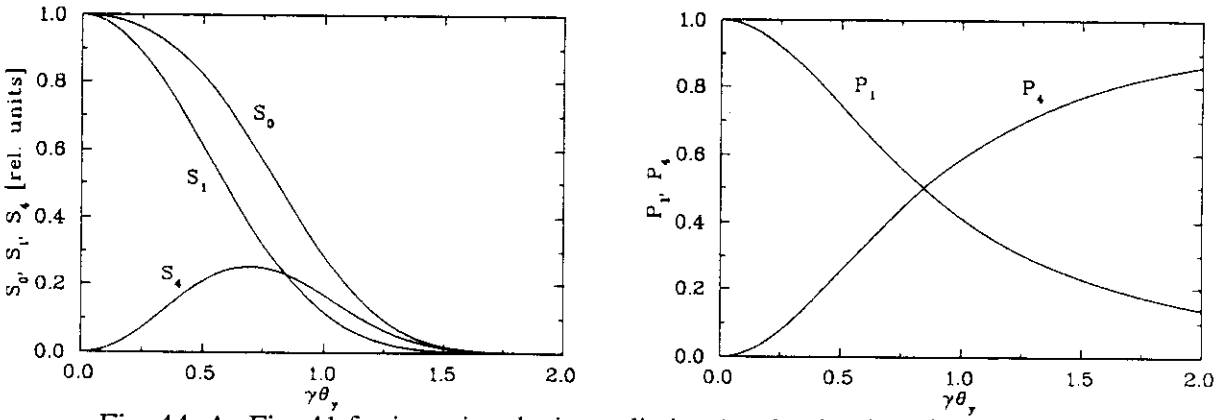

Fig. 44 As Fig. 41 for insertion device radiation (neglecting interference effects)

In the analysis above we have simply summed the radiation intensities from the positive and negative poles, neglecting the effect of interference, a procedure that is valid only in the limit of large K and large harmonic number (i.e. the wiggler case). To include the effect of interference we must examine the radiation amplitudes. Defining $t = 0$ at the centre of the two poles, we can write the amplitude as follows:

$$\int \underline{E}\, e^{i\omega t}\, dt = e^{-i\omega\Delta t} \underbrace{\int \underline{E}\, e^{i\omega t}\, dt}_{\text{1'st. pole}} + e^{i\omega\Delta t} \underbrace{\int \underline{E}\, e^{i\omega t}\, dt}_{\text{2'nd. pole}}$$

where $2\Delta t$ is the (observer) time difference between the first and second poles. Taking now the x- and y-components, recalling the sign change for the E_x component, we obtain:

$$A_x = A_{xo}(e^{-i\phi} - e^{i\phi}) = -2i\, A_{xo} \sin\phi$$

$$A_y = iA_{yo}(e^{-i\phi} + e^{i\phi}) = 2i\, A_{yo} \cos\phi$$

where A_{xo}, A_{yo} are the real amplitudes for a single pole emission and $\phi = \omega \Delta t$. We see therefore that both components are imaginary, from which it follows directly from Eqs. (26) that in general $S_2 \neq 0$ and $S_3 = 0$. The polarization is therefore always linear, however the direction of polarization changes in a complicated way as a function of angle and harmonic number [119]. Averaging the intensities over frequency (i.e. ϕ) we return to the wiggler case with $\langle S_2 \rangle = 0$.

In order to obtain circularly polarized, or variably polarized, radiation therefore requires a special type of insertion device. In the following sections we consider the many types that have been developed over the years (see also Ref. [53]). The majority are helical or elliptical devices, with combined horizontal and vertical field components. The horizontal field component introduces a vertical acceleration and hence vertical electric field component even when the radiation is viewed on axis. Another type is the asymmetric wiggler: in this case there is no horizontal field component, however the cancellation of the circularly polarized component that occurs off-axis in a conventional device is avoided by making the field strengths of the positive and negative poles unequal. A third type is the crossed-undulator: in this case circular polarization is generated by the interference of the radiation emitted in successive horizontal and vertically polarized undulators.

7.3 Helical/elliptical devices

7.3.1 Magnetic configurations

Many different schemes have been put forward that can generate helical or elliptical field distributions, using both electromagnets and permanent magnets in various configurations - either with a helical geometry, a combination of separate horizontal and vertical devices, or with an open-sided (planar) structure - and as result, with either fixed or variable polarization.

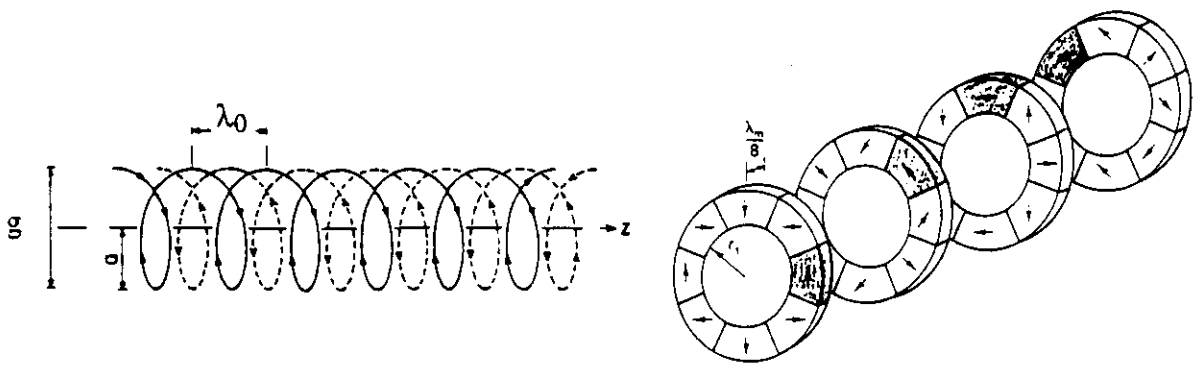

Fig. 45 Two methods for producing a pure helical field; left - the classical bifilar helix, right - a sequence of dipole magnets using permanent magnets

The classical method of producing a pure helical field is the "bifilar helix" (Fig. 45, left): a conductor is wound on a cylindrical former with diameter g and with a pitch λ_o forming a helical coil. A second winding is then added in between the windings of the first coil. When a current I is passed in opposite directions through the two windings the solenoidal field is cancelled, leaving a periodic helical field:

$$B_x = B_o \cos(kz) \qquad B_y = B_o \sin(kz)$$

The field amplitude for the case of wires with infinitesimal cross-section is given by [120]:

$$B_o = \frac{2\mu_o I}{\lambda_o}\left[\xi K_0(\xi) + K_1(\xi)\right]$$

where $\xi = \pi g/\lambda_o$ and K_0, K_1 are modified Bessel functions. The above expression shows a rapid decrease in field amplitude as λ_o/g reduces, analogous to the behaviour of linearly

polarized electromagnets and permanent magnets. Approximate expressions for a distributed winding were derived in Ref. [121]. Details of the field components generated on and off-axis were considered in [122] and end-effects in Ref. [123]. In this design the polarization direction (right- or left-handed) is determined by the sense of the winding. The possibility of superposing windings of opposite handedness to generate arbitrary polarization was suggested in Ref. [124]. The field generated by the bifilar helix is significantly less than for a conventional electromagnet [125] because of the lack of iron poles. Because of this fact, and the disadvantages associated with a closed structure for magnetic measurements and ease of installation etc., few magnets of this type have been built. The first FEL experiment at Stanford employed a superconducting helical magnet [126], while a pulsed magnet was used in the early FEL experiments at Frascati [127].

A higher field level can be obtained by incorporating iron poles. An example of a magnet of this type is the superconducting helical undulator installed in the VEPP-2M storage ring in Novosibirk in 1984; prior to this a non-superconducting version was operated to which iron poles were added later to enhance the field level [86]. For the FEL experiment of the Bell Laboratories a novel scheme was devised in which the iron poles were fed by straight, rather than helical conductors [128]. Another scheme is presented in Ref. [129].

Helical arrangements of permanent magnets have also been considered. The design proposed in Ref. [130] consists of N "slices" per magnet period, where each slice is an annulus containing segments of permanent magnet material with a suitable direction of magnetization to create a dipole field (Fig. 45, right). The slices are arranged along the length of the undulator with a $2\pi/N$ rotation from one slice to the next, so creating a helical field. Similar field strengths can be generated in this way compared to the linear undulator geometry [125]. A method of producing blocks with the required magnetisation directions was put forward in Ref. [131] while an alternative consisting of a large number of small rectangular blocks was considered in [132].

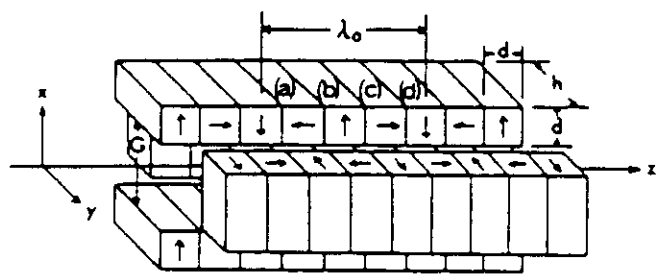

Fig. 46 Variably polarized undulator

A more flexible scheme consists of a superposition of separate horizontally and vertically polarized devices with a variable longitudinal displacement between them [133]. In general such a configuration allows the flexibility to change both the field amplitudes, B_{xo}, B_{yo}, and the phase between them, ψ:

$$B_x = B_{xo}\cos(kz + \psi) \qquad B_y = B_{yo}\cos(kz) \tag{28}$$

and as a result, any polarization state can be created. We can see this in a simplified way by using Eqs. (25) and (27) above and equating the acceleration with the corresponding field component ($E_x \sim \beta_x \sim B_y$ etc.). We obtain then that:

$$A_x \sim B_{yo} \qquad A_y \sim B_{xo}\,(\cos\psi - i\sin\psi)$$

from which it follows from Eqs. (26) that:

$$S_0 \sim B_{yo}^2 + B_{xo}^2 \qquad S_1 \sim B_{yo}^2 - B_{xo}^2$$
$$S_2 \sim 2\,B_{xo}\,B_{yo}\cos\psi \qquad S_3 \sim 2\,B_{xo}\,B_{yo}\sin\psi$$

This analysis is valid for the first harmonic and for small K. The original proposal was an undulator consisting of identical permanent magnet arrays, as shown in Fig. 46, and therefore generating equal field strengths in both directions. A prototype device was subsequently constructed and installed in the TERAS ring in Japan and the polarization of the emitted radiation measured [134]. In such a structure changing the phase changes the polarization but does not change the field amplitudes, or the wavelength of the radiation (see 7.3.2). The polarization and the radiation wavelength can therefore be changed independently.

With unequal field amplitudes in the two directions higher harmonics are generated with, in general, elliptical polarization [135]. Two permanent magnet devices of this kind were later constructed and installed in the TRISTAN Accumulator Ring and the Photon Factory [136]. These devices made use of the fact that the vertical magnet gap (30 mm) could be much smaller than the horizontal one (110 mm) so allowing a much higher field strength in the vertical direction, 1.0 T (K_y = 15) compared to the horizontal, 0.2 T (K_x = 3). Such a device became known as an elliptical multipole wiggler (EMPW). Later measurements confirmed that a high degree of circular polarization could be obtained at high photon energies [137].

The idea of replacing the permanent magnet arrays in the above scheme with an electromagnet in order to allow a rapid switching of the polarization state was first mentioned in [133]. Since an electromagnet requires a longer period length, and generates a smaller field strength than a permanent magnet, the idea is more applicable to the case of an elliptical wiggler. The first proposal for an electromagnetic elliptical wiggler (EEW) capable of reaching a switching speed of 100 Hz was made in [138]. A prototype device was later built by an APS/BINP/NSLS collaboration and installed in the NSLS X-ray ring [139]. A similar device was subsequently installed in the APS. A device consisting of two electromagnets, with the possibility also of shifting one magnet with respect to another has recently been proposed at LURE [140].

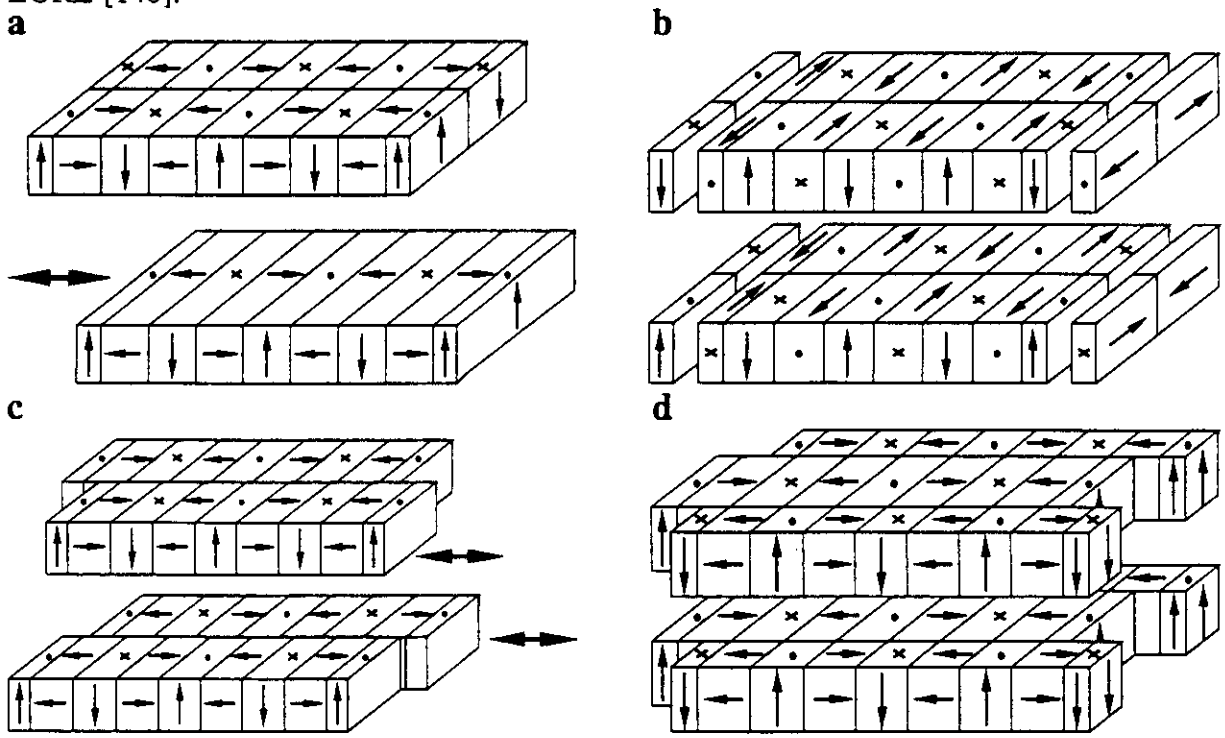

Fig. 47 Various planar permanent magnet arrangements.
a - HELIOS, b - planar helical undulator, c - APPLE-II, d - Spring-8

A disadvantage of all of the above schemes is the need for magnetic arrays on all sides of the electron beam tube. This not only complicates magnetic measurements and installation, but also means that the minimum gaps that can be achieved are restricted by the lateral size of the magnetic structures. Alternative "planar" structures have therefore been devised with magnets located only above and below the beam axis. The first proposal of this kind is shown in Fig. 47

(a) [141]. In this scheme the upper array produces a horizontal field, while the lower array produces a vertical field. The field components on-axis are therefore identical to those of the Onuki device given by Eq. (28), and hence by adjusting separately the upper and lower half-gaps and the longitudinal phase shift any polarization state can be generated. Owing to the lack of symmetry this device produces a linear variation of both field components in the vertical direction, thereby increasing the sensitivity of the radiation wavelength to beam position. A further potential problem is the fact that the fields give rise to a second-order deflection of the trajectory in the horizontal direction when $\psi \neq 0$, and in the vertical direction when $B_{xo} \neq B_{yo}$ [142]. Since these effects are of second-order and therefore inversely proportional to Energy^2, the effects may become problematic in low energy rings. In the ESRF the horizontal deflection is overcome using two separate undulators with opposite helicity so that the two deflections cancel [143]. The two undulators are used in a "chicane" arrangement to produce radiation with opposite helicity displaced slightly to the left and right of the beam axis. The HELIOS device was installed in the ESRF in June 1993; no effect on beam lifetime was observed, and only small changes in closed orbit were produced, in agreement with expectations [67]. Two further single section structures have subsequently been installed [144].

A modification of the HELIOS device is the planar helical undulator [142], shown in Fig. 47 (b). In this case both arrays produce a pure helical field, with equal field amplitudes that exceed that of the HELIOS device in the helical mode. A further advantage of this structure is that the symmetrical arrangement eliminates any second-order deflections. A significant disadvantage however is that the helicity is fixed.

More recently a further device was developed called APPLE (Advanced Planar Polarized Light Emitter), which produces even higher field amplitudes. The first structure to be put forward (APPLE-I) employed magnet blocks with a 45^o magnetization [145]. Subsequently a simpler structure (APPLE-II) was developed in which each of the four arrays has a conventional Halbach structure [146], shown in Fig. 47 (c). This version, as well as being easier to construct, produces a larger B_x field at the expense of smaller B_y and hence also a higher field in the helical mode. In both versions the polarization is altered by shifting the upper-back and lower-front arrays with respect to the upper-front and lower-back arrays. Considering for simplicity a shift of $\pm\psi$ for the pairs of arrays, the upper-back and lower-front arrays produce a linearly polarized field given by:

$$B_x = B_{xo}/2 \ \cos(kz - \psi) \qquad B_y = B_{yo}/2 \ \cos(kz - \psi)$$

whereas the upper-front and lower-back arrays generate a field given by:

$$B_x = -B_{xo}/2 \ \cos(kz + \psi) \qquad B_y = \ B_{yo}/2 \ \cos(kz + \psi)$$

Adding the two together and simplifying results in the following:

$$B_x = B_{xo} \sin(kz) \ \sin(\psi) \qquad B_y = B_{yo} \cos(kz) \cos(\psi)$$

Thus, unlike the Onuki and HELIOS cases, the field amplitudes do depend on ψ, and so the polarization cannot be adjusted independently of the radiation wavelength. In addition, changing the gap changes the horizontal and vertical fields by a different amount, and so changes the polarization. An interesting property of this device is that the two field components remain 90^o out of phase, and hence the polarization ellipse remains upright. The simple polarization analysis gives in this case (in the low K limit):

$$S_1 \sim B_{yo}^2 \cos^2\psi - B_{xo}^2 \sin^2\psi \qquad S_2 \sim 0 \qquad S_3 \sim B_{xo} B_{yo} \sin 2\psi$$

The APPLE configuration has a greater degree of symmetry than the HELIOS one, which eliminates problems due to second-order steering effects. The transverse field homogeneity remains considerably worse than in a conventional device, however experience with operating devices and beam dynamics calculations do not indicate any major problems.

The first test of the APPLE-I device was made with a seven-period prototype in the JAERI Storage Ring (JSR) [147]. Visible light was generated with variable polarization with a ring energy of 138 MeV. No beam deflections were observed while changing the gap or the phase.

An APPLE-II device was subsequently constructed for the SPEAR storage ring. This device includes a further feature, namely the ability to change the field strengths by phase rather than gap variation [148]. This is achieved by shifting the relative positions of the two upper arrays with respect to the two lower ones, or the two front arrays with respect to the two back arrays. In this way no gap adjustment is required to set any desired output wavelength and ellipticity. The device was subsequently tested in SPEAR with no noticeable effect on the 3 GeV beam for any longitudinal motion of the arrays [149]. Further devices are under construction for ALS, BESSY-II and TLS, and are planned for the SRS.

Finally, a structure consisting of six magnet arrays has been proposed by the Spring-8 team [150], shown in Fig. 47 (d). In this case the upper and lower central arrays generate a vertical field while the outer four arrays generate a horizontal field. The longitudinal phasing of the outer arrays with respect to the central arrays allows the polarization to be adjusted. A disadvantage of the structure however is that it is not possible to achieve both pure horizontal and vertical polarization unless at least five of the arrays are moveable: if the central arrays are fixed, then there is always a vertical field present, while if the outer arrays are fixed there is always a horizontal field. Both versions are planned for Spring-8, while the former type has been constructed and installed recently in the UVSOR storage ring. It has been claimed that this structure results in a better transverse field homogeneity than the APPLE design, and therefore produces less effect on the electron beam dynamics.

7.3.2 Radiation properties

We firstly consider how the interference condition is modified in the presence of an additional horizontal field component, at an arbitrary phase with respect to the vertical field component:

$$B_x = B_{xo}\sin(kz+\psi) \qquad B_y = B_{yo}\sin(kz)$$

The electron motion is then:

$$\beta_y = -\frac{K_x}{\gamma}\cos(kz+\psi) \qquad \beta_x = \frac{K_y}{\gamma}\cos(kz)$$

where $K_x = \frac{eB_x\lambda_o}{2\pi mc}$, and $K_y = \frac{eB_y\lambda_o}{2\pi mc}$. Since the electron velocity is given by $\beta^2 = \beta_x^2 + \beta_y^2 + \beta_z^2$ we have therefore:

$$\beta_z \cong \beta\left(1 - \frac{K_x^2}{4\gamma^2} - \frac{K_y^2}{4\gamma^2} - \frac{K_y^2}{4\gamma^2}\cos 2kz - \frac{K_x^2}{4\gamma^2}\cos 2(kz+\psi)\right) \tag{29}$$

For the interference condition only the average velocity along the z-axis is important, which is simply:

$$\overline{\beta} \cong \beta\left(1 - \frac{K_x^2}{4\gamma^2} - \frac{K_y^2}{4\gamma^2}\right)$$

Applying the interference condition, Eq. (3), then gives:

$$\lambda = \frac{\lambda_o}{2\gamma^2}\frac{1}{n}\left(1+\frac{K_x^2}{2}+\frac{K_y^2}{2}+\gamma^2\theta^2\right) \tag{30}$$

Thus the radiation wavelength depends only on the amplitudes of the two field components, independently of the phase ψ between them.

The analysis of the radiation emission in the general case is quite complicated (see Appendix). In the particular case of on-axis radiation for $\psi = \pi/2$ the angular flux density can be written, in practical units, as follows:

$$\left.\frac{d^2\dot{n}}{d\omega/\omega\ d\Omega}\right|_{\theta=0} = 1.744\ 10^{14}\ N^2\ E^2_{[GeV]}\ F_n(K_x,K_y)\ I_b$$

where

$$F_n(K_x,K_y) = \frac{n^2}{(1+K_x^2/2+K_y^2/2)^2}\left(A_x^2+A_y^2\right)$$

and

$$A_x = K_y\left(J_{\frac{n+1}{2}}(Y) - J_{\frac{n-1}{2}}(Y)\right),\quad A_y = K_x\left(J_{\frac{n+1}{2}}(Y) + J_{\frac{n-1}{2}}(Y)\right)$$

with

$$Y = \frac{n\,(K_y^2-K_x^2)}{4(1+K_x^2/2+K_y^2/2)}$$

The integrated flux is then given, see Eq. (18), by:

$$\frac{d\dot{n}}{d\omega/\omega} = 1.431\ 10^{14}\ N\ Q_n(K_x,K_y)\,f(N\Delta\omega/\omega_1(0))\ I_b$$

where $Q_n(K_x,K_x) = (1+K_x^2/2+K_y^2/2)\,F_n(K_x,K_x)/n$. The Stokes parameters are given by:

$$S_1/S_0 = \left(A_x^2-A_y^2\right)/\left(A_x^2+A_y^2\right)$$
$$S_2/S_0 = 0$$
$$S_3/S_0 = -2A_xA_y/\left(A_x^2+A_y^2\right)$$

In the case of purely circular motion, when $K_x = K_y = K$ (and $\psi = \pi/2$) the longitudinal velocity, Eq. (29), is constant. As a result the electric fields E_x and E_y are purely sinusoidal and so the radiation consists of a single harmonic on axis. This is evident also in the formula above since when $Y = 0$ the only non-zero term is $J_0(0)$ which occurs only for $n = 1$. We have therefore:

$$F_1(K) = \frac{2K^2}{(1+K^2)^2} \quad \text{and} \quad Q_1(K) = \frac{2K^2}{(1+K^2)}$$

and the radiation is purely circularly polarized:

$$S_1/S_0 = 0, \qquad S_2/S_0 = 0, \qquad S_3/S_0 = 1$$

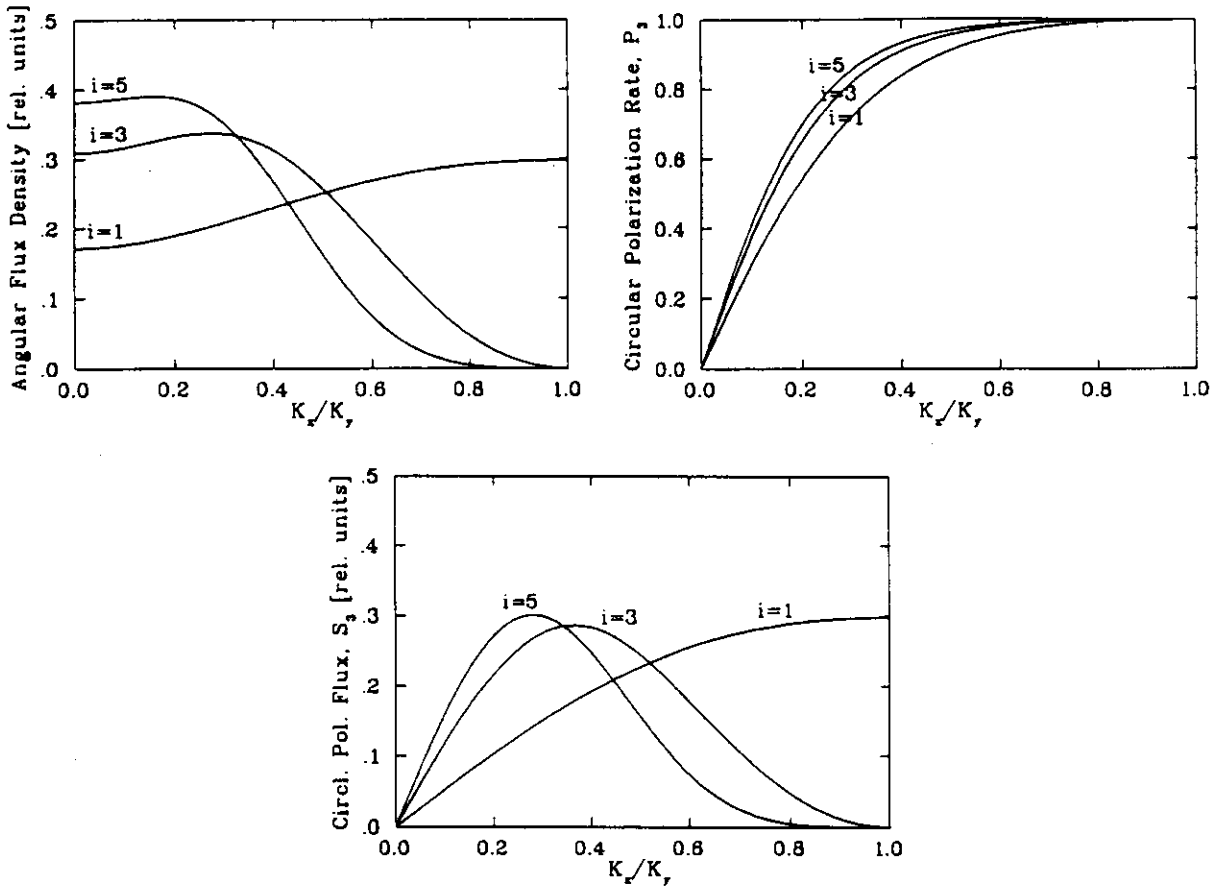

Fig. 48 Variation of (a) angular flux density, (b) circular polarization rate and (c) circularly polarized flux density with ratio K_x/K_y for $K_x^2 + K_y^2 = 3^2$

Figure 48 shows the variation of angular flux density, circular polarization rate and their product (S_3) as a function of the ratio between the horizontal and vertical field strengths with a fixed radiation wavelength (i.e. fixed $K_x^2 + K_y^2$). For $K_x/K_y = 0$ we have the same result for a plane undulator, with pure linear polarization. As K_x/K_y increases both the flux and circular polarization rate increase for the fundamental. The maximum circularly polarized flux is therefore obtained with pure circular polarization with $K_x = K_y$. In the case of the higher harmonics however the circular polarization rate increases, but the flux eventually tends to zero at $K_x = K_y$. There is therefore an optimum value of K_x/K_y which maximizes S_3, which depends on the harmonic number (and on $K_x^2 + K_y^2$).

The angular distribution of the power density in the elliptical case ($\psi = \pi/2$) is obtained from Eq. (19) with $\upsilon_x = K_y \sin\alpha - \gamma\theta_x$ and $\upsilon_y = K_x \cos\alpha - \gamma\theta_y$ from which one obtains:

$$\frac{dP}{d\Omega}[\mathrm{W/mrad^2}] = 13.44\ 10^{-3}\ E^4_{[GeV]}\, I_b \frac{2\pi}{\lambda_o} N \int_{-\pi}^{\pi} \left\{ \frac{(K_y^2 \cos^2\alpha + K_x^2 \sin^2\alpha)}{D^3} - \frac{\left[(K_y^2 - K_x^2)\sin 2\alpha - 2K_y\,\gamma\theta_x \cos\alpha + 2K_x\,\gamma\theta_y \sin\alpha\right]^2}{D^5} \right\} d\alpha$$

where $D = 1 + (K_y \sin\alpha - \gamma\theta_x)^2 + (K_x \cos\alpha - \gamma\theta_y)^2$. In the case of pure helical motion, $K_x = K_y$, the on-axis result becomes simply:

$$\frac{dP}{d\Omega}[\mathrm{W/mrad^2}] = 13.44\ 10^{-3}\ E^4_{[GeV]}\, I_b \left(\frac{2\pi}{\lambda_o}\right)^2 L\, \frac{K^2}{(1+K^2)^3}$$

which shows a maximum for $K = 1/\sqrt{2}$. For larger K the on-axis power density decreases rapidly as most of the power is emitted off-axis, with a maximum near the angle K/γ [15]. The total power emitted is given from Eq. (20) as:

$$P_{tot}[\mathrm{W}] = 633.\ E^2_{[GeV]}\ (B^2_{xo} + B^2_{xo})\ L\, I_b$$

7.4 Asymmetric wiggler

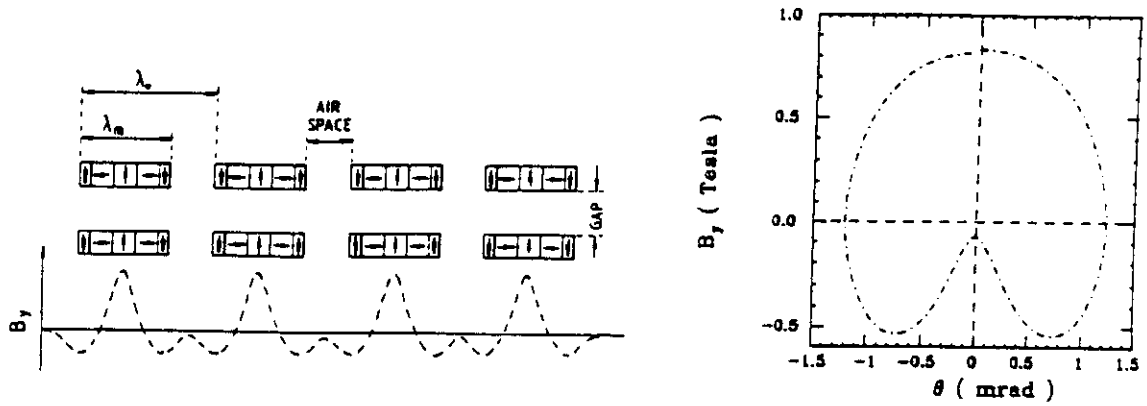

Fig. 49 Asymmetric wiggler; left - permanent magnet structure and field distribution, right - variation of magnetic field with emission angle [152].

An asymmetric wiggler is a planar device with a single on-axis field component but differs from a conventional insertion device in that the positive and negative field strengths are of unequal magnitude [151]. The first asymmetric wiggler was constructed at HASYLAB in 1989 and employed a pure permanent magnet construction, illustrated in Fig. 49 (left) [152]. In a normal sinusoidal wiggler the radiation emitted at a given horizontal angle has two source points per period with equal positive and negative field amplitudes. In an asymmetric wiggler however this symmetry is broken and the field values are no longer equal, as illustrated in Fig. 49 (right). As a result, circularly polarized radiation is emitted off-axis in the vertical direction as in a single bending magnet. It can be seen that the difference between the field values is greatest at zero horizontal angle and decreases with increasing angle. The circular polarization rate therefore follows the same trend, as can be seen in Fig. 50 (left), calculated for the structure of Fig. 49. Another related feature of this device is that the total intensity peaks off-axis in the horizontal direction. It is clear that the highest circular polarization rate is obtained close to zero horizontal angle and also off axis vertically, and there is therefore a compromise between flux and degree of circular polarization. Figure 50 (right) shows the integrated flux, circularly polarized flux and circular polarization rate for a particular case, with horizontal acceptance of ± 0.25 mrad and vertical acceptance from 0.1 to 0.2 mrad. The characteristic feature can be seen that the circularly polarized flux S_3 changes sign at low photon energies when the lower field pole (with negative S_3) contributes more than the higher field pole (with positive S_3). On the other hand at the highest photon energies the contribution of the lower field pole becomes negligible, resulting in increasing polarization rate, but rapidly diminishing flux.

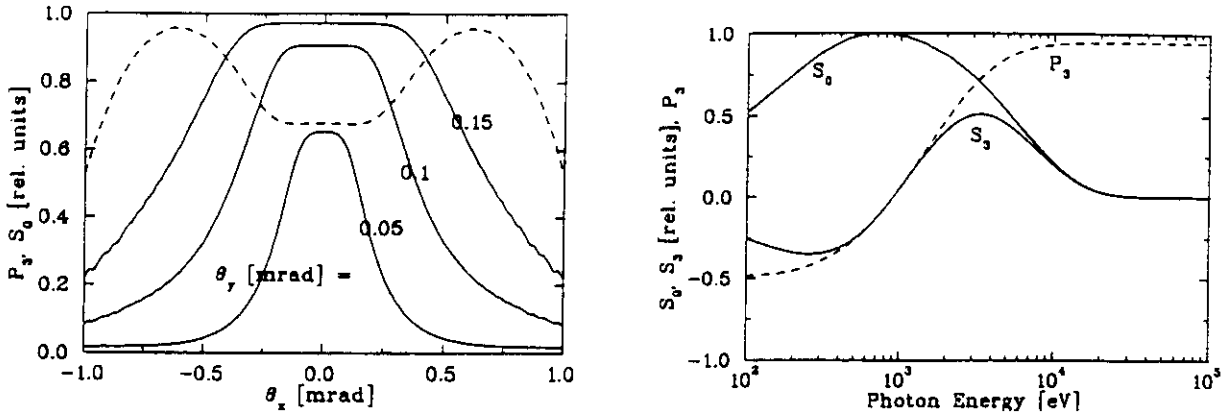

Fig. 50 Performance of the asymmetric wiggler shown in Fig. 49;
left - circular polarization rate as a function of horizontal and vertical angle for 10 keV radiation, dotted line - total intensity at $\theta_y = 0.1$ mrad; right - integrated flux and circular polarization rate as a function of energy.

Further asymmetric wigglers have been built using the hybrid technology (i.e. with iron poles) at LURE [153], HASYLAB [154] and ESRF [144]. A superconducting asymmetric wiggler has also been constructed for DELTA [155]. The LURE and ESRF designs are similar and are obtained by splitting every alternate pole into two and separating by a drift space. The HASYLAB design on the other hand incorporates zero-potential field clamps rather than drift spaces. In the pure permanent magnet case, linear superposition guarantees that although the field amplitudes are different for each pole, the field integrals are equal. In the hybrid case this is no longer true, and the main problem in the design is therefore to achieve a compensation of the vertical field integral at all operating gaps. Three dimensional computations are therefore very useful in order to reduce the correction needed with coils etc.

7.5 The crossed undulator

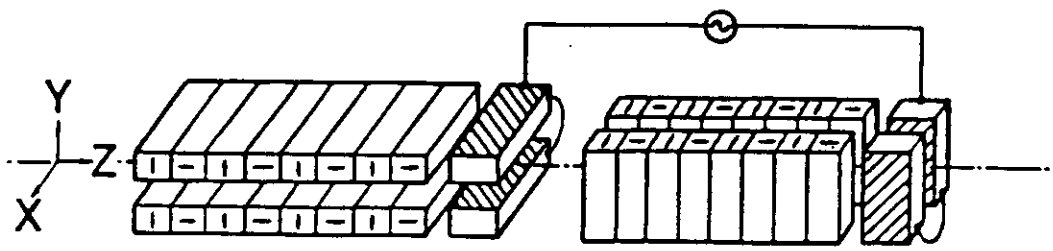

Fig. 51 The crossed undulator

The crossed undulator [156] consists of two separate linearly polarized undulators with polarization at right-angles to each other, separated by a "modulator" magnet (see Fig. 51). The purpose of the latter is to create a compensated bump in the electron trajectory and hence introduce a variable phase delay between the radiation emitted in the two undulators. The resulting interference produces elliptically polarized radiation on-axis.

A simple analysis of the polarization properties can be made by summing the amplitudes from the two undulators:

$$\underline{A} = \left[\underline{A_1} + \underline{A_2}\, e^{i(N\delta+\psi)}\right] \frac{\sin N\delta/2}{\sin \delta/2}$$

where $\delta = 2\pi\Delta\omega/\omega_1(\theta)$ is the phase advance per period in the first undulator and ψ is the extra phase change introduced by the modulator, which is assumed constant over the small range of frequencies that we will be considering. Assuming that the two undulators are identical

(each with N periods) and that the first undulator is polarized in the horizontal direction and the second in the vertical direction we obtain:

$$A_x = A\frac{\sin N\delta/2}{\sin \delta/2} \qquad A_y = A\, e^{i(N\delta+\psi)}\frac{\sin N\delta/2}{\sin \delta/2}$$

from which it follows that:

$$S_0 = 2A^2\,\frac{\sin^2 N\delta/2}{\sin^2 \delta/2}$$

$$S_1 = 0$$

$$S_2/S_0 = \cos(N\delta + \psi)$$

$$S_3/S_0 = \sin(N\delta + \psi)$$

At zero detuning therefore ($\delta = 0$) the polarization changes with the modulator phase in the following way:

Phase (ψ)	S_2/S_0	S_3/S_0	Polarization
0°	1	0	linear at 45°
90°	0	1	right-handed circular
180°	-1	0	linear at -45°
270°	0	-1	left-handed circular
360°	1	0	linear at 45°

A rapid change of polarization can be made if the modulator is a suitably designed electromagnet. An interesting feature of the device is that, unlike helical magnets, even with pure circular polarization higher harmonics are generated on-axis, since each individual linear undulator generates higher harmonics.

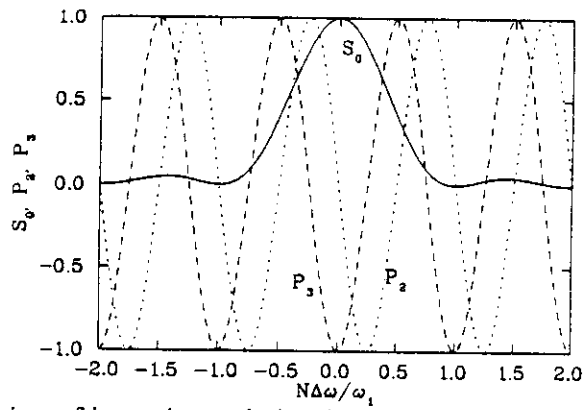

Fig. 52 Variation of intensity and circular polarization rates with frequency in a crossed undulator

From the equation above it is clear that the polarization changes rapidly with the detuning parameter, and this is illustrated in Fig. 52. For example, with $\psi = \pi/2$ we obtain pure circularly polarized radiation on axis. At $\Delta\omega/\omega_1 = 1/4N$ however this becomes zero, whereas the total flux becomes zero only at $\Delta\omega/\omega_1 = 1/N$. Certain conditions must therefore be met in order to obtain significant circular polarization:

- selection of a narrow range of photon energies, $\Delta\omega/\omega \le 1/2nN$. Under normal circumstance this is not a problem since the monochromator provides a significantly smaller band-pass;

- selection of a narrow range of acceptance angles, $\theta \leq \sqrt{\lambda/2L}$. In other words, the acceptance angle must be restricted with a "pinhole" aperture so as to receive only a fraction of the available flux;
- it follows from the above that the electron beam divergence must also be sufficiently small, $\sigma_\theta \leq \sqrt{\lambda/2L}$;
- similarly, the energy spread of the electron beam must be sufficiently small, $\Delta E/E \leq 1/8nN$.

It should be noted that in all cases the sensitivity increases for the higher harmonics.

The first, and so far only, device of this type to be built is operational in BESSY [157]. The present modulator is not laminated and so does not permit a fast switching. A crossed undulator that was proposed for the ALADDIN storage ring [158] incorporated a modulator that was designed to reach a switching speed of 10 Hz [159].

Alternative geometries to the one presented above are also possible. With the two undulators oriented at 45° and -45° with respect to the x-y axes results in an exchange of the S_1 and S_2 parameters, i.e. allowing horizontal and vertical polarization to be obtained as well as circular polarization. A combination of right- and left-handed circularly polarized undulators creates linearly polarized radiation ($S_1 \neq 0$, $S_2 \neq 0$, $S_3 = 0$). In this case however the interesting situation arises that since only a single harmonic is generated on-axis in each device, the linearly polarized radiation consists only of a single harmonic [160].

8. UNDULATORS FOR FREE-ELECTRON LASERS

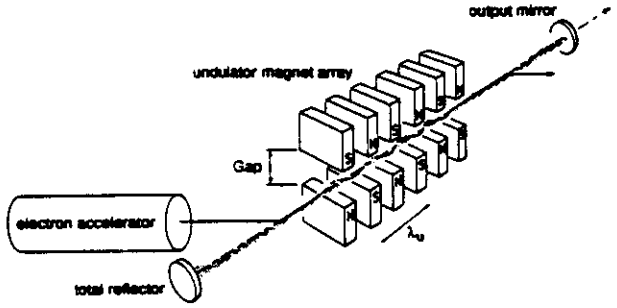

Fig. 53 Basic scheme of a free-electron laser

In a free-electron laser (FEL) the presence of a static periodic magnetic field produced by an undulator magnet allows an exchange of energy between an electron beam and a co-propagating radiation beam, resulting in the emission of coherent radiation [161]. The resonance condition governing this interaction and which determines the laser output wavelength is identical to the interference condition derived earlier, Eq. (3). An undulator is therefore one of the principle components of a FEL. The same type of undulator used as a synchrotron radiation source can be used, however there are a number of additional requirements and circumstances that apply in the case of the FEL and as a result many different kinds of magnet design have been developed for this specific application.

In the following we will firstly consider the various undulator configurations that have been developed in order to enhance the FEL interaction. Other important differences in the characteristics of FEL undulators compared to those used as synchrotron radiation sources arise in cases in which the electron beam passes only once through the undulator i.e. single-pass devices, driven by a linac beam for example. In this case a much smaller gap can be employed, since there are no restrictions due to the beam lifetime. A great deal of activity has therefore been devoted to the development of small-period devices of various types, in order to reach the shortest possible wavelength with a given electron beam energy. Some of these devices are pulsed electromagnets, since the electron beam itself is generally pulsed. Another important requirement in the case of FEL undulators is the need to incorporate additional focusing into the magnetic structure, in order to obtain a better overlap of the electron and photon beam sizes and so optimize the FEL interaction. Further details on FEL undulator construction and measurement can be found in the Proceedings of the annual International Free-Electron Laser Conferences [162].

8.1 Undulator configurations

The two main quantities that characterize the performance of a FEL oscillator are the small-signal gain, which determines how rapidly the signal builds up, and the efficiency, which determines what fraction of the electron beam energy can be converted into radiation intensity. The efficiency is limited by the fact that at saturation the electrons loose so much energy per pass that they fall out of resonance. To overcome this a *tapered undulator* is sometimes adopted in which the period and/or field strength are profiled along the length of the magnet in order to match the desired decrease in electron energy [163]. Several experiments were carried out to confirm the theoretical predictions in an amplifier configuration, using permanent magnet undulators with up to 9 % energy tapering [164]. An example of a tapered electromagnetic device is the 25 m long wiggler built for the PALADIN FEL experiments [165]. In this device each two-periods were excited with a separate power supply in order to allow a variable tapering. In order that the adjustment of the taper would cause no net displacement of the electron beam the excitation pattern applied was compensated as for a conventional entrance/exit sequence i.e. each five poles were excited with a sequence +1, -2, +2, -2, +1. More complex excitation patterns have also been studied [166].

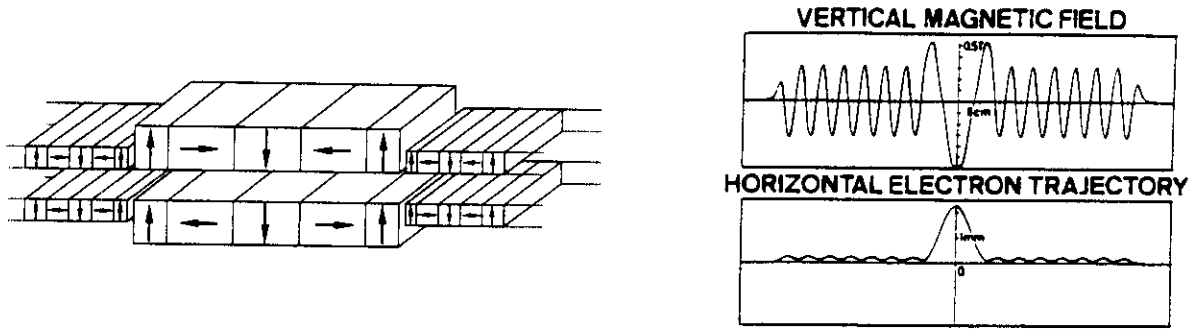

Fig. 54 Schematic of a pure permanent magnet optical klystron (left); field and electron trajectory in the Orsay device (right) [168].

Another variant of the basic FEL undulator is the so-called *optical klystron* [167], see Fig. 54. This consists of two identical undulators separated by a dispersive section, which introduces a compensated bump into the electron trajectory and hence a phase delay between the radiation emitted in the two magnets. The structure is therefore similar to that of the crossed undulator considered earlier (Section 7.5) except that in this case the undulators have the same polarization and the phase delay is much larger. The lineshape of the spontaneous or incoherent radiation spectrum becomes modulated, resulting in an enhanced gain. Alternatively one can consider that an energy modulation introduced in the first undulator by the interaction of the electron beam and radiation field is converted in the dispersive section into a density modulation, so that coherent emission takes place in the second undulator. Such a scheme is particularly useful in cases with small gain, but with sufficiently small energy spread, such as is often the case with a storage ring FEL. For this reason the optical klystron configuration has been chosen for all existing and previous SR-FEL experiments, on the ACO, DELTA, DUKE, NIJI-IV, SuperACO, UVSOR, and VEPP-3 storage rings. In almost all cases a linearly polarized undulator has been used, either permanent magnet or electromagnet. The exception is a helical optical klystron recently constructed for UVSOR [169].

A similar arrangement to the optical klystron is one in which the second undulator emits coherent radiation at a harmonic of the frequency of the first undulator [170] and is therefore called a *harmonic generation* scheme.

The disadvantage of a tapered undulator is that it results in a lower small-signal gain and is only optimized at a given power level. As a result it is not ideal in an oscillator configuration when a rapid increase of power is required. In order to overcome this problem and so provide a high output power oscillator a *multi-component* design was put forward, which includes a number of constant and tapered sections as well as a dispersive region as in an optical klystron [171]. Successful operation of an oscillator using this scheme was later reported [172].

8.2 Small-period devices

Various approaches have been taken to the construction of small-period FEL undulators. First of all, conventional permanent magnet devices can be scaled down quite successfully to smaller period and gap. For example, a 5 m tapered hybrid undulator with 21.8 mm period and 4.8 mm gap was constructed by Spectra Technology Inc. for a visible FEL oscillator experiment [173]. A 20 mm period pure permanent magnet in-vacuum device was built for the FELI facility (Japan), which generated 0.85 T at 5 mm gap [174]. Various other hybrid devices have been built, the most advanced is that developed at CREOL (USA) having 185 periods of 8 mm, and which achieves a field of 0.2 T at 6 mm gap [175]. A number of alternative hybrid schemes have been investigated at the Kurchatov Institute. In one scheme the field of a conventional hybrid structure is augmented by side permanent magnets which direct extra flux into the gap region via C-shaped pole pieces [176]. Alternative pure permanent magnet schemes have also been developed that are more easily adaptable to short period lengths, such as that developed UCSB which consist of grooves ground in large blocks of permanent magnet material [177]; prototypes of this concept were built with 4 mm period, 2 mm gap and achieved fields of the order 0.1 T. The field was however considerably lower than could be achieved in a conventional pure permanent magnet, with the added difficulties of field offset, large end fields and significant field errors.

Various miniature electromagnetic schemes have also been developed, starting with a simple design in which a copper foil is wound between electric steel laminations in alternating directions [178]. A prototype with a period of 2.7 mm and gap of 1 mm produced a field amplitude of about 0.08 T in d.c. mode. Most later devices were designed to be pulsed in order to allow higher currents to be used without overheating. Another design based on a folded foil involved a double winding scheme, i.e. the foil is folded back at the end of the magnet and wound in the opposite sense, which has the advantage of producing a more symmetrical field distribution [179]. Periods as small as 5 mm were considered possible using this technique. Another approach which received a lot of attention was the slotted-tube device in which a high current pulse is passed along a cylindrical tube with appropriately positioned cut-outs to direct the current flow so as to generate the desired field configuration; several prototypes were built producing both helical and later planar fields and in one a field strength of 1 T was achieved with 5 mm period with a 25 kA pulse [180]. Another related idea was to use a bifilar helical sheet with ferromagnetic cores; a 10 mm prototype was constructed [181]. All of the above devices suffer from the disadvantage that there is no simple method for correcting field errors. An alternative approach which overcomes this problem uses individual small electromagnets, which allows independent tuning of the strength of each pole by means of a resistive current divider network feeding each pair of coils from a single power supply [182]. A 70 period device was constructed with a period of 8.8 mm and gap of 4.2 mm which generated a field amplitude of 0.42 T with excellent field quality [183].

Small-period devices have also been constructed using superconducting magnet technology. The design developed at BNL is based on a continuously wound conductor on a precisely machined iron yoke [184]. Two devices have been constructed for two different FEL experiments; the undulator with the shortest period (8.8 mm) produces a field of 0.5 T at 4.4 mm gap. Very good field uniformity was achieved within each section, although some errors appeared at the joints between sections [185].

Two other novel concepts that have been developed for producing sub-cm period undulators are an electromagnetic helical device based on a laminated construction with three poles per magnet period [186] and a device consisting of a staggered array of iron poles immersed in a solenoidal field produced by a superconducting magnet [187]. A 1 T sinusoidal field amplitude was generated for a 10 mm period at 2 mm gap with a 0.7 T solenoidal field.

8.3 Transverse focusing

A conventional linearly polarized undulator with a vertical field, causes a focusing of the beam in the vertical plane, whereas (ignoring the effects of any field errors) it acts like a drift space in the horizontal plane [29]. In the vertical plane therefore there exists a matching condition, such that if the electron beam ellipse is adjusted correctly at the entrance of the

magnet, it will remain unaltered as it progresses along the magnet. It can be shown that under these conditions the longitudinal velocity (averaged over an undulator period) is constant for each electron during its motion in the vertical plane, and that this is the optimum setting in order to minimize the effect of the electron beam emittance on the FEL interaction. The same situation however does not exist in the horizontal plane due to the lack of horizontal focusing. To remedy this situation, certain types of helical undulator can be used. For example, the bifilar helix produces equal focusing in both planes [121]. The double-undulator scheme of Onuki in the helical mode, with identical magnet arrays and equal gaps, also gives equal focusing, even though the field distribution is quite different to that of the bifilar helix [142]. The same is not generally true however for the other helical magnet schemes capable of generating circularly polarized radiation (Section 7.3).

In many cases a plane polarized magnet is preferred to a helix and considerable attention has been given to different ways of incorporating focusing in the horizontal plane. In Ref. [188] it was shown that in general a small parabolic curvature of the pole profile (assuming an iron-dominated electromagnet or hybrid device) is sufficient to produce equal focusing in both planes and that this has the advantage over the alternative method of adding focusing by means of linear field gradients that the longitudinal velocity, and hence the FEL resonance condition, remains constant. It was also shown that this difference can have a significant influence on FEL performance. One of the first magnets to be built incorporating this principle was the electromagnet for the PALADIN FEL experiment [165]. The idea is however quite an old one: focusing of this type was employed in the ubitron developed by Philips [5].

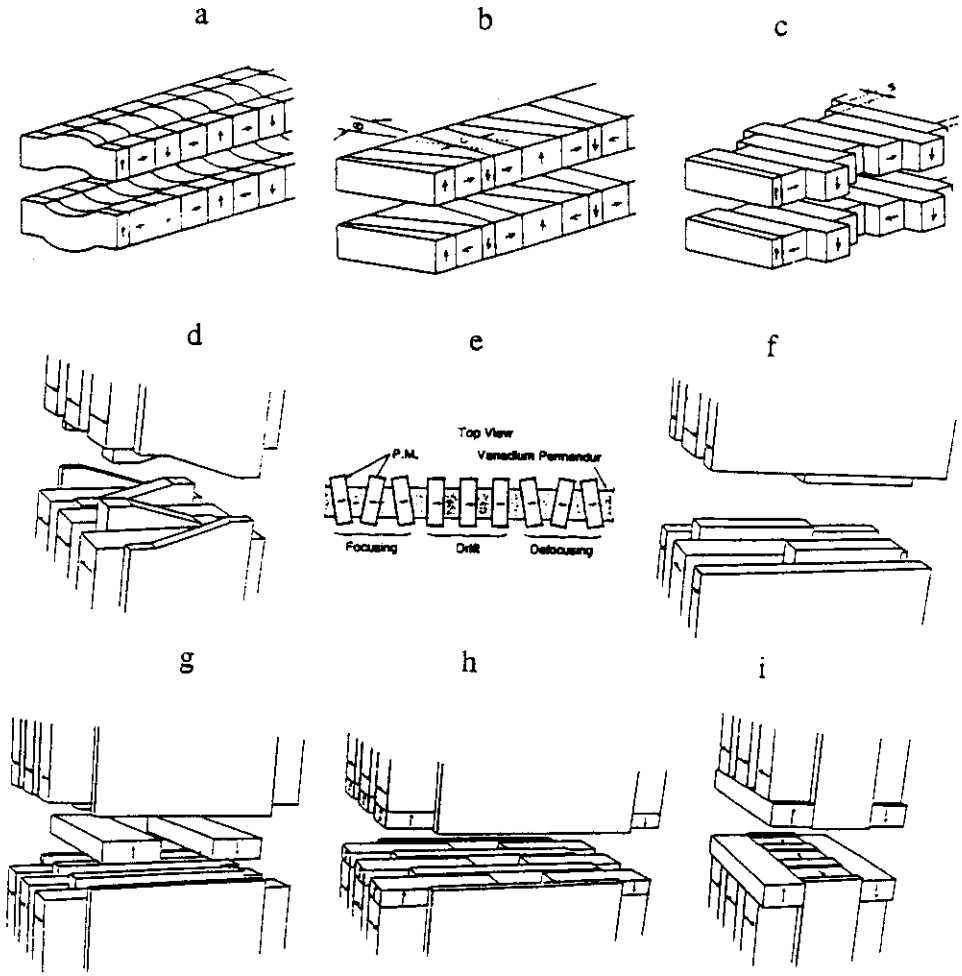

Fig. 55 Various schemes for introducing additional focusing in pure permanent magnet and hybrid undulators

Various schemes have been investigated for incorporating both types of focusing, quadrupole and sextupole-like, into permanent magnet FEL undulators as shown in Fig. 55. In the case of the pure permanent magnet configuration, it has been shown that curved blocks (Fig. 55a) can introduce sextupole-like focusing [189], while trapezoidal (Fig. 55b) [189] and staggered blocks (Fig. 55c) [190] can introduce quadrupole-like focusing. In the case of hybrid designs, alternate pole canting (Fig. 55d) has been applied on several occasions to produce additional quadrupole focusing [173]; displacing the poles transversely in alternating directions (Fig. 55f) has a similar effect. It has been suggested that a simple method of introducing sextupole focusing is to cut a rectangular slot in the pole, rather than curving the pole surface [191]. Another possibility is the use of additional side magnets. If the side blocks are arranged so that their magnetization directions are opposite to the direction of the field in the gap on both sides of the magnet, the field amplitude is increased and a sextupole field is generated providing horizontal focusing. Such a scheme was adopted for the FOM-FEM project [192].

In the case of short wavelength single-pass FEL experiments in particular there is a need for very strong focusing to maintain small beam dimensions over the required long undulator lengths of 15-50 m. In this case natural sextupole focusing is insufficient, and instead strong superimposed quadrupole fields of 20-50 T/m must be used with alternating gradient. One of the possibilities being investigated for the LCLS project is a canted and wedged pole hybrid (Fig. 55e) [193]. Another possibility is the use of side magnets, but differing from the scheme outlined above for producing sextupole focusing. In this case the side magnets have opposite directions of magnetization, and are continuous along the length of the magnet, and so produce a superimposed quadrupole field (Fig. 55g) [194]. A similar concept, but using four magnets above and below the median plane, and therefore having the advantage of leaving the sides open, was introduced in Ref. [195]. Two further related schemes of incorporating the additional magnets into the hybrid structure (Figs. 55h and 55i) were reported in [196]. One of these, the so-called four magnet focusing undulator (Fig. 55h), was subsequently selected for the undulator for the TTF-FEL project and is presently under construction. Various other schemes are also being studied for the LCLS project, including superconducting and pulsed copper helical magnets [197].

ACKNOWLEDGEMENTS

It is a pleasure to thank B. Diviacco for preparing several of the figures and for various helpful discussions and M. Nadalin for her skill and patience in preparing the manuscript.

REFERENCES

[1] V.L. Ginzburg, Izv. Akad. Nauk. SSSR, Ser. Fiz., 11 (1947) 165.
[2] H. Motz, J. Appl. Phys. 22 (1951) 527.
[3] H. Motz et al., J. Appl. Phys. 24 (1953) 826.
[4] I.A. Grishaev et al., Sov. Phys. Dokl. 5 (1960) 272.
[5] R.M. Phillips, Nucl. Instr. Meth. A272 (1988) 1.
[6] J.M.J. Madey, J. Appl. Phys. 42 (1971) 1906.
[7] R.P. Godwin, Synchrotron Radiation as a Light Source, Springer Tracts in Modern Physics, Vol. 51, Springer-Verlag (1969).
[8] D.F. Alferov, Yu. A. Bashmakov and E.G. Bessonov, Sov. Phys. Tech. Phys. 17 (1973) 1540.
[9] V.N. Baier et al., Sov. Phys. JETP 36 (1973) 1120.
[10] E.M. Purcell, unpublished note, July 1972 [also Ref. 18 p. IV-18].
[11] A.I. Alikhanyan et al., JETP Lett. 15 (1972) 98.
[12] D.F. Alferov et al., JETP Lett. 26 (1977) 385.
[13] A.N. Didenko et al., Sov. Tech. Phys. Lett. 4 (1978) 281.
[14] D.F. Alferov, Yu. A. Bashmakov and E.G. Bessonov, Sov. Phys. Tech. Phys. 18 (1974) 1336.
[15] B.M. Kincaid, J. Appl. Phys. 48 (1977) 2684.
[16] A.S. Artamonov et al., Nucl. Instr. Meth. 177 (1980) 247.
[17] K. Halbach et al., IEEE Trans. Nucl. Sci. NS-28 (1981) 3136.

[18] Proc. Wiggler Workshop, Stanford, March 1977, SSRP Report 77/05 (May 1977).
[19] H. Winick and R.H. Helm, Nucl. Instr. Meth. 152 (1978) 9.
[20] W.S. Trzeciak, IEEE Trans Nucl. Sci. NS-18 (1971) 213.
[21] M. Berndt et al., IEEE Trans. Nucl. Sci. NS-26 (1979) 3812.
[22] R. Barbini et al., Riv. del Nuov. Cim. 4 (1981) 1.
[23] E. Hoyer et al., IEEE Trans. Nucl. Sci. NS-30 (1983) 3118.
[24] A.S. Artamonov et al., Nucl. Instr. Meth. 177 (1980) 239.
[25] V.P. Suller et al., IEEE Trans. Nucl. Sci. NS-30 (1983) 3127.
[26] K.W. Robinson, Phys. Rev. 111 (1958) 373.
[27] A. Hofmann et al., Proc. VIth Int. Conf. High Energy Accelerators, Cambridge MA, (1967) p. 123.
[28] J.M. Paterson, J.R. Rees and H. Wiedemann,, SPEAR-186, PEP-125, July 1975.
[29] R.P. Walker, Proc. CERN Accelerator School Fifth Advanced Accelerator Physics Course, CERN 95-06, Vol. II, p. 807
[30] Proc. Wiggler Meeting, Frascati, June 1978, INFN (Dec. 1978).
[31] Proc. Int. Conf. on Insertion Devices for Synchrotron Sources, Stanford, Oct. 1985, SPIE Vol. 582 (1986).
[32] Proc. Adriatico Research Conference on Undulator Magnets for Synchrotron Radiation and Free Electron Lasers, Trieste, June 1987, World Scientific (1988).
[33] Proc. Workshop on Fourth Generation Light Sources, Stanford, Feb. 1992, SSRL 92/02
[34] Proc. Int. Workshop on Insertion Devices for Circularly Polarized Light, BESSY, Berlin, Nov. 1993.
[35] Proc. 10th ICFA Beam Dynamics Workshop: 4th Generation Light Sources, ESRF, Grenoble, Jan. 1996.
[36] J.E. Spencer and H. Winick, "Wiggler Systems as Sources of Electromagnetic Radiation", Chapter 21 in "Synchrotron radiation Research", H. Winick and S. Doniach eds., Plenum Press (1980).
[37] S. Krinsky, M.L. Perlman and R.E. Watson, "Characteristics of Synchrotron Radiation and of its Sources", Chapter 2 in "Handbook on Synchrotron Radiation", Vol. 1a, E.E. Koch ed. (North Holland, 1983).
[38] G. Margaritondo, "Introduction to Synchrotron Radiation" (Oxford, New York, 1988).
[39] P. Luchini and H. Motz, "Undulators and Free-Electron Lasers", Oxford University Press (1990)
[40] G. Brown and W. Lavender, "Synchrotron Radiation Spectra", Chapter 2 in "Handbook on Synchrotron Radiation", Vol. 3, G. Brown and D.E. Moncton eds. (Elsevier, 1991).
[41] G.S. Brown, "Undulators and the Properties of Synchrotron Radiation", Chapter 8 in "Synchrotron Radiation Research: Advances in Surface and Interface Science, Volume 2: Issues and Technology", R.Z. Bachrach ed., Plenum Press (1992).
[42] R.D. Schlueter, "Wiggler and Undulator Insertion Devices", Chapter 14 in "Synchrotron Radiation Sources: A Primer", H. Winick ed., World Scientific (1994).
[43] K.J. Kim, "Characteristics of Synchrotron Radiation", Proc. US Particle Accelerator School, 1987, M. Month and M. Dieses eds., AIP Conference Proceedings Vol. 184 p. 567.
[44] P. Elleaume, "Theory of Undulators and Wigglers", Proc. CERN Accelerator School, Synchrotron Radiation and Free-Electron Lasers, CERN 90-03 p. 142.
[45] M.R. Howells and B.M. Kincaid, "The Properties of Undulator Radiation", Proc. NATO ASI Series E, Vol. 254, p. 315.
[46] H. Winick et al., Physics Today 34, May 1981, p. 50.
[47] G. Brown et al., Nucl. Instr. Meth. 208 (1983) 65.
[48] P. Elleaume, Synchrotron Radiation News 1(4) (1988) 18 and 1(5) (1988) 21.
[49] R. Coïsson, Proc. 2nd EPAC, Nice, June 1990, Editions Frontières (1990) p. 291.
[50] P. J. Viccaro et al., Proc. PAC 1991, IEEE Catalog No. 91CH3038-7, p. 1091.
[51] P. Elleaume, Proc. SRI'91, Rev. Sci. Instr. 63 (1992) 321.
[52] F. Ciocci, Proc. 3rd EPAC, Berlin, March 1992, Editions Frontières (1992) p. 86.
[53] R.P. Walker, Proc. 4th EPAC, London, June 1994, World Scientific (1994), p. 310.

[54] H. Kitamura, Proc. SRI'94, Rev. Sci. Instr. 66 (1995) 2007.
[55] E. Gluskin and E.R. Moog, Proc. PAC 1995, IEEE Catalog No. 95CH35843, p. 1301
[56] G. Margaritondo, J. Synchrotron Rad. 2 (1995) 155.
[57] A. Hoffman, Nucl. Instr. Meth. 152 (1978) 17.
[58] A. Hoffman, these Proceedings.
[59] J.D. Jackson, "Classical Electrodynamics", Wiley, New York (1962)
[60] R.P. Walker, Nucl. Instr. Meth. A267 (1988) 537.
[61] A.N. Didenko et al., Sov. Phys. JETP 49 (1979) 973.
[62] R. Tatchyn and I. Lindau, Nucl. Instr. Meth. 222 (1984) 14.
[63] S. Krinsky, Nucl. Instr. Meth. 172 (1980) 73.
[64] R.P. Walker, Nucl. Instr. Meth. A335 (1993) 328.
[65] K.J. Kim, Nucl. Instr. Meth. A246 (1986) 71.
[66] J. Schwinger, Phys. Rev. 75 (1949) 1912.
[67] P. Elleaume, J. Synchr. Rad. 1 (1994) 19.
[68] K.J. Kim, Nucl. Instr. Meth. A246 (1986) 67.
[69] R. Tatchyn et al., Proc. SPIE 582 (1985) 47.
[70] R. Barbini et al., Ref. [32] p. 100.
[71] J. Chavanne and P. Elleaume, ESRF-ID-90/46
[72] P. Elleaume and X. Marechal, ESRF-SR/ID-91-54
[73] R.J. Dejus and A. Luccio, Nucl. Instr. Meth. A347 (1994) 61.
[74] H. Rarbach et al., Nucl. Instr. Meth. A266 (1988) 96.
[75] R.P. Walker and B. Diviacco, Rev. Sci. Inst. 63 (1992) 392.
[76] D. Steinmüller-Nethl et al., Nucl. Instr. Meth. A285 (1989) 307.
[77] C. Wang and D. Xian, Nucl. Instr. Meth. A288 (1990) 649.
[78] C. Wang, Phys. Rev. E 47 (1993) 4358.
[79] R.P. Walker, ST/M-TN-89/24, July 1989
[80] R. Coîsson et al., Nucl. Instr. Meth. 201 (1982) 3.
[81] G.E. van Dorssen et al., Proc. SPIE Vol. 2013 (1993) 104.
[82] N.Marks, Proc. Proc. CERN Accelerator School Fifth General Accelerator Physics Course, CERN 94-01, Vol. II, p. 867.
[83] S. Krinsky, BNL 23747 (1977); also Ref. [30] p. 97.
[84] M.W. Poole and R.P. Walker, Nucl. Instr. Meth. 176 (1980) 487.
[85] G.A. Kornyukhin et al., Nucl. Instr. Meth. 208 (1983) 189.
[86] N.A. Vinokurov, Nucl. Instr. Meth. A246 (1986) 105.
[87] K. Halbach, Nucl. Instr. Meth. 187 (1981) 109.
[88] K. Halbach, J. de Physique C1 44 (1983) 211.
[89] K. Halbach, Nucl. Instr. Meth. 169 (1980) 1.
[90] B. Diviacco and R.P. Walker, Proc. PAC 1993, IEEE Catalog No. 93CH3279-7, p. 1593.
[91] 6 GeV Synchrotron X-ray Source Conceptual Design Report, Supplement A, LS-52 (March 1986), Argonne National Laboratory.
[92] R.P. Walker, Daresbury Laboratory Technical Memorandum DL/SCI/TM54A, Nov. 1987.
[93] K. Halbach, Lawrence Berkeley Laboratory Report LSBL-034 (1989)
[94] T. Meinander, SPIE Vol. 582 (1986) 193.
[95] K. Halbach et al., IEEE Trans. Nucl. Sci. NS-32 (1985) 3640.
[96] D.C. Quimby et al., Nucl. Instr. Meth. A259 (1987) 304.
[97] S. Sasaki et al., Rev. Sci. Instr. 60 (1989) 1859.
[98] B. Diviacco and R.P. Walker, Sincrotrone Trieste Internal Report ST/M-TN-92/5 (May 1992).
[99] E. Hoyer et al., Proc. PAC 1987, IEEE Catalog No. 87CH2387-9 (1987) 1508.
[100] D. Humphries et al., Proc. PAC 1993, IEEE Catalog No. 93CH3279-7, p. 1581.
[101] I. Vasserman and E.R. Moog, Rev. Sci. Instr. 66 (1995) 1943.
[102] J. Chavanne et al., Proc PAC 1995, IEEE Catalog No. 95CH35843, p. 1319.
[103] B.M. Kincaid, J. Opt. Soc. Am. B2 (1985) 1294.
[104] B. Diviacco and R.P. Walker, Proc. PAC 1989, IEEE Catalog No. 89CH2669-0, p. 1259.

[105] B.L. Bobbs et al., Nucl. Instr. Meth. A296 (1990) 574.
[106] R. Dejus, Rev. Sci. Instr. 66 (1995) 1875.
[107] A.D. Cox and B.P. Youngman, SPIE 582 (1986) 91.
[108] R. Hajima et al., Nucl. Instr. Meth. A318 (1992) 822.
[109] D.C. Quimby et al., Nucl. Instr. Meth. A285 (1989) 281.
[110] S.C. Gottschalk et al., Nucl. Instr. Meth. A296 (1990) 579.
[111] J. Chavanne et al., ESRF Internal Report ESRF-SR/ID-89-27, Sept. 1989.
[112] B. Diviacco, Proc. PAC 1993, IEEE Catalog No. 93CH3279-7, p. 1590
[113] J. Chavanne and P. Elleaume, Rev. Sci. Instr. 66 (1995) 1868
and SR News, Vol. 8, No. 1, Jan./Feb. 1995, p. 18.
[114] B. Diviacco and R.P. Walker, Nucl. Instr. Meth. A368 (1996) 522.
[115] I. Vasserman, Advanced Photon Source LS-253, Jan. 1996.
[116] S.C. Gottschalk et al., Rev. Sci. Instrum. 67(9) (1996).
[117] Proc. Int. Workshop on Magnetic Measurements of Insertion Devices, Argonne National Laboratory, Sep. 1993, ANL/APS/TM-13
[118] M. Born and E. Wolf, "Principles of Optics" 6th ed. (Pergamon Press, 1980).
[119] H. Kitamura, Jap. J. Appl. Phys. (1980) L185.
[120] W.R. Smythe, Static and Dynamic Electricity (McGraw-Hill, New York, 1950) p. 277
[121] J.P. Blewett and R. Chasman, J. Appl. Phys., 48 (1977) 2692.
[122] S. Y. Park and J. M. Baird, J. Appl. Phys. 53 (1982) 1320.
[123] J. Fajans, J. Appl. Phys. 55 (1984) 43.
[124] D.F. Alferov et al., Sov. Phys. Tech. Phys. 21 (1976) 1408.
[125] R.P. Walker, Nucl. Instr. Meth. A237 (1985) 366.
[126] L. R. Elias and J.M. Madey, Rev. Sci. Instr. 50 (1979) 1335.
[127] U. Bizzari et al., J. Phys. Coll. C1 44 (1983) 313.
[128] E.D. Shaw et al., J. Phys. Coll. C1 44 (1983) 153.
[129] J. Vetrovec, Nucl. Instr. Meth. Phys. Res. A296 (1990) 563.
[130] K. Halbach, Nucl. Instr. Meth. 187 (1981) 109.
[131] M.S. Curtin et al., Nucl. Instr. Meth. Phys. Res. A237 (1985) 395.
[132] P. Diament et al., Nucl. Instr. Meth. Phys. Res. A237 (1985) 381.
[133] H. Onuki, Nucl. Instr. Meth. Phys. Res. A 246 (1986) 94.
[134] K. Yagi et al., Rev. Sci. Instr. 63 (1992) 396.
[135] S. Yamamoto and H. Kitamura, Jpn. J. Appl. Phys. 26 (1987) L1613.
[136] S. Yamamoto et al., Rev. Sci. Instr. 60 (1989) 1834.
[137] S. Yamamoto et al., Phys. Rev. Lett. 62 (1989) 2672.
[138] R.P. Walker and B. Diviacco, Rev. Sci. Instr. 63 (1992) 332.
[139] E. Gluskin et al., Proc. 1995 PAC, IEEE Catalog No. 95CH35843, p. 1426.
[140] L. Nahon et al., to be published in Nucl. Instr. Meth.
[141] P. Elleaume, Nucl. Instr. Meth., A304 (1991) 719.
[142] B. Diviacco and R.P. Walker, Nucl. Instr. Meth. A292 (1990) 517.
[143] P. Elleaume, Nucl. Instr. Meth. A304 (1991) 719.
[144] P. Elleaume, Proc. 10th ICFA Beam Dynamics Panel Workshop, 4th Generation Light Sources, Grenoble, Jan. 1996, p. WG7-40.
[145] S. Sasaki et al., Jpn. J. Appl. Phys. 31 (1992) L1794.
[146] K. Kakuno and S. Sasaki, JAERI-M 92-157, Sept. 1992.
[147] S. Sasaki, Nucl. Instr. Meth. A347 (1994) 87.
[148] R. Carr and S. Lidia, Proc. SPIE 2013 (1993) 56.
[149] R. Carr et al., Rev. Sci. Instr. 66 (1995) 1862.
[150] X. Maréchal et al., Rev. Sci. Instr. 66 (1995) 1936.
[151] J. Goulon et al., Nucl. Instr. Meth. A254 (1987) 192.
[152] J. Pflüger and G. Heintze, Nucl. Instr. Meth. A289 (1990) 300.
[153] M. Barthès et al., IEEE Trans. Magn. 24 (1987) 1233, and 28 (1992) 601.
[154] J. Pflüger, Rev. Sci. Instr. 63 (1992) 295.
[155] D. Schirmer, Proc. XVth Int. Conf. on High Energy Accelerators, Int. J. Mod. Phys. A (Proc. Suppl.) 2B (1993), Volume 2, p. 644
[156] M.B. Moisev et al., Sov. Phys. J. 21 (1978) 332,
K.J. Kim, Nucl. Instr. Meth., 219 (1984) 425.

[157] J. Bahrdt et al., Rev. Sci. Instr. 63 (1992) 339.
[158] M.A. Green at al., Proc. 1991 Particle Accelerator Conference, p. 1088.
[159] R. Savoy and K. Halbach, Proc. 1991 Particle Accelerator Conference, p. 2718
[160] S. Sasaki, Proc. PAC 1997, to be published.
[161] R. Bakker and M.W. Poole, these Proceedings.
[162] Recent Conferences have been published in Nucl. Instr. Meth. Volumes A375, A358, A341, A331, A318, A304 etc.
[163] N.M. Kroll et al., Physics of Quantum Electronics Vol. 7; Free Electron Generators of Coherent Radiation (Addison-Wesley, Reading, MA (1980) 89.
[164] H. Boehmer et al., Phys. Rev. Lett. 48 (1982) 141; W.E. Stein et al., Proc. 1981 Linear Accel. Conf., Santa-Fe NM, LANL Report LA-9234, Feb. 1982; J.M. Slater et al., IEEE J. Q. Electron. QE-19 (1983) 374.
[165] G.A. Deis, IEEE Trans. Mag. 24 (1988) 1090.
[166] K. Halbach, Nucl. Instr. Meth. A250 (1986) 95.
[167] N.A. Vinokurov and A.N. Skrinsky, Budker Institute of Nuclear Physics, Novosibirk, Preprint 77-59.
[168] P. Elleaume, Nucl. Instr. Meth. A237 (1985) 28.
J.M. Ortega et al., Nucl. Instr. Meth. 206 (1983) 281.
[169] H. Hama, Nucl. Instr. Meth. A375 (1996) 57.
[170] I. Boscolo and V. Stagno, Il Nuovo Cimento 58B (1980) 267.
[171] C. Shih and M.Z. Caponi, IEEE J. Q. Electron. QE-19 (1983) 369.
[172] J.A. Edighoffer et al., Phys. rev. lett. 52 (1984) 344.
[173] K. E. Robinson et al., IEEE J. Q. Electron. QE-23 (1987) 1497.
[174] T. Keishi et al., Nucl. Instr. Meth. A341 (1994) ABS 128.
[175] P.P. Tesch, Nucl. Instr. Meth. A375 (1995) 504.
[176] A.A. Varfolomeev et al., Nucl. Instr. Meth. A318 (1992) 813.
[177] G. Ramian et al., Nucl. Instr. Meth. A250 (1986) 125.,
K.P. Paulson, Nucl. Instr. Meth. A296 (1990) 624.
[178] V.L. Granatstein, Appl. Phys. Lett. 47 (1985) 643.
[179] A. Sneh and W. Jerby, Nucl. Instr. Meth. A285 (1989) 294.
[180] R.W. Warren et al., Nucl. Instr. Meth. A296 (1990) 558,
R.W. Warren et al., Nucl. Instr. Meth. A304 (1991) 765,
C.M. Fortgang and R.W. Warren, Nucl. Instr. Meth. A341 (1994) 436.
[181] B. Feng, Rev. Sci. Instr. 63 (1992) 3849.
[182] S.C. Chen et al., Nucl. Instr. Meth. A285 (1989) 290.
[183] R. Stoner and G. Bekefi, IEEE J. Q. Electronics 31 (1995) 1158.
[184] I. Ben-Zvi et al., Nucl. Instr. Meth. A318 (1992) 781.
[185] G. Ingold et al., Nucl. Instr. Meth. A375 (1996) 451.
[186] N. Ohigashi et al., Nucl. Instr. Meth. A341 (1994) 426.
[187] Y.C. Huang et al., Nucl. Instr. Meth. A341 (1994) 431.
[188] E.T. Scharlemann, J. Appl. Phys. 58 (1985) 2154.
[189] Y. Tsunawaki et al., Nucl. Instr. Meth. A304 (1991) 753.
[190] Y. Tsunawaki et al., Nucl. Instr. Meth. A331 (1993) 727.
[191] A.A. Varfolomeev and A.H. Hairetdinov, Nucl. Instr. Meth. A341 (1994) 462.
[192] A.A. Varfolomeev et al., Nucl. Instr. Meth. A341 (1994) 466.
[193] R.D. Schlueter, Nucl. Instr. Meth A358 (1985) 44.
[194] A.A. Varfolomeev et al., Nucl. Instr. Meth. A358 (1995) 70.
[195] R. Tatchyn, Nucl. Instr. Meth. A341 (1994) 449.
[196] Y.M. Nikitina and J. Pflüger, Nucl. Instr. Meth. A375 (1996) 325.
[197] S. Caspi et al., Proc. 1995 PAC, IEEE Catalog No. 95CH35843, p. 1441.

APPENDIX 1 SPECTRAL AND ANGULAR DISTRIBUTION OF THE RADIATION EMITTED IN VARIOUS TYPES OF SINUSOIDAL UNDULATOR

Given the following general field distribution which includes both planar, circular and general elliptical undulator types:

$$B_x = B_{xo}\sin(kz+\psi) \qquad B_y = B_{yo}\sin(kz)$$

we obtain, using the procedure outlined in section 2.1, for the transverse motion:

$$\beta_y = -\frac{K_x}{\gamma}\cos(\Omega t+\psi) \qquad \beta_x = \frac{K_y}{\gamma}\cos(\Omega t)$$

$$y = -\frac{K_x}{\gamma}\frac{c}{\Omega}\sin(\Omega t+\psi) \qquad x = \frac{K_y}{\gamma}\frac{c}{\Omega}\sin(\Omega t)$$

and for the longitudinal motion:

$$\beta_z \cong \bar{\beta} - \frac{K_y^2}{4\gamma^2}\cos 2\Omega t - \frac{K_x^2}{4\gamma^2}\cos 2(\Omega t+\psi)$$

$$z = \bar{\beta}ct - \frac{K_y^2}{4\gamma^2}\frac{c}{2\Omega}\sin 2\Omega t - \frac{K_x^2}{4\gamma^2}\frac{c}{2\Omega}\sin 2(\Omega t+\psi)$$

where

$$\Omega = \frac{2\pi\bar{\beta}c}{\lambda_o}, \text{ and } \bar{\beta} \cong 1 - \frac{1}{2\gamma^2} - \frac{K_x^2}{4\gamma^2} - \frac{K_y^2}{4\gamma^2}$$

The general expression for the radiated intensity in the case of a periodic magnet in the far-field approximation is given by the following (see section 3.1):

$$\frac{d^2I}{d\omega\, d\Omega} = \frac{N^2 e^2 \omega^2}{(4\pi\varepsilon_o)4\pi^2 c}\left|\int_{-\lambda_o/2\bar{\beta}c}^{\lambda_o/2\bar{\beta}c}\{\hat{n}\wedge(\hat{n}\wedge\beta)\}\, e^{i\omega(t-n\cdot r/c)}\, dt\right|^2 L(N\Delta\omega/\omega_1(\theta)) \qquad \text{(A1)}$$

Expanding the term $\hat{n}\wedge(\hat{n}\wedge\beta)$ to order K/γ and using the small angle approximation $\hat{n} = (\theta\cos\phi, \theta\sin\phi, 0)$, one obtains $\hat{n}\wedge(\hat{n}\wedge\beta) \cong (\theta\cos\phi - \beta_x, \theta\sin\phi - \beta_y, 0)$. Expanding also the phase terms we obtain:

$$\omega(t - n\cdot r/c) = \omega t - \omega\theta\cos\phi\, x/c - \omega\theta\sin\phi\, y/c - \omega\cos\theta\, z/c$$

$$= \omega t(1-\bar{\beta}\cos\theta) - \frac{\omega\theta\cos\phi}{\Omega}\frac{K_y}{\gamma}\sin\Omega t + \frac{\omega\theta\sin\phi}{\Omega}\frac{K_x}{\gamma}\sin(\Omega t+\psi) +$$

$$\frac{\omega}{2\Omega}\left(\frac{K_y^2}{4\gamma^2}\sin 2\Omega t + \frac{K_x^2}{4\gamma^2}\sin 2(\Omega t+\psi)\right)$$

With large N we only need evaluate the expression at the harmonic frequencies, where:

$$\omega = \frac{n\Omega}{(1-\bar{\beta}\cos\theta)} = \frac{n\Omega 2\gamma^2}{1 + K_x^2/2 + K_y^2/2 + \gamma^2\theta^2} \qquad \text{(A2)}$$

Combining the trigonometric terms we then obtain:

$$\omega(t - n\cdot r/c) = n\Omega t - X\sin(\Omega t - \Phi) + Y\sin(2\Omega t + \Psi)$$

where,

$$X = \frac{2n\gamma\theta}{A}\sqrt{K_y^2\cos^2\phi + K_x^2\sin^2\phi - 2K_xK_y\sin\phi\cos\phi\cos\psi}$$

$$Y = \frac{n}{4A}\sqrt{K_y^4 + K_x^4 + 2K_x^2K_y^2\cos 2\psi}$$

and

$$A = 1 + K_x^2/2 + K_y^2/2 + \gamma^2\theta^2,\quad \tan\Phi = \frac{-K_x\sin\phi\sin\psi}{K_x\sin\phi\cos\psi - K_y\cos\phi},\quad \tan\Psi = \frac{K_x^2\sin 2\psi}{K_x^2\cos 2\psi + K_y^2}.$$

By means of the relation $\exp(ix\sin\phi) = \sum_{p=-\infty}^{\infty} J_p(x)\exp(ip\phi)$ the phase expression now becomes:

$$e^{i\{n\Omega t - X\sin(\Omega t-\Phi)+Y\sin(2\Omega t+\Psi)\}} = \sum_{p'=-\infty}^{\infty}\sum_{p=-\infty}^{\infty} J_{p'}(X)J_p(Y)\,e^{i\{n\Omega t - p'(\Omega t-\Phi)+p(2\Omega t+\Psi)\}}$$

and hence Eq. (A1) becomes:

$$\frac{d^2I}{d\omega\,d\Omega} = \frac{N^2e^2\omega^2}{(4\pi\varepsilon_o)4\pi^2c}\,L(N\Delta\omega/\omega_1(\theta))\;\times$$

$$\left|\sum_{p'=-\infty}^{\infty}\sum_{p=-\infty}^{\infty} J_{p'}(X)J_p(Y)\int_{-\lambda_o/2\bar{\beta}c}^{\lambda_o/2\bar{\beta}c}(\theta\cos\phi - \beta_x, \theta\sin\phi - \beta_y)\,e^{i\{n\Omega t - p'(\Omega t-\Phi)+p(2\Omega t+\Psi)\}}\,dt\right|^2$$

where the two terms in the integrand represent the amplitudes polarized respectively in the x and y directions. It can be seen that the integral over one period is non-zero only when either $n - p' + 2p = 0$ for the constant terms, or when $n - p' + 2p = \pm 1$ for the terms in $\cos\Omega t$ or $\sin\Omega t$. Defining therefore $n - p' + 2p = -q$, where $q = -1, 0, 1$ we then have, using Eq. (A2):

$$\frac{d^2I}{d\omega\,d\Omega} = \frac{N^2e^2\gamma^2}{(4\pi\varepsilon_o)c}\frac{n^2}{A^2}L(N\Delta\omega/\omega_1(\theta))\;\left|A_x, A_y\right|^2$$

with:

$$A_x = 2\gamma\theta\cos\phi S_o - K_y(S_1 + S_{-1}) \qquad \text{(A3)}$$

$$A_y = 2\gamma\theta\sin\phi S_o + K_x\left(e^{i\Psi}S_1 + e^{-i\Psi}S_{-1}\right)$$

where:

$$S_q = \sum_{p=-\infty}^{\infty} J_p(Y)J_{n+2p+q}(X)\,e^{i(n+2p+q)\Phi}\,e^{ip\Psi}$$

On-axis $X = 0$ and hence $n + 2p + q = 0$ and $p = (-n - q)/2$. It follows that $S_o = 0$ and:

$$S_q = J_{\frac{-(n+q)}{2}}(Y)\,e^{-i(n+q)\Psi/2}$$

for $q=-1, 1$, with $n=\text{odd}$. After some simplification, and using the fact that $J_{-n}(x)=(-1)^n J_n(x)$ one obtains:

$$\begin{aligned} A_x &= K_y\left(J_{\frac{n+1}{2}}(Y)e^{i\frac{n+1}{2}\Psi} - J_{\frac{n-1}{2}}(Y)e^{i\frac{n-1}{2}\Psi}\right) \\ A_y &= K_x\left(-J_{\frac{n+1}{2}}(Y)e^{i\frac{n+1}{2}\Psi}e^{-i\psi} + J_{\frac{n-1}{2}}(Y)e^{i\frac{n-1}{2}\Psi}e^{i\psi}\right) \end{aligned} \tag{A4}$$

Pure elliptical case

We have $\psi=\pi/2$ and hence $\tan\Phi=(K_x/K_y)\tan\phi$ and $\Psi=0$. We obtain therefore from Eq. (A3):

$$\begin{aligned} A_x &= 2\gamma\theta\cos\phi S_o - K_y(S_1+S_{-1}) \\ A_y &= 2\gamma\theta\sin\phi S_o + iK_x(S_1-S_{-1}) \end{aligned}$$

where:

$$S_q = \sum_{p=-\infty}^{\infty} J_p(Y)J_{n+2p+q}(X)\,e^{i(n+2p+q)\Phi}$$

and:

$$X=\frac{2n\gamma\theta}{A}\sqrt{K_y^2\cos^2\phi+K_x^2\sin^2\phi}\,,\quad Y=\frac{n}{4A}(K_y^2-K_x^2)$$

which is equivalent to the result of Yamamoto and Kitamura [135].

On-axis we obtain directly from Eq. (A4):

$$A_x = K_y\left(J_{\frac{n+1}{2}}(Y)-J_{\frac{n-1}{2}}(Y)\right)\qquad A_y = iK_x\left(J_{\frac{n+1}{2}}(Y)+J_{\frac{n-1}{2}}(Y)\right)$$

Pure circular case

In this case we have in addition to the above, $K_y=K_x=K$ and hence $X=2n\gamma\theta K/A$, $Y=0$, $\Phi=\phi$. We have then:

$$S_q = J_{n+q}(X)e^{i(n+q)\phi}$$

and hence:

$$\begin{aligned} A_x &= e^{in\phi}\left\{2\gamma\theta\cos\phi J_n(X) - K\left(J_{n+1}(X)e^{i\phi}+J_{n-1}(X)e^{-i\phi}\right)\right\} \\ A_y &= e^{in\phi}\left\{2\gamma\theta\sin\phi J_n(X) + iK\left(J_{n+1}(X)e^{i\phi}-J_{n-1}(X)e^{-i\phi}\right)\right\} \end{aligned} \tag{A5}$$

The general expressions for the amplitudes are therefore still quite complicated, however since the radiation pattern is circularly symmetric we can take any value of ϕ, for example $\phi=0$:

$$\begin{aligned} A_x &= 2\gamma\theta J_n(X) - K\left(J_{n+1}(X)+J_{n-1}(X)\right) \\ A_y &= iK\left(J_{n+1}(X)-J_{n-1}(X)\right) \end{aligned}$$

By making use of the following relations:

$$J_{n+1}(x)+J_{n-1}(x)=\frac{2n}{x}J_n(x) \quad \text{and} \quad J_{n-1}(x)-J_{n+1}(x)=2J_n'(x) \tag{A6}$$

we can express the results in the following form:

$$A_x=\left(2\gamma\theta-\frac{2nK}{X}\right)J_n(X), \quad A_y=-2iKJ_n'(X) \tag{A7}$$

The expression for the total intensity then becomes:

$$\left|A_x^2\right|+\left|A_y^2\right|=4K^2\left[J_n'^2(X)+J_n^2(X)\left(\frac{\gamma\theta}{K}-\frac{n}{X}\right)\right]$$

in agreement with Alferov et al. [14] and Kincaid [15].

On-axis $X=0$ and hence in Eq. (A5) there is only one term with $n=1$. We have then:

$$A_x=-K \text{ and } A_y=-iK$$

The radiation has therefore complete circular polarization ($S_3=1$) with total intensity:

$$\frac{d^2I}{d\omega\, d\Omega}=\frac{N^2e^2\gamma^2}{(4\pi\varepsilon_o)c}\frac{2K^2}{(1+K^2)^2}L(N\Delta\omega/\omega_1(\theta))$$

We note in passing that the circular polarization component reverses direction off-axis when $A_x=0$ in Eq. (A7), i.e. when $\gamma\theta=\sqrt{1+K^2}$.

Linear case

In this case $K_x=0$ and hence $\Phi=\Psi=0$, $X=2n\gamma\theta K_y\cos\phi/A$, $Y=nK_y^2/4A$ and $A=1+K_y^2/2+\gamma^2\theta^2$. As a result we have from Eq. (A3):

$$\begin{aligned} A_x&=2\gamma\theta\cos\phi S_o-K_y(S_1+S_{-1}) \\ A_y&=2\gamma\theta\sin\phi S_o \end{aligned} \tag{A8}$$

with

$$S_q=\sum_{p=-\infty}^{\infty}J_p(Y)J_{n+2p+q}(X)$$

Making use of the first of the relations in Eq. (A4) we can write:

$$S_1+S_{-1}=\frac{2n}{X}S_o+\frac{4}{X}S_2=\frac{A}{K_y\gamma\theta\cos\phi}\left(S_o+\frac{2}{n}S_2\right)$$

where

$$S_2=\sum_{p=-\infty}^{\infty}pJ_p(Y)J_{n+2p}(X)$$

Hence,

$$A_x = 2\gamma\theta\cos\phi S_o - \frac{A}{\gamma\theta\cos\phi}\left(S_o + \frac{2}{n}S_2\right) \quad A_y = 2\gamma\theta\sin\phi S_o$$

in agreement with the result of Aferov et al. [14] and Krinsky [63].

On-axis we obtain either from Eq. (A8) or (A4):

$$A_x = K_y\left(J_{\frac{n+1}{2}}(Y) - J_{\frac{n-1}{2}}(Y)\right) \text{ and } A_y = 0$$

The intensity is often written in the form:

$$\frac{d^2I}{d\omega\, d\Omega} = \frac{N^2 e^2 \gamma^2}{(4\pi\varepsilon_o)c} L(N\Delta\omega/\omega_1(\theta))F_n(K)$$

where:

$$F_n(K) = \frac{n^2K^2}{(1+K^2/2)^2}\left[J_{\frac{n+1}{2}}(Z) - J_{\frac{n-1}{2}}(Z)\right]^2 \quad \text{with} \quad Z = \frac{nK^2}{4(1+K^2/2)}$$